



January 2023

## RF Coverage Planning And Analysis With Adaptive Cell Sectorization In Millimeter Wave 5G Networks

Md Maruf Ahamed

[How does access to this work benefit you? Let us know!](#)

Follow this and additional works at: <https://commons.und.edu/theses>

---

### Recommended Citation

Ahamed, Md Maruf, "RF Coverage Planning And Analysis With Adaptive Cell Sectorization In Millimeter Wave 5G Networks" (2023). *Theses and Dissertations*. 5661.  
<https://commons.und.edu/theses/5661>

This Dissertation is brought to you for free and open access by the Theses, Dissertations, and Senior Projects at UND Scholarly Commons. It has been accepted for inclusion in Theses and Dissertations by an authorized administrator of UND Scholarly Commons. For more information, please contact [und.common@library.und.edu](mailto:und.common@library.und.edu).

RF COVERAGE PLANNING AND ANALYSIS WITH ADAPTIVE CELL  
SECTORIZATION IN MILLIMETER WAVE 5G NETWORKS

by

Md. Maruf Ahamed

Master of Science, University of North Dakota, 2015

Bachelor of Science, Rajshahi University of Engineering & Technology, 2010

A Dissertation

Submitted to the Graduate Faculty

of the

University of North Dakota

in partial fulfillment of the requirements

for the degree of

Doctor of Philosophy Electrical Engineering

Grand Forks, North Dakota

December

2023

Copyright 2023 Md. Maruf Ahamed

This dissertation, submitted by Md Maruf Ahamed in partial fulfillment of the requirements for the Degree of Doctor of Philosophy Electrical Engineering from the University of North Dakota, has been read by the Faculty Advisory Committee under whom the work has been done and is hereby approved.

---

Dr. Ryan Adams, Chairperson

---

Dr. Naima Kaabouch, Committee Member

---

Dr. Tarek Elderini, Committee Member

---

Dr. Taufique Mahmood, Member-At-Large

This dissertation is being submitted by the appointed advisory committee as having met all of the requirements of the School of Graduate Studies at the University of North Dakota and is hereby approved.

---

Dr. Chris Nelson  
Dean of the School of Graduate Studies

---

12/06/2023

Date



## PERMISSION

Title            RF Coverage Planning and Analysis with Adaptive Cell Sectorization in  
Millimeter Wave 5G Networks

Department    School of Electrical Engineering and Computer Science

Degree           Doctor of Philosophy Electrical Engineering

In presenting this dissertation in partial fulfillment of the requirements for a graduate degree from the University of North Dakota, I agree that the library of this University shall make it freely available for inspection. I further agree that permission for extensive copying for scholarly purposes may be granted by the professor who supervised my dissertation work or, in his absence, by the chairperson of the department or the dean of the Graduate School. It is understood that any copying or publication or other use of this thesis or part thereof for financial gain shall not be allowed without my written permission. It is also understood that due recognition shall be given to me and to the University of North Dakota in any scholarly use which may be made of any material in my dissertation.

Signature    Md. Maruf Ahamed

Date           11/16/2023

## ACKNOWLEDGEMENTS

First of all, I would like to thank Dr. Ryan Adams for giving me the opportunity to work with him and providing all the guidance throughout my doctoral work. His mentoring and continuous support has motivated me to stay focused and achieved my goals. I would also like to thank my committee members, Dr. Naima Kaabouch, Dr. Tarek Elderini, and Dr. Taufique Mahmood for their timely feedbacks, valuable comments, and suggestions. I also thank the School of Electrical Engineering and Computer Science department, University of North Dakota, for giving me this opportunity and financial support to finish my dissertation. Finally, I am very grateful to my wife Shadia Sultana and my parents for their love and support.

## DEDICATION

To my lovely wife Shadia Sultana

## ABSTRACT

The advancement of Fifth Generation Network (5G) technology is well underway, with Mobile Network Operators (MNOs) globally commencing the deployment of 5G networks within the mid-frequency spectrum range (3GHz–6GHz). Nevertheless, the escalating demands for data traffic are compelling MNOs to explore the high-frequency spectrum (24GHz–100GHz), which offers significantly larger bandwidth (400MHz-800 MHz) compared to the mid-frequency spectrum (3GHz–6GHz), which typically provides 50MHz-100MHz of bandwidth. However, it is crucial to note that the higher-frequency spectrum imposes substantial challenges due to exceptionally high free space propagation loss, resulting in 5G cell site coverage being limited to several hundred meters, in contrast to the several kilometers achievable with 4G. Consequently, MNOs are faced with the formidable task of accurately planning and deploying hundreds of new 5G cells to cover the same areas served by a single 4G cell.

This dissertation embarks on a comprehensive exploration of Radio Frequency (RF) coverage planning for 5G networks, initially utilizing a conventional three-sector cell architecture. The coverage planning phase reveals potential challenges, including coverage gaps and poor Signal-to-Interference-plus-Noise Ratio (SINR). In response to these issues, the dissertation introduces an innovative cell site architecture that embraces both nine and twelve sector cells, enhancing RF coverage through the adoption of an advanced antenna system designed with subarrays, offering adaptive beamforming and beam steering capabilities. To further enhance energy efficiency, the dissertation introduces adaptive higher-order cell-sectorization (e.g., nine sector cells and twelve sector cells). In this proposed method, all sectors within a twelve-sector cell remain active during peak hours

(e.g., daytime) and are reduced to fewer sectors (e.g., nine sectors or six sectors per cell) during off-peak hours (e.g., nighttime). This dynamic adjustment is facilitated by an advanced antenna system utilizing sub-array architecture, which employs adaptive beamforming and beam steering to tailor the beamwidth and radiation angle of each active sector. Simulation results unequivocally demonstrate significant enhancements in RF coverage and SINR with the implementation of higher-order cell-sectorization. Furthermore, the proposed adaptive cell-sectorization method significantly reduces energy consumption during off-peak hours.

In addition to addressing RF coverage planning, this dissertation delves into the numerous challenges associated with deploying 5G networks in the higher frequency spectrum (30GHz-300GHz). It encompasses issues such as precise cell site planning, location acquisition, propagation modeling, energy efficiency, backhauling, and more. Furthermore, the dissertation offers valuable insights into future research directions aimed at effectively surmounting these challenges and optimizing the deployment of 5G networks in the high-frequency spectrum.

## TABLE OF CONTENTS

ACKNOWLEDGEMENTS.....	v
ABSTRACT.....	x
TABLE OF CONTENTS.....	xii
LIST OF TABLES.....	xvii
LIST OF Figures.....	<b>Error! Bookmark not defined.</b>
LIST OF ACRONYMS .....	xxvii
Chapter 1 Introduction .....	1
1.1 Motivation.....	1
1.2 Contributions of the Dissertation .....	7
1.3 Dissertation Outline .....	8
1.4 Publications.....	8
Chapter 2 RF Coverage Planning .....	11
2.1 Introduction.....	11
2.2 What is Network Coverage? .....	11
2.3 Cell-Sectorization .....	12
2.4 Frequency Planning .....	13
2.4.1 N = 7 frequency reuse plan .....	14
2.4.2 N = 3 frequency reuse plan .....	15
2.5 Carrier to Interference (C/I).....	16
2.5.1 Methods of Locating Cochannel Cells.....	19

2.5.2 Worst Case Analysis of C/I in an Omnidirectional Antenna System.....	20
2.5.3 Worst Case Analysis of C/I in a 3-Sector Cellular System.....	22
2.5.4 Worst Case Analysis of C/I in a 6-Sector Cellular System.....	23
2.6 Network Layout .....	25
2.7 Define Transmitter Sites .....	27
2.8 Advanced Antenna System Design.....	27
2.8.1 Design an Antenna Array .....	27
2.8.2 Antenna Array with Reduced Side Lobes .....	30
2.8.3 Antenna Array Analysis with Amplitude Tapering .....	33
2.9 Propagation modeling .....	41
2.9.1 Free Space Propagation Modelling .....	42
2.9.2 RF Signal Attenuation Due to Rainfall .....	43
2.9.3 RF Signal Attenuation Due to Fog and Clouds.....	46
2.9.4 RF Signal Attenuation Due to Atmospheric Gas .....	48
2.9.5 Total RF Propagation Loss.....	52
2.9.6 Signal Power Losses Associated with Transmitting and Receiving Antenna.....	55
2.9.7 RF Link Budget Analysis.....	59
2.9.8 Signal-to-Noise Ratio (SNR) .....	60
2.9.9 Calculate Required Transmit Power .....	61
2.9.10 Literature Review for RF Propagation Modeling Candidates of 5G.....	62

2.10 Define 5G cell site radius.....	64
<b>Chapter 3 RF Coverage Simulation and Analysis .....</b>	<b>67</b>
3.1 Introduction.....	67
3.2 RF Coverage Simulation Tool and Configuration of Simulation Parameters.....	67
3.2.1 Embracing RF Coverage Simulation Tool .....	67
3.2.2 Parameters Configuration for RF Coverage Simulations..	69
3.3 RF Coverage Simulations: Employing Single Antenna Element in Every Sector.....	71
3.4 RF Coverage Simulations: Employing 8-by-8 Antenna Array in Every Sector .....	73
3.5 RF Coverage Simulations: Employing 16-by-16 Antenna Array in Every Sector.....	75
3.6 Improved RF Coverage Through the use of Advanced Antenna Systems .....	77
3.6.1 Types of Base Station (BS) Antenna Downtilt .....	78
3.6.2 RF Coverage Versus BS Antenna Downtilt Angle .....	80
3.6.3 RF Coverage Versus Operating Frequency.....	83
3.6.4 RF Coverage Versus BS Antenna Height .....	84
<b>Chapter 4 Higher-Order Cell-Sectorization for 5G and Beyond .....</b>	<b>86</b>
4.1 Introduction.....	86
4.2 Literature Review on Higher-order Cell-Sectorization.....	87
4.3 RF Coverage Versus the Number of Sectors Per Cell .....	90



4.3.1 Improved RF Coverage Employing 8-by-8 Antenna Array in Every Sector.....	91
4.3.2 Improved RF Coverage Employing 16-by-16 Antenna Array in Every Sector .....	92
4.4 Cell Site Power Consumption with Higher-Order Cell-Sectorization	94
4.4.1 Dynamic Mode Power Consumption .....	95
4.4.2 Sleeping Mode Power Consumption Simulation .....	97
4.5 Adaptive Beamforming and Cell-Sectorization.....	99
4.5.1 Traditional Phased Array Architecture .....	99
4.5.2 Phased Array Architecture with Subarrays .....	100
4.5.3 Adaptive Beamforming .....	101
4.5.4 Adaptive Beam Steering.....	103
4.5.5 Proposed Adaptive Cell-Sectorization to Save Energy...	104
<b>Chapter 5 RF Coverage Analysis for Non-Line-of-Sight Location.....</b>	<b>109</b>
5.1 Introduction.....	109
5.2 User at Non-Line-of-Sight with One Reflected Path.....	111
5.3 User at non-line-of-sight with two reflected paths .....	112
5.4 Adaptive Beam Steering to Enhance the Received signal Power.....	114
<b>Chapter 6 5G Network Deployment Challenges and Guidelines .....</b>	<b>118</b>
6.1 Introduction 5G Network Deployment Challenges .....	118
6.2 Accurate Cell Site Planning .....	118
6.3 Acquiring Cell Site Location .....	119
6.4 Propagation Modeling and Coverage Prediction .....	121

6.5 Challenges Raised by Advanced Antenna System .....	121
6.6 Automatic cell planning.....	124
6.7 Energy Efficiency .....	124
6.8 Backhaul Network .....	125
6.9 Separate cell-site for indoor and outdoor coverage .....	127
6.10 Cell site monitoring and signal testing.....	127
<b>Chapter 7. Conclusions and Future Work .....</b>	<b>128</b>
7.1 Conclusions.....	128
7.2 Directions for Future Research .....	129
7.2.1 Accurate Terrain Profile to Analyze RF coverage .....	129
7.2.2 Appropriate Propagation Modeling.....	130
7.2.3 RF Coverage Planning and Analysis for Indoor .....	130
7.2.4 More Studies on Adaptive Cell-Sectorization.....	131
7.2.5 Extensive Studies on Advanced Antenna System.....	131
<b>References.....</b>	<b>133</b>

## LIST OF TABLES

Tables	Page
Table. 1.1 Evolution of mobile networks [1, 3-7].....	1
Table. 1. 2 Some key requirements of 5G networks.....	2
Table. 2.1 Characteristics of the antenna radiation pattern for a 5G cell. [30] .....	28
Table. 2.2 Half power beam width of uniform phased array antenna with various level of amplitude tapering. ....	39
Table. 2.3 Maximum directivity of the array antenna with different levels of amplitude tapering. ....	40
Table. 2.4 Simulation parameters to calculate total propagation loss.....	53
Table. 2.5 Simulation parameters to determine the required transmit power for strong signal coverage across the deployment area .....	62
Table. 3.1 The parameters employed for simulating RF coverage and computing Signal- to-Interference-plus-Noise-Ratio (SINR) values in the simulation .....	70
Table. 5.1 The parameters for simulating a 5G cell for analyzing non-line-of-sight signals .....	110
Table. 5.2 Relationship between received signal power involving one reflected path and types of building materials.....	112

Table. 5.3 Building Relationship between received signal power involving two reflected paths and types of building materials in contrast to Table 5.2.....	114
Table. 5.4 Relationship between received signal power involving one reflected path and types of building materials after beam steering in contrast to Table 5.2 .....	115
Table. 5.5 Relationship between received signal power involving two reflected path and types of building materials after beam steering in contrast to Table 5.3 .....	117

## LIST OF FIGURES

Figures	Page
Figure. 1.1 The relationship between channel capacity and signal-to-noise ratio, as given in Equation (1.1), is compared for four different bandwidths: 1GHz, 400MHz, 80MHz, and 20MHz. ....	4
Figure. 1.2 The relationship between received signal attenuation and propagation path length, as described in Equation (1.2), is examined for four different operating frequencies: 6GHz, 30GHz, 70GHz, and 100GHz. ....	6
Figure. 2.1 A visual depiction of a 5G cell coverage boundary. ....	12
Figure. 2.2 Depiction of a generic seven cell cluster.....	12
Figure. 2.3 The use of directional antennas for cell-sectorization: (a) shows an omni-cell with a single antenna providing 360-degree radiation, (b) shows a cell divided into three sectors, each with 120-degree radiation, and (c) shows a cell divided into six sectors, each with 60-degree radiation. [7] .....	13
Figure. 2.4 Illustration of $N = 7$ frequency planning: (a) a cluster of seven omni cells each with three frequency groups and (b) a cluster comprising seven sectorized cells, each divided into three sectors, and assigned one frequency group per sector.....	14
Figure. 2.5 Illustration of $N = 7$ frequency planning: (a) a cluster of seven omni cells each with three frequency groups and (b) a cluster comprising seven sectorized cells, each divided into three sectors, and assigned one frequency group per sector.....	16
Figure. 2.6 A visual illustration of cochannel interference.....	17
Figure. 2.7 A standard cluster consisting of seven cells, each replicated seven times with frequency reuse among cochannel cells (shaded cells).....	20

Figure. 2.8 A depiction of signal-to-cochannel interference ratio ( $C/I$ ) at the mobile receiver located at the boundary of its omnidirectional operating cell, under the influence of interfering signals from six cochannel interfering cells. ....	21
Figure. 2.9 A depiction of signal-to-cochannel interference ratio ( $C/I$ ) at the mobile receiver located at the boundary of its 3-sector cell, under the influence of interfering signals from two cochannel interfering cells. ....	22
Figure. 2.10 A depiction of signal-to-cochannel interference ratio ( $C/I$ ) at the mobile receiver located at the boundary of its 3-sector cell, under the influence of interfering signals from two cochannel interfering cells. ....	24
Figure. 2.11 Illustrate the relationship between the carrier-to-interference ratio ( $C/I$ ) and propagation loss factor ( $\gamma$ ), utilizing Equations (2.8), (2.9), and (2.10), in the context of a cluster that includes omni cells, three-sector cells, and six-sector cells. ....	25
Figure. 2.12 A 5G network layout consisting of 19 cells, with each cell having three sectors. [7].....	26
Figure. 2.13 An 8-by-8 uniform rectangular phased array antenna architecture for 70 GHz operating frequency .....	28
Figure. 2.14 Simulated 3D radiation pattern of a single rectangular patch antenna element and an 8-by-8 array comprised of rectangular patch antenna elements.....	29
Figure. 2.15 3D radiation pattern of an 8-by-8 antenna array composed of rectangular patch antenna elements, with varying element spacing: (a) element spacing of $\frac{1}{4}$ wavelength, (b) element spacing of $\frac{1}{2}$ wavelength, and (c) element spacing of one wavelength. ....	31

Figure. 2.16 3D radiation pattern of a rectangular patch antenna array without amplitude tapering, with various array sizes: (a) an 8-by-8 array, (b) a 16-by-16 array, and (c) a 32-by-32 array.....	32
Figure. 2.17 3D radiation pattern of a rectangular patch antenna array with amplitude tapering, varying in size: (a) an 8-by-8 array, (b) a 16-by-16 array, and (c) a 32-by-32 array .....	34
Figure. 2.18 Normalized power distribution of various arrays, with and without 30dB amplitude tapering: (a) the response of an 8-by-8 array, (b) the response of an 8-by-8 array with amplitude tapering, (c) the response of a 16-by-16 array, (d) the response of a 16-by-16 array with amplitude tapering, (e) the response of a 32-by-32 array, and (f) the response of a 32-by-32 array with amplitude tapering.....	35
Figure. 2.19 An illustration of the radiation pattern of an 8-by-8 antenna array, which displays the half power beam width, main lobe, minor lobes, and grading lobe.....	36
Figure. 2.20 Comparison of the normalized power distribution of various arrays with 30dB and 50dB amplitude tapering in contrast to Figure 2.18: (a) the response of an 8-by-8 array with 30dB amplitude tapering, (b) the response of an 8-by-8 array with 50dB amplitude tapering, (c) the response of a 16-by-16 array with 30dB amplitude tapering, (d) the response of a 16-by-16 array with 50dB amplitude tapering, (e) the response of a 32-by-32 array with 30dB amplitude tapering, and (f) the response of a 32-by-32 array with 50dB amplitude tapering.....	38
Figure. 2.21 RF signal attenuation in free space as a function of operating frequency obtained using Equation (1.2) for cell ranges of 100m, 600m, and 1200m.....	43

Figure. 2.22 RF signal attenuation at various operating frequencies for a 100m propagation path obtained using Equation (2.13) for the rainfall rates of 1 mm/hr, 6 mm/hr, 20 mm/hr, 50 mm/hr, and 100 mm/hr .....	45
Figure. 2.23 RF signal attenuation over distance for 70 GHz operating frequency obtained using Equation (2.13) for the rainfall rates of 6 mm/hr, 50 mm/hr, and 100 mm/hr	46
Figure. 2.24 RF signal attenuation at different operating frequencies obtained using Equation (2.15) for light fog, moderate fog, and thick fog.....	47
Figure. 2.25 RF signal attenuation at different operating frequencies with a 100m cell radius obtained using Equations (2.16) and (2.17) for the water vapor density of 0 g/m <sup>3</sup> (i.e., dry air) and 30 g/m <sup>3</sup> (i.e., humid air).....	51
Figure. 2.26 RF signal attenuation over propagation path length at 70GHz operating frequency obtained using Equations (2.16) and (2.17) for the water vapor density of 0 g/m <sup>3</sup> (i.e., dry air), 7.5 g/m <sup>3</sup> , and 30 g/m <sup>3</sup> (i.e., humid air).....	52
Figure. 2.27 Total signal attenuation at various operating frequencies obtained using Equation (2.13) for the free space and realistic propagation environment .....	54
Figure. 2.28 Received signal attenuation (dB) at various operating frequencies (GHz) obtained using Equation (2.26) for the path length of 100m, 200m, and 400m .....	55
Figure. 2.29 A visual representation of the antenna feeder cable system in a 5G cell-site .....	56
Figure. 2.30 The relationship between transmit signal power and received signal power obtained using Equation (2.27) for the operating frequency of 30GHz and 70GHz	61



Figure. 2.31 Received signal power (dBm) at various operating frequencies (GHz) obtained using Equation (2.27) for the cell radius of 100m, 200m, 300m, and 400m .....	66
Figure 3.1 A map of RF coverage and signal strength for a collection of seven cell sites. Each site is equipped with three sectors, each with one antenna element. ....	71
Figure 3.2 A map of RF coverage and SINR for a collection of seven cell sites. Each site is equipped with three sectors, each with one antenna element.....	72
Figure 3.3 A map of RF signal strength for a collection of seven cell sites. Each site is equipped with three sectors, each with an 8-by-8 Antenna Array in contrast to Figure 3.1.....	73
Figure 3.4 A map of RF coverage and SINR for a collection of 19 cell sites. Each site is equipped with three sectors, each with an 8-by-8 Antenna Array in contrast to Figure 3.2.....	74
Figure 3.5 A map of RF signal strength for a group of 19 cell sites, each of which is equipped with three sectors, each featuring a 16-by-16 Antenna Array in contrast to Figure 3.3 .....	75
Figure 3.6 A map of RF coverage and SINR for a collection of 19 cell sites. Each site is equipped with three sectors, each with a 16-by-16 Antenna Array in contrast to Figure 3.4 .....	76
Figure 3.7 A visual representation of RF coverage incorporating antenna downtilt [7] ..	78
Figure 3.8 An illustration showing the antenna downtilt of a base station using (a) a standard antenna, (b) mechanical downtilt, and (c) electrical downtilt. [7] .....	79

Figure 3.9 A comparison of RF signal strength is depicted for a group of seven cell sites in contrast to Figures 3.1, 3.3, and 3.5. Each site is fitted with three sectors, each having 8-by-8 antenna arrays and different downtilt angles.....	81
Figure 3.10 A comparison of RF signal strength is depicted for a group of seven cell sites in contrast to Figures 3.9. Each site is fitted with three sectors, each having 16-by-16 antenna arrays and different downtilt angles. ....	82
Figure 3.11 A comparison of RF signal strength among seven cell sites, each with three sectors and a transmitter using an 8-by-8 uniform phased array antenna for operating frequencies of 30GHz and 70GHz, in contrast to Figure 3.10.....	83
Figure 3.12 Comparison of RF Signal Strength Across Seven Cell Sites at 70GHz Frequency with Varying Antenna Heights (10m, 20m, 25m, and 30m) Using an 8-by-8 Uniform Phased Array Antenna and 30° Antenna Downtilt, Contrasted with Figures 3.9 and 3.11.....	85
Figure 4.1 An illustration showing a revised 5G cell architecture in comparison to Figure 2.3: (a) a 5G cell divided into nine sectors, each with a 40-degree radiation pattern, and (b) a 5G cell divided into twelve sectors, each with a 30-degree radiation pattern. ....	87
Figure 4.2 A comparison of RF coverage and SINR is depicted for a group of seven cells by varying the number of sectors per cell and equipped with 8-by-8 antenna arrays in each sector.....	92
Figure 4.3 A comparison of RF coverage and SINR is depicted for a group of seven cells by varying the number of sectors per cell and equipped with 16-by-16 antenna arrays in each sector in contrast to Figure 4.2. ....	93

Figure 4.4 The power consumption of a cell site in dynamic mode as function of the number of transmitters per sector, obtained using Equation (4.1) and (4.3), for a cell with 3-sectors, 6-sectors, 9-sectors, and 12-sectors .....	97
Figure 4.5 The power consumption of a cell site in sleeping mode as function of the number of transmitters per sector, obtained using Equation (4.2) and (4.3), for a cell with 3-sectors, 6-sectors, 9-sectors, and 12-sectors .....	98
Figure 4.6 An illustration of a phased array antenna structure with eight antenna elements. Each of these elements includes a T/R (Transmit/Receive) switch and steering circuitry .....	100
Figure 4.7 A visual representation of a phased array antenna configuration featuring two subarrays, each equipped with four antenna elements. Each of these elements includes a T/R (Transmit/Receive) switch and steering circuitry, in contrast to Figure 4.6 .....	101
Figure 4.8 A visual representation of a phased array antenna configuration featuring two subarrays with duel feed architecture, each equipped with four antenna elements. Each of these elements includes a T/R (Transmit/Receive) switch and steering circuitry, distinguishing it from the setups depicted in Figures 4.6 and 4.7 .....	102
Figure 4.9 A comparison of array responses for a phased array operating at a frequency of 70GHz for different numbers of radiating elements per subarray in contrast to Figure 2.1: (a) array response with 16 radiating elements per subarray, (b) array response with 8 radiating elements per subarray, and (c) array response with 4 radiating elements per subarray .....	103

Figure 4.10 An array response comparison for a 70GHz phased array for different beam steering configurations, as compared to Figure 4.9: (a) array response with no beam steering using 16 radiating elements per subarray, and (b) array response with 20 <sup>0</sup> beam steering using 16 radiating elements per subarray .....	104
Figure 4.11 A comparison of cell site energy consumption gain as a function of the number of transmitters per sector for various numbers of active sectors and 16 hours of observation time: (scenario 1) twelve sectors active for 8 hours and nine sectors active for the remaining 8 hours, (scenario 2) twelve sectors active for 8 hours and six sectors active for the remaining 8 hours, and (scenario 3) twelve sectors active for 8 hours, nine sectors active for 4 hours, and six sectors active for the remaining 4 hours.....	107
Figure 5.1 Visualize Buildings Data of Chicago downtown, IL, USA.....	109
Figure 5.2 Radio frequency coverage of a 5G cell and ray tracing involving a single reflected path.....	111
Figure 5.3 Radio frequency coverage of a 5G cell and ray tracing involving two reflected paths in contrast to Figure 5.2.....	113
Figure 5.4 Radio frequency coverage of a 5G cell and ray tracing involving a single reflected path after beam steering in contrast to Figure 5.3.....	115
Figure 5.5 Radio frequency coverage of a 5G cell and ray tracing involving two reflected paths after beam steering in contrast to Figure 5.3. ....	116

## LIST OF ACRONYMS

4G	Fourth Generation
5G	Fifth Generation
5G NR	Fifth Generation New Radio
MNO	Mobile Network Operator
RF	Radio Frequency
RAN	Radio Area Network
BS	Base Station
AAS	Advanced Antenna System
SISO	Single Input and Single Output
SIMO	Single Input and Multiple Outputs
MISO	Multiple Inputs and Single Output
MIMO	Multiple-Inputs and Multiple-Outputs
SINR	Signal to Interference plus Noise Ratio
SNR	Signal-to-Noise Ratio
C/I	Carrier-to-Interference ratio
BER	Bit Error Rate
ECG	Energy Consumption Gain
QoS	Quality of Service
ISD	Inter-site Distance
HPBW	Half Power Beamwidth
FEC	Forward Error Control
LPDC	Low Density Parity Check

RLB	Radio Link Budget
ITU	International Telecommunication Union
IMT	International Mobile Telecommunications
3GPP	3rd Generation Partnership Project
ICT	Information and Communications Technology
LTE	Long Term Evolution
Tx	Transmitter
Rx	Receiver
DL	Downlink
UL	Uplink
LOS	Line of Sight
NLOS	Non-Line of Sight

# CHAPTER 1

## INTRODUCTION

### 1.1 Motivation

The first generation of the cellular network (i.e., 1G) started service in the late 1980s with analog telephony, and has evolved to the current generation where the users and devices experience network connectivity to the internet in addition to telephone and other basic services [1, 2]. The primary goal of each evolution is to provide seamless connectivity anytime, and anywhere the user wants. It will also bring new use cases and services (e.g., mobile internet in 3G) to bring more users to the network and continue the economic growth. Table 1.1 shows the evolution of mobile networks with the key services and deployment years [1, 3-7].

Table. 1.1 Evolution of mobile networks [1, 3-7]

Generation	Year	Key Services	Primary Differentiator
1G	1980s	Analog voice calls	Mobility
2G	1990s	Mobile voice calls and messaging	Digital
3G	2000s	Phone calls, messaging, mobile web browsing	Broadband internet and smartphones
4G	2010s	All 3G services and mobile video consumption with higher data speed	Faster broadband internet and lower latency
5G	2020s	Massive mobile broadband, massive Internet of Things (IoT), industrial automation	Digitalization of industry, ultra-low latency, ultra-high availability, ultra-speed, and ultra-reliability

The new use cases and services introduced by the previous generation cellular networks are mainly used by humans (e.g., phone calls, messaging, and web browsing). The 5G network will have advanced network requirements listed in Table 1.2 [1, 8-10]. It will enable new use cases and services for the following three main areas [9, 11]:

- *Massive mobile broadband*: Provide extremely high data rates for human-centric devices (e.g., smartphone, smartwatch, tablet, laptop, pc, etc.) and regular use cases (e.g., telephone, gaming, media, etc.).
- *Extensive communication for autonomy*: Provide interconnection of devices (e.g., sensors, actuators, motors, etc.) to share data and control remotely. It enables wide application areas including industry, household electronics, cars, agriculture, health, etc.
- *Ultra-reliable low latency*: The high reliability and ultra-low latency will enable real-time control and human collaboration with devices. It also enables broad application areas, including autonomous vehicles, augmented/virtual reality (i.e., AR/VR), remote health services, remote agriculture services, cloud robotics, etc.

Table. 1. 2 Some key requirements of 5G networks

Requirements	Values
Peak data rate	Downlink (20Gb/s) and uplink (10Gb/s)
Latency	User plane (1m-4ms) and control plane (20ms)
Reliability	99.999%
Availability	99.999%
Connection density	1,000,000 devices per km <sup>2</sup>



The successful implementation of the 5G network will allow interconnecting new types of devices, including household electronic devices, cars, moving robots, sensors, Internet of Things (IoT), Machine-to-Machine (M2M) communication, etc.[12-17]. According to the Ericsson forecasts, IoT connections are expected to reach 27 billion worldwide by 2026, a 13% from 2020 [1]. Over that same time period, global coverage for 5G communication is expected to rise from 20% to 60%, and an increase in worldwide mobile subscriptions from 7.8 billion to 8.8 billion [1]. Therefore, it will be the fastest global rollout for any generations.

However, the 5G network services are no longer hype. The MNOs worldwide (e.g., Verizon and AT&T in the USA) started deploying 5G networks in mid-frequency bands (i.e., 3-6 GHz) with the current 4G cellular networks. In recent years, the global data traffic demands have grown exponentially. For example, the Ericsson Mobility report projected that the global data traffic level will increase to 160 exabytes per month by 2025 from 38 exabytes per month in 2019 [18]. But, the maximum channel capacity is bound by the Bandwidth (BW) and Signal-to-Noise Ratio (SNR) according to Shannon's channel capacity formula, Equation (1.1) [19].

$$C = B * \log_2 (1 + S/N) \quad (1.1)$$

Where, B is the channel bandwidth, S is the signal power, and N is the noise power.

The straightforward way to increase the network capacity is to add more bandwidth, shown in Figure 1.1. It drives the MNOs to seek higher bandwidth which is available in a higher frequency spectrum. For example, the current 4G Network can offer the channel bandwidth from 5MHz, 10MHz, and 20MHz. But, the 5G mid-bands can offer 50MHz and 100MHz, whereas the 5G high-band can offer 400~800MHz of Bandwidth [20].

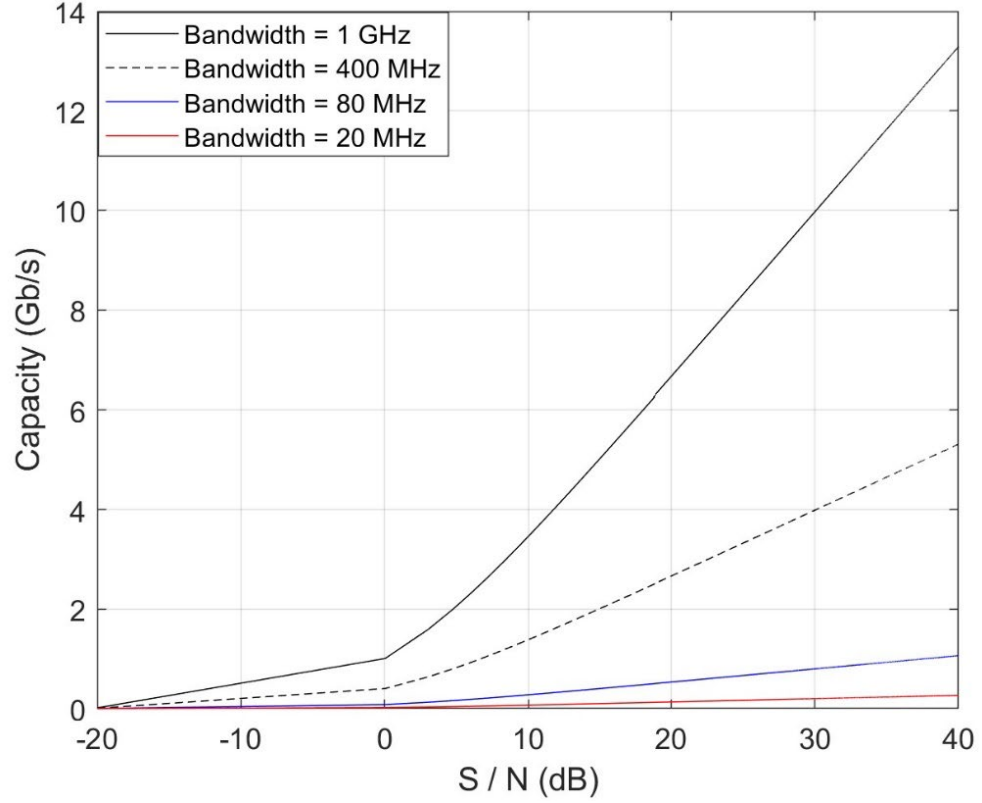


Figure. 1.1 The relationship between channel capacity and signal-to-noise ratio, as given in Equation (1.1), is compared for four different bandwidths: 1GHz, 400MHz, 80MHz, and 20MHz.

Since the radiated energy from a transmitter (i.e., 5G cell) spreads over the surface as it propagates towards the receiver (i.e., user), the signal energy level attenuates. Some of transmitted energy will be captured by the receiver, while the remaining energy will be lost. In an ideal case, when there is a direct line of sight between isotropic transmitter and receiver antenna without any absorbing or reflecting obstacles, the total signal attenuation known as free-space path loss ( $L_{FS}$ ) can be calculated by Equation (1.2) [21, 22].

$$L_{FS} = \left( \frac{4 \pi d}{\lambda} \right)^2 \quad (1.2)$$

Where  $\lambda = c / f$  is the wavelength of the transmitted signal,  $c$  is the speed of light ( $3 \times 10^8$  m/s), and  $f$  is the operating frequency of the transmitted signal. The propagation path length is represented by  $d$ .

Figure 1.2 shows the free space propagation loss versus propagation path length for different operating frequencies. Results show that the higher frequency spectrum has extremely high propagation loss that increases with path length. Additionally, the outdoor deployment environment will also include additional signal impairments such as precipitation, dust, foliage, and multipath propagation, etc., which reduces the receive signal level [23-25].

But, the 5G network requires extremely high availability (i.e., 99.999%) and reliability (i.e., 99.999%) [9, 26] which will limit the cell site coverage range in the high-frequency spectrum (i.e., 24GHz –100 GHz) to several hundred meters, as opposed to several kilometers in a 4G cell. Hence, the MNOs will need to deploy hundreds of new cell sites to provide comparable coverage to a 4G cell. The viable cell site locations will be limited due to several factors, including availability of electric power, load-bearing capabilities, government and private owner approval, and operating costs, etc. Therefore, it will be a big challenge for the MNOs to plan the massive number of new cells accurately, acquire the physical locations for each cell, and complete the deployments.

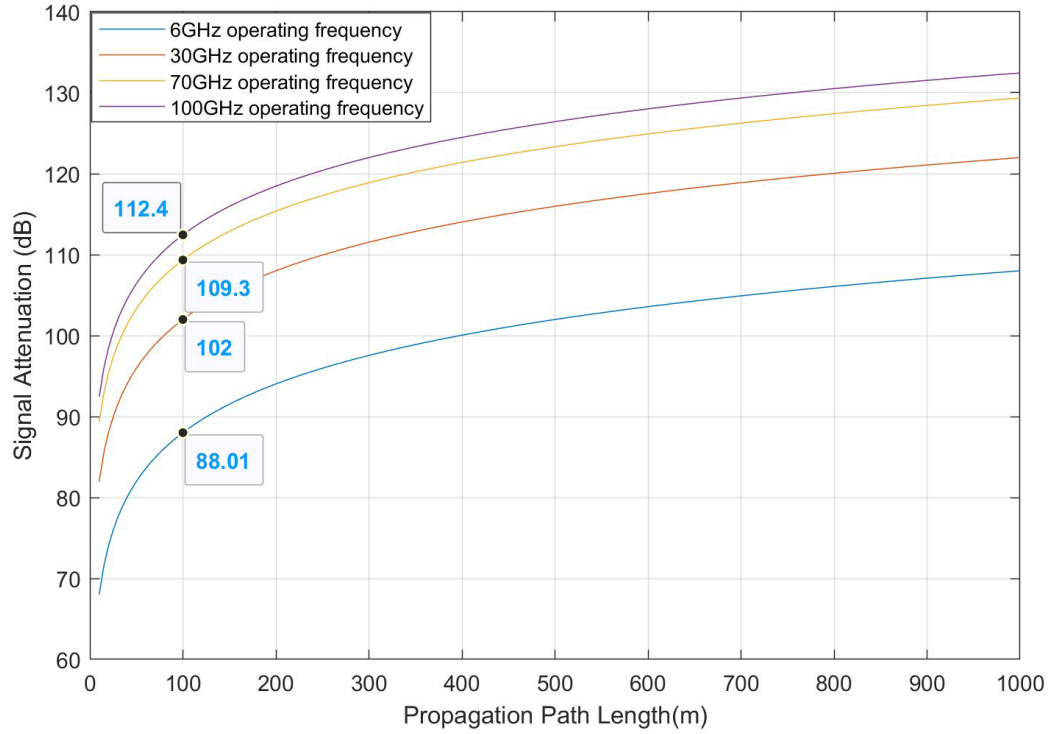


Figure. 1.2 The relationship between received signal attenuation and propagation path length, as described in Equation (1.2), is examined for four different operating frequencies:

6GHz, 30GHz, 70GHz, and 100GHz.

The 5G network will require optimal RF coverage (i.e., close to 100% coverage) for any deployment areas to meet the high network availability (i.e., 99.999%) and reliability (i.e., 99.999%). Therefore, the RF coverage planning will be of utmost importance for the MNOs to successfully plan and deploy a massive number of new cells. In addition, the RF coverage planning and analysis can also provide the approximate receive signal characteristics throughout the deployment area without physical signal testing in the area. It is the primary motivation of this Dissertation, and the findings will help the system designer to:

- Identify appropriate cell site location.

- Guidance on the selection of components for 5G cell transmitters (e.g., antenna types, beamwidth, directivity, size of antennas, etc.).
- Adjust the antenna height and tilt angle to improve RF coverage.
- Estimate the RF signal propagation loss throughout the deployment area.
- Identify the maximum cell range.
- Calculate the appropriate transmitted power based on the propagation loss.
- Appropriately positioned the neighboring cells to reduce the coverage holes.
- Find the best network planning in a higher frequency spectrum.
- Optimize cell site power consumption with adaptive cell-sectorization technique
- Estimate the RF signal characteristics in a multipath environment for the LOS (line-of-sight) and NLOS (non-line-of-sight) users and how to reduce multipath signals.

## **1.2 Contributions of the Dissertation**

My key contributions of this Dissertation are summarized below:

- RF coverage planning, analysis, and optimization for the 70GHz operating frequency using both nine and twelve sectors per cell.
- Innovative adaptive cell-sectorization technique enabling dynamic adjustments to the number of sectors within a cell to optimize RF coverage.
- A cell site energy-saving technique that leverages adaptive cell-sectorization for deployment scenarios with variable traffic to improve power efficiency.
- Optimization of RF coverage for non-line-of-sight scenarios at the 70GHz operating frequency.

- Practical guidelines to overcome deployment challenges of 5G networks operating in the millimeter band.

### **1.3 Dissertation Outline**

The rest of the Dissertation is organized as follows:

Chapter 2 includes the fundamentals of RF coverage planning for the 5G network.

Chapter 3 presents RF coverage simulation with traditional three sectors cell architecture and investigates the potential challenges. It then proposes an advanced antenna system to improve the RF coverage.

Chapter 4 introduces higher-order cell-sectorization and proposes an adaptive cell-sectorization method that ensures higher capacity in peak-hours traffic and saves energy in off-peak hours traffic.

Chapter 5 studies the RF coverage analysis and optimization at non-line-of-sight location.

Chapter 6 investigates the 5G network deployment challenges. It then provides future research directions to overcome these challenges.

Chapter 7 concludes the Dissertation. Some potential open problems and future research directions are then presented in Section 8.2.

### **1.4 Publications**

#### **Book Chapter**

- B 1. **M. M. Ahamed** and S. Faruque, "5G Backhaul: Requirements, Challenges, and Emerging Technologies," in Broadband Communications Networks - Recent Advances and Lessons from Practice, A. Haidine and A. Aqqal, Eds., ed: InTech, ISBN 978-953-51-5810-3, September 19th, 2018.

## Journal Publications

- J 1. **M. M. Ahamed** and S. Faruque, "5G Network Coverage Planning and Analysis of the Deployment Challenges," *Sensors*, vol. 21, no. 19, p. 6608, 2021. [Online]. Available: <https://www.mdpi.com/1424-8220/21/19/6608>.
- J 2. **M. M. Ahamed** and S. Faruque, "RF Coverage Planning with Adaptive Higher-Order Cell-Sectorization for the 5G Network and Beyond", *Journal of Communications and Networks*, 2021 [submit by October].

## Conference Proceedings

- C 1. **M. M. Ahamed** and S. Faruque, "Design a 5G Backhaul Network Based on Free Space Optics and Analyze the Link Performances," 2021 4th International Conference on Information and Computer Technologies (ICICT), 2021, pp. 187-193, doi: 10.1109/ICICT52872.2021.00038.
- C 2. **M. M. Ahamed** and S. Faruque, "Hybrid Driving Assist Technology for a Smart Car Based on Driver Heart Rate", World Conference & Expo on Biomedical Engineering, Miami, USA, July 16-17, 2018.
- C 3. **M. M. Ahamed**, Saleh Faruque, and Sunil Kumar Gaire "Laser radio: backhaul solution for 5G networks", *Proc. SPIE 9979, Laser Communication and Propagation through the Atmosphere and Oceans V*, 99790C (19 September 2016); doi: 10.1117/12.2237952.
- C 4. S. K. Gaire, S. Faruque, and **M. M. Ahamed** "OptoRadio: a method of wireless communication using orthogonal M-ary PSK (OMPSK) modulation", *Proc. SPIE*

9979, Laser Communication and Propagation through the Atmosphere and Oceans  
V, 99790D (19 September 2016); doi: 10.1117/12.2237962

- C 5. **M. M. Ahamed** and S. Faruque, "Propagation factors affecting the performance of  
5G millimeter wave radio channel," 2016 IEEE International Conference on Electro  
Information Technology (EIT), 2016, pp. 0728-0733, doi:  
10.1109/EIT.2016.7535329.



## **CHAPTER 2**

### **RF COVERAGE PLANNING**

#### **2.1 Introduction**

The 5G network will require nearly ubiquitous network coverage to meet the high network availability (i.e., 99.999%) and network reliability (i.e., 99.99%) requirements of the standard. Therefore, optimum network coverage planning will be the key to ensure all the network requirements of 5G are met and provide the requested services to the users. This section first describes the fundamentals of RF coverage. It then introduces a novel method for 5G RF coverage planning, encompassing aspects such as network layout planning, transmitter site design, and propagation modeling.

#### **2.2 What is Network Coverage?**

The network coverage refers to the region around the base station/cell site where the user can send any service requests and successfully connect with the cell site to receive the services. The radius of a cell, as depicted in Figure 2.1, refers to the farthest distance from the cell site that a user can send service requests and receive uninterrupted services. The cell radius establishes the boundary of maximum cell coverage, beyond which a user cannot establish any connections. It also plays a role in determining the Inter-Site Distance (ISD), which is the minimum distance between adjacent cells required to prevent multiple dominant signals in the deployment area.

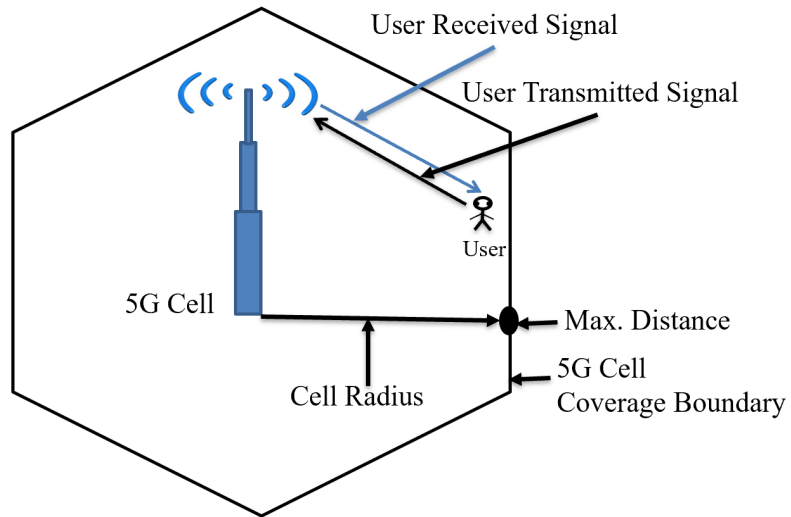


Figure. 2.1 A visual depiction of a 5G cell coverage boundary.

### 2.3 Cell-Sectorization

Traditionally the cell sites are deployed in a group of cells called a cluster, shown in Figure 2.2. Each cell can have one omnidirectional antenna (Omni-cell) or multiple directional antennas called sectoring, shown in Figure 2.3.

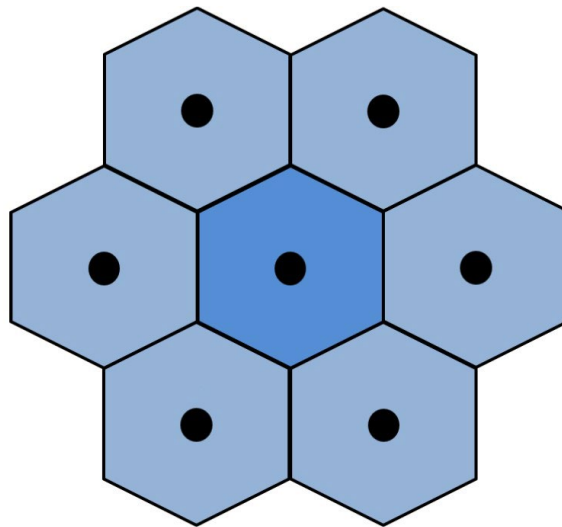


Figure. 2.2 Depiction of a generic seven cell cluster

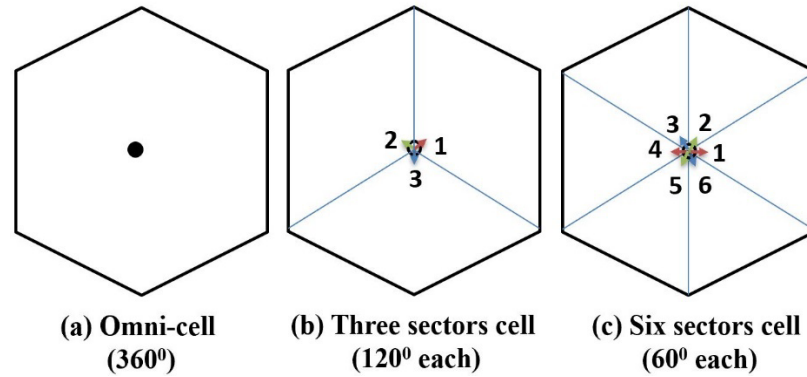


Figure. 2.3 The use of directional antennas for cell-sectorization: (a) shows an omni-cell with a single antenna providing 360-degree radiation, (b) shows a cell divided into three sectors, each with 120-degree radiation, and (c) shows a cell divided into six sectors, each with 60-degree radiation. [7]

## 2.4 Frequency Planning

The Federal Communications Commission (FCC) issues licenses for operating cellular communication systems within specific frequency bands, referred to as RF spectrum allocation [27, 28]. These frequency bands are further subdivided into smaller channels, which are then allocated to a cluster of cells using a technique called frequency planning [19, 28, 29]. Given the finite number of channels due to limited RF spectrum allocation, they are reused to serve various geographical regions [29]. As an illustration, if there are twenty-one available channels, they are distributed among a cluster of seven cells, with each cell assigned three channels [29]. Subsequently, these cell clusters, along with their assigned channels, are strategically positioned in adjacent geographic regions to extend coverage to neighboring areas. This process is replicated as needed to provide coverage for a given geographic area, serving as the fundamental principle of frequency reuse planning [19, 28, 29].

Numerous frequency planning or channel assignment techniques are available in the realm of cellular communication. Presented below are two of the most widely adopted frequency planning techniques [28]:

#### 2.4.1 $N = 7$ frequency reuse plan

The  $N = 7$  frequency reuse plan, initially developed by V.H. MacDonald in 1979, involves the allocation of all available channels among seven cells within a cluster [27]. Figure 2.4 provides a visual representation of this technique, illustrating both a cluster of seven omni cells and a cluster of seven sectorized cells. In the omni cell configuration, each cell utilizes a single antenna, providing 360-degree radiation coverage. Conversely, in the sectorized cell configuration, each cell is divided into three sectors, with each sector employing a single antenna, delivering 120-degree radiation coverage.

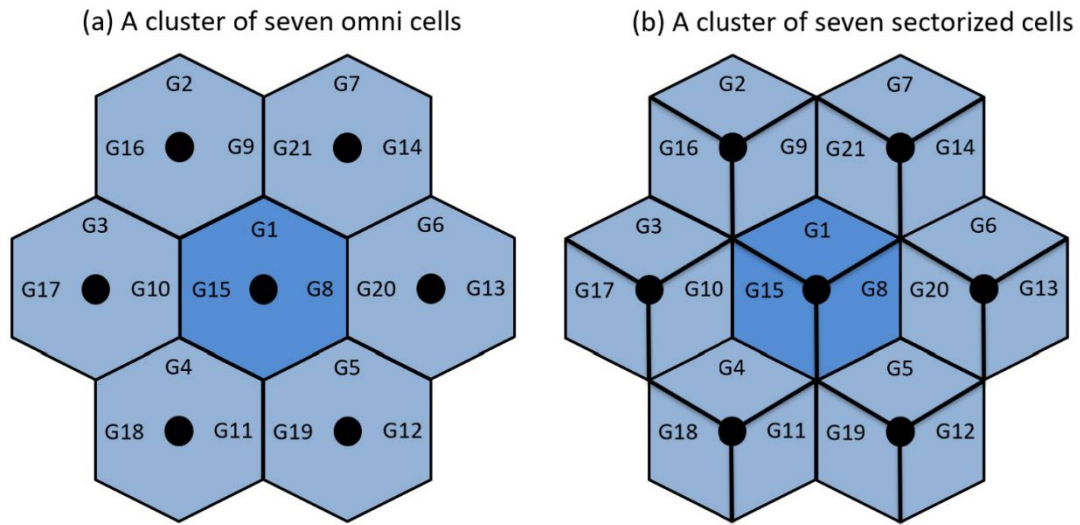


Figure. 2.4 Illustration of  $N = 7$  frequency planning: (a) a cluster of seven omni cells each with three frequency groups and (b) a cluster comprising seven sectorized cells, each divided into three sectors, and assigned one frequency group per sector

To illustrate this frequency reuse technique, let's assume that the available channels are grouped into 21 frequency groups, denoted as G1, G2, G3, G4, G5, G6, G7, G8, G9, G10, G11, G12, G13, G14, G15, G16, G17, G18, G19, G20, and G21. Each frequency group contains multiple frequencies, known as channels, and these frequency groups are evenly distributed among the cells. Specifically, each omni cell is assigned three frequency groups, while a sectorized cell receives one frequency group per sector, resulting in a total of three frequency groups per cell. Consequently, the total number of frequency groups per cluster remains consistent.

The channel distribution adheres to the  $N, N+7, N+14$  scheme, where  $N$  ranges from 1 to 7, corresponding to the cell number. For example, in the case of  $N = 1$ , omni cell-1 utilizes frequency groups 1, 8, and 15. In contrast, sectorized cell-1 employs frequency group 1 for sector 1, frequency group 8 for sector 2, and frequency group 15 for sector 3. This configuration effectively eliminates adjacent channel interference by ensuring that adjacent sites do not share adjacent channels.

#### **2.4.2** *$N = 3$ frequency reuse plan*

Figure 2.5 visually depicts the  $N = 3$  frequency reuse plan, featuring both a cluster of three omni cells and a cluster of three sectorized cells. In this frequency reuse technique, all available frequency groups are evenly distributed among the three cells within a cluster unlike the  $N = 7$  frequency plan.

To illustrate this frequency reuse plan, consider a scenario where the available channels are grouped into 9 frequency groups (in contrast to the 21 previously mentioned), denoted as G1, G2, G3, G4, G5, G6, G7, G8, and G9. These frequency groups are subsequently distributed equally among the cells. Specifically, each omni cell is allocated

three frequency groups, while a sectorized cell receives one frequency group per sector, resulting in a total of three frequency groups per cell. Consequently, the total number of frequency groups per cluster remains constant, but the total number of channels per frequency group is higher compared to the  $N = 7$  frequency plan.

The channel distribution follows the  $N, N+3, N+6$  scheme, where  $N$  varies from 1 to 3, corresponding to the cell number. For instance, in the case of  $N = 2$ , omni cell-2 utilizes frequency groups 2, 5, and 8. In contrast, sectorized cell-2 employs frequency group 2 for sector 1, frequency group 5 for sector 2, and frequency group 8 for sector 3.

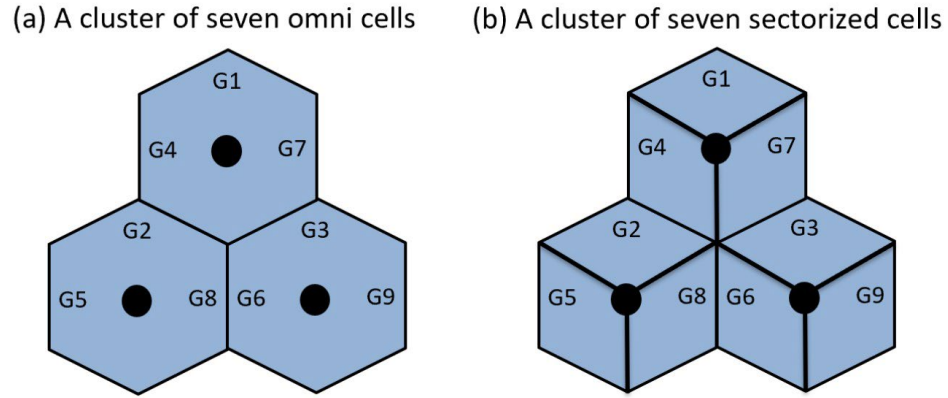


Figure. 2.5 Illustration of  $N = 3$  frequency planning: (a) a cluster of seven omni cells each with three frequency groups and (b) a cluster comprising seven sectorized cells, each divided into three sectors, and assigned one frequency group per sector

## 2.5 Carrier to Interference (C/I)

Cells that utilize an identical set of frequencies are referred to as the cochannel cells [19, 28]. When the distance between two cochannel cells is inadequate, it results in interference due to the simultaneous utilization of the same channel, which is known as cochannel interference [19, 27]. Given that available channels are reused to provide

coverage over a geographic area, mitigating cochannel interference is of paramount concern in any frequency reuse plan.

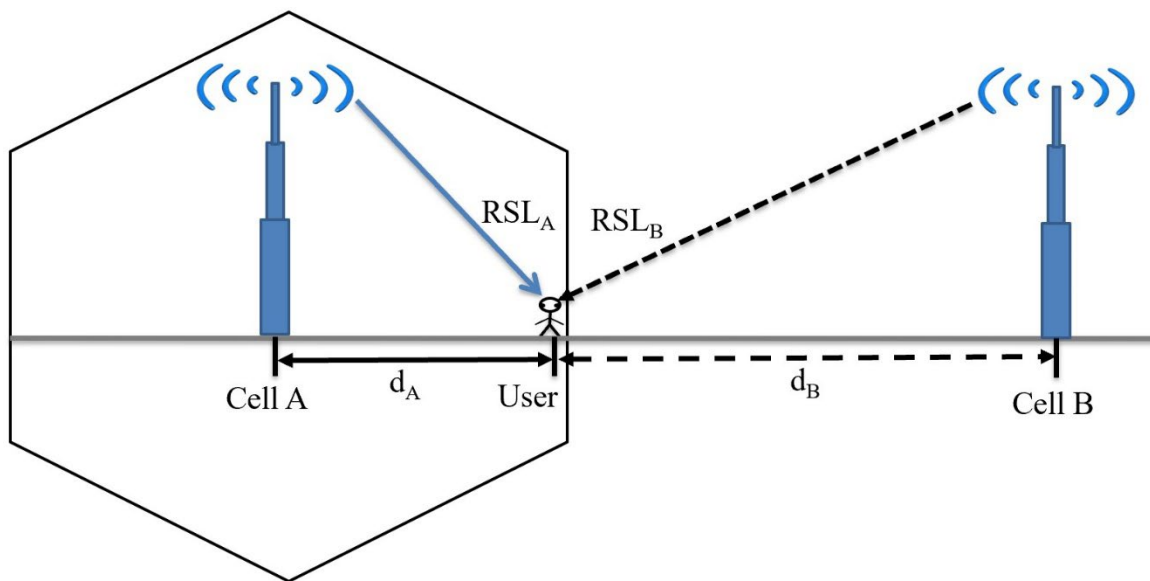


Figure. 2.6 A visual illustration of cochannel interference

Figure 2.6 illustrates a scenario of cochannel interference, where Cell A and Cell B both employ the same frequency. Consequently, when a user within Cell A communicates with Cell A, they also receive the same frequency signal from distant Cell B. The signal levels received by the user from Cell A and Cell B are computed using Equation 2.1 [29]:

$$\begin{aligned} RSL_A &\propto (d_A)^{-\gamma} \\ RSL_B &\propto (d_B)^{-\gamma} \end{aligned} \tag{2.1}$$

Here,  $RSL_A$  and  $RSL_B$  denote the received signal levels received by the user from Cell A and Cell B, respectively. The distance from the user to Cell A is represented as  $d_A$ , while the distance from the user to Cell B is denoted as  $d_B$ . The signal propagation loss is denoted by  $\gamma$ , and it is determined by the propagation environment, typically falling within the range of 2 to 5.

The ratio of received signal strength at the user is computed by Equation 2.2:

$$\frac{RSL_A}{RSL_B} = \left(\frac{d_A}{d_B}\right)^{-\gamma} = \left(\frac{d_B}{d_A}\right)^{\gamma} \quad (2.2)$$

Given that  $RSL_A$  is the desired signal received from the serving cell, we can redefine this signal as the carrier signal  $C$ . Let's also consider that the user is positioned at the cell edge, where the distance from Cell A to the user is equivalent to the cell radius  $R$ .

Conversely,  $RSL_B$  represents the undesired signal received from a distant Cell B. We can redefine this signal as the interference signal  $I$ , and the corresponding distance from the user to Cell B can be expressed as  $d_B = D$ , where  $D$  denotes the frequency reuse distance. Thus, Equation 2.2 can be expressed as a carrier-to-interference ratio ( $C/I$ ), attributed to a single interferer:

$$\frac{C}{I} = \left(\frac{R}{D}\right)^{-\gamma} = \left(\frac{D}{R}\right)^{\gamma} \quad (2.3)$$

Equation 2.3 can be written in dB as:

$$\frac{C}{I} (dB) = 10 \log \left(\frac{D}{R}\right)^{\gamma} \quad (2.4)$$

When considering the presence of  $k$  interference signals arriving at the user, the resulting carrier-to-interference ratio ( $C/I$ ) due to cochannel interference can be estimated using Equation 2.5. This estimation assumes that the path-loss exponent remains constant across the entire geographical coverage area.

$$\frac{C}{I} \approx \frac{\sum_{k=1}^{N_k} (D_k)^{\gamma}}{R^{\gamma}} \quad (2.5)$$



Here,  $D_k$  is the distance between the  $k^{\text{th}}$  interfering cochannel cell and the user. In a simplified scenario where  $D_k = D$  for  $k = 1, 2, 3, \dots, N_k$ , Equation 2.5 can be expressed in decibel as follows:

$$\frac{C}{I} \approx 10 \log \left[ \frac{1}{N_k} \cdot \left( \frac{D}{R} \right)^{\gamma} \right] \quad (2.6)$$

Hence, knowing the minimum C/I requirements allows for the determination of the optimal frequency reuse distance within a specific propagation environment. This frequency reuse distance, denoted as  $D$ , relative to the cell radius  $R$ , can be expressed as a ratio known as the frequency reuse ratio, represented by  $q = D/R$ . This ratio is also linked to the number of cells,  $N$ , in a cluster, as indicated below [27]:

$$q = \frac{D}{R} = \sqrt{3N} \quad (2.7)$$

### 2.5.1 *Methods of Locating Cochannel Cells*

The location of the nearest cochannel cell in a hexagonal geometry can be determined using two shift parameters,  $i$  and  $j$ , which measure the number of nearest neighboring cells between cochannel cells. These parameters,  $i$  and  $j$ , are separated by 60 degrees and can each take integer values starting from 0, 1, 2, 3, and so on. To determine the nearest cochannel cells using a reference cell as a starting point, follow these two steps [27]:

- Step 1: Move  $i$  number of cells along any chain of hexagons.
- Step 2: Turn 60 degrees counterclockwise and move  $j$  number of cells.

To exemplify the previous procedure, consider Figure 2.7 with  $i = 2$  and  $j = 1$ , where cochannel cells are shaded and labeled as A.

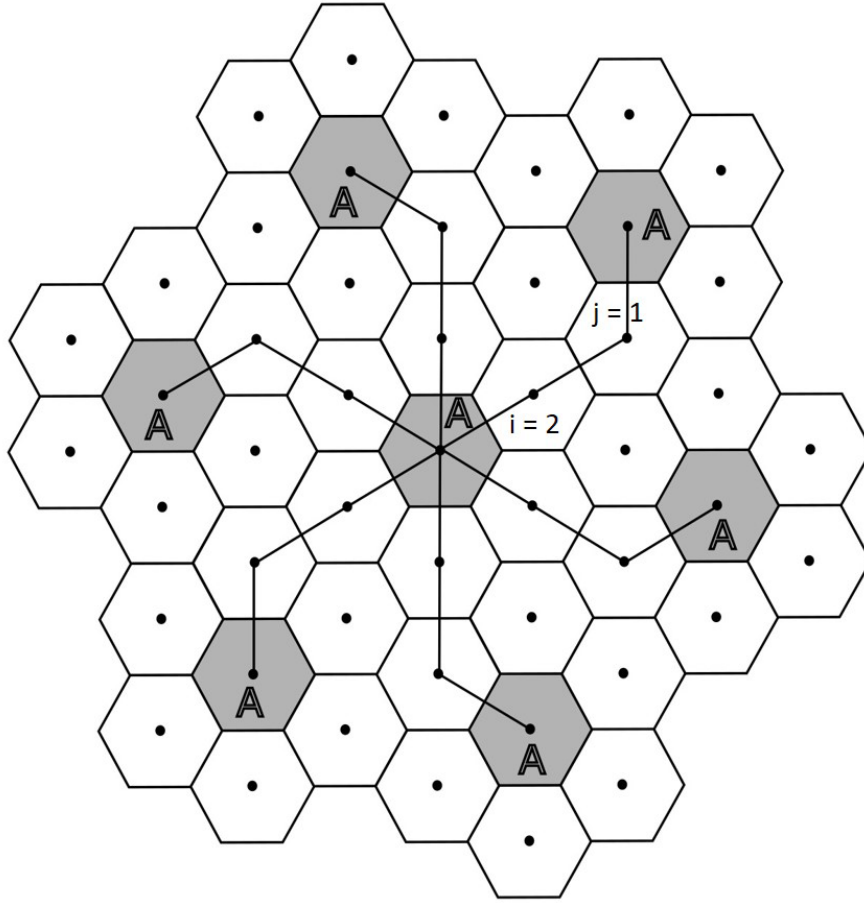


Figure. 2.7 A standard cluster consisting of seven cells, each replicated seven times with frequency reuse among cochannel cells (shaded cells)

### 2.5.2 Worst Case Analysis of C/I in an Omnidirectional Antenna System

Figure 2.8 demonstrates a standard cellular cluster consisting of seven omni cells, each implementing the  $N = 7$  frequency plan as described in section 2.4.1, and replicated seven times. As an illustration, the frequency group G1 is assigned to the cochannel cells (i.e., center cell) of each cluster. In a worst-case scenario, let's assume that the user is positioned at the cell edge of serving cell A, where the user receives a weak signal from the serving cell. Additionally, the user will receive interfering signals from six cochannel cells. If  $D$  represents the distance between the centers of any two cochannel cells, the

resulting carrier-to-interference ratio (C/I) due to cochannel interference can be calculated using Equation 2.8 [19]:

$$\frac{C}{I}(\text{omni}) \approx \frac{R^{-\gamma}}{2(D-R)^{-\gamma} + 2D^{-\gamma} + 2(D+R)^{-\gamma}} \quad (2.8)$$

Here, the cell radius of each cell is denoted as R, and the distance between the centers of any two cochannel cells is represented by D. The path loss exponent is symbolized as  $\gamma$ .

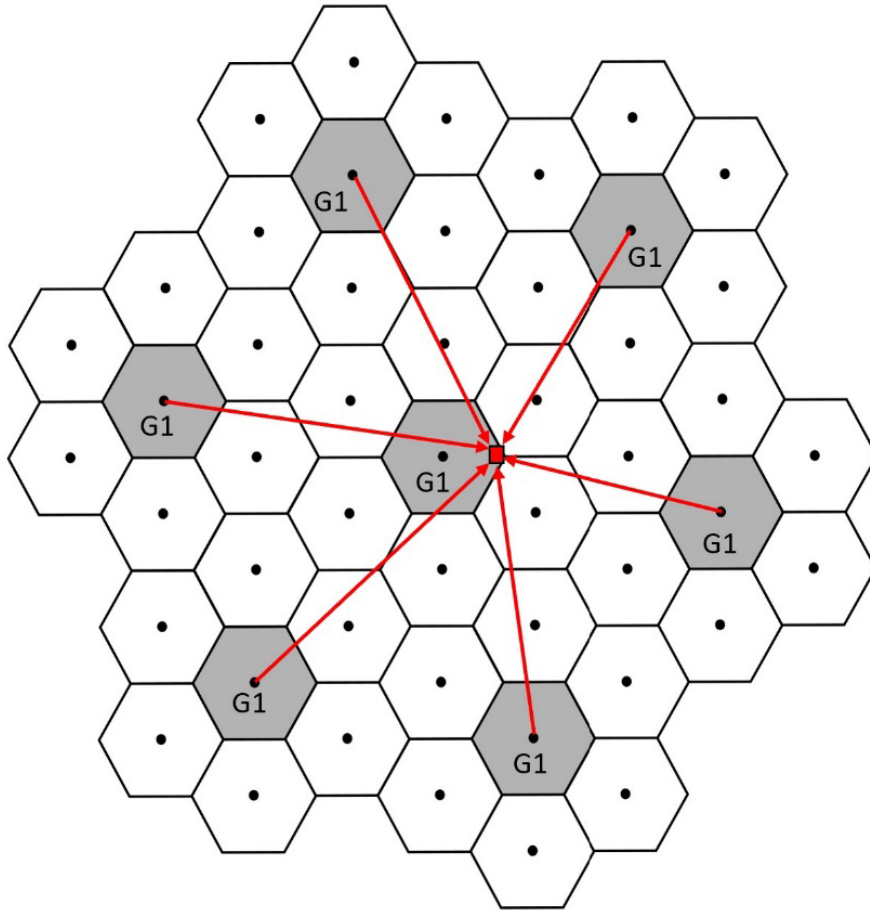


Figure. 2.8 A depiction of signal-to-cochannel interference ratio (C/I) at the mobile receiver located at the boundary of its omnidirectional operating cell, under the influence of interfering signals from six cochannel interfering cells.

### 2.5.3 Worst Case Analysis of C/I in a 3-Sector Cellular System

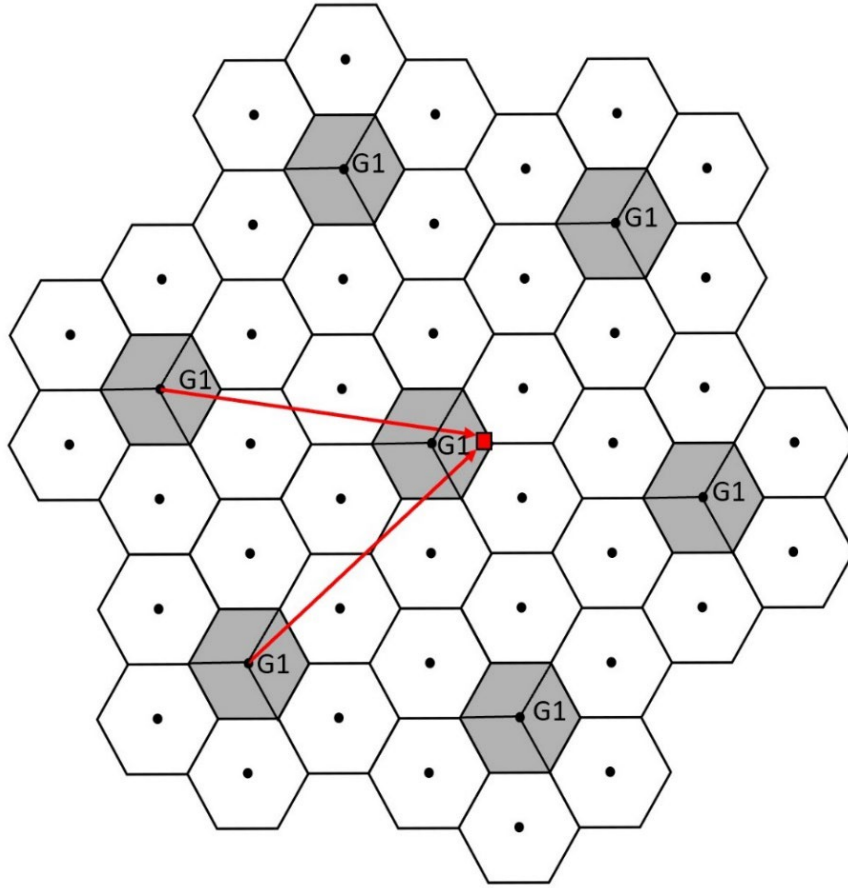


Figure. 2.9 A depiction of signal-to-cochannel interference ratio (C/I) at the mobile receiver located at the boundary of its 3-sector cell, under the influence of interfering signals from two cochannel interfering cells.

Figure 2.9 presents an illustration of a cellular cluster that comprises seven sectorized cells, each subdivided into three sectors. This cluster adheres to the  $N = 7$  frequency plan and is replicated seven times. For example, the frequency group G1 is allocated to sector one of each cochannel cell (i.e., the center cell) in each cluster. In a worst-case scenario, let's consider a user positioned at the cell edge of serving cell A and getting service from Sector S1. In this scenario, the user encounters cochannel interference

originating from the corresponding cochannel sectors, specifically S1, emanating from two out of the total six cochannel cells. Consequently, we can determine the carrier-to-interference ratio (C/I) due to cochannel interference using Equation 2.9 [19]:

$$\frac{C}{I}(3 - \text{sectors}) \approx \frac{R^{-\gamma}}{D^{-\gamma} + (D + 0.7 R)^{-\gamma}} \quad (2.9)$$

Here, the cell radius of each cell is denoted as R, and the distance between the centers of any two cochannel cells is represented by D. The path loss exponent is symbolized as  $\gamma$ .

#### 2.5.4 Worst Case Analysis of C/I in a 6-Sector Cellular System

Figure 2.10 illustrates a hexagonal cellular reuse pattern with a configuration of six sectors per cell. To elucidate the  $N = 7$  frequency reuse technique, let's assume that the available channels are organized into 42 frequency groups. Within these groups, each frequency group is comprised of multiple frequencies, referred to as channels. These frequency groups are then distributed uniformly among the cells, with each sector being assigned one frequency group. For example, the frequency group G1 is allocated to sector one of each cochannel cell (i.e., the center cell) in each cluster.

Now, if a user is receiving service from sector S1 of serving cell A while positioned at the cell boundary, the user will encounter interference signals solely from the corresponding cochannel sectors of one out of the total six cochannel cells. Consequently, the resulting carrier-to-interference ratio (C/I) due to cochannel interference can be calculated using Equation 2.10 [19]:

$$\frac{C}{I}(6 - \text{sectors}) \approx \frac{R^{-\gamma}}{(D + 0.7 R)^{-\gamma}} \quad (2.10)$$

Here, the cell radius of each cell is denoted as R, and the distance between the centers of any two cochannel cells is represented by D. The path loss exponent is symbolized as  $\gamma$ .

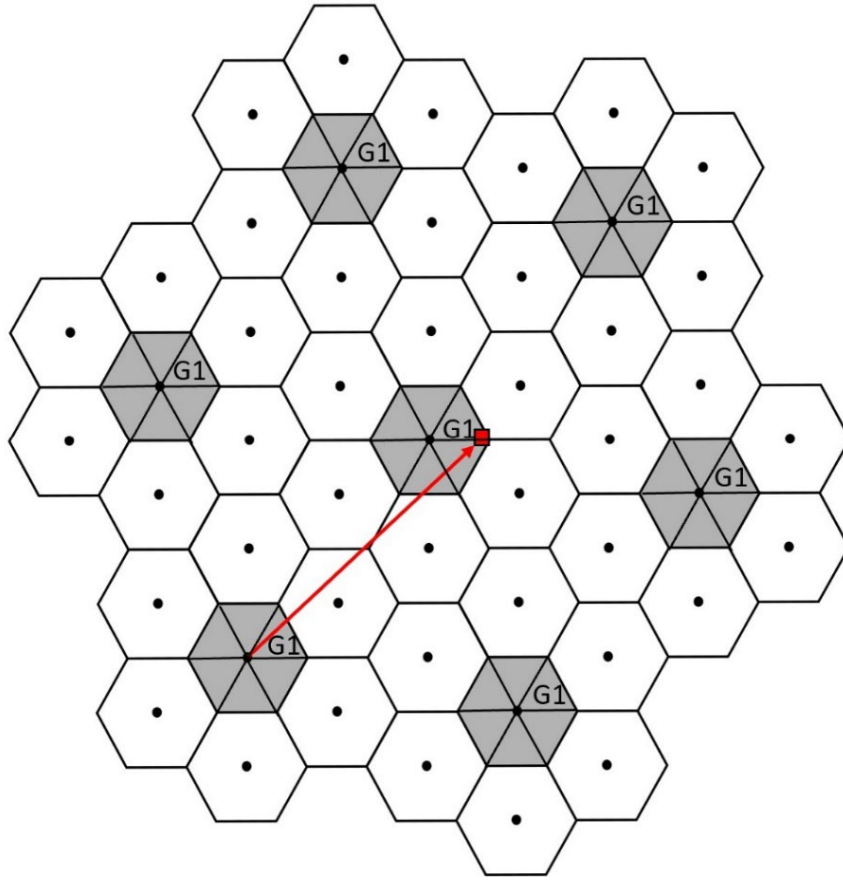


Figure. 2.10 A depiction of signal-to-cochannel interference ratio ( $C/I$ ) at the mobile receiver located at the boundary of its 6-sector cell, under the influence of interfering signals from one cochannel interfering cell.

Figure 2.11 presents a comparison of  $C/I$  values under various path loss exponents for omni cells, three-sector cells, and six-sector cells. The results indicate that six-sector cells consistently achieve superior  $C/I$  level compared to omni cells and three-sector cells across all path loss exponents. This improvement is attributed to a reduced number of interfering cells in the case of six-sector cells.

In Chapter 5, higher-order cell-sectorization strategies, such as nine and twelve sectors per cell, are explored as means to enhance RF coverage.

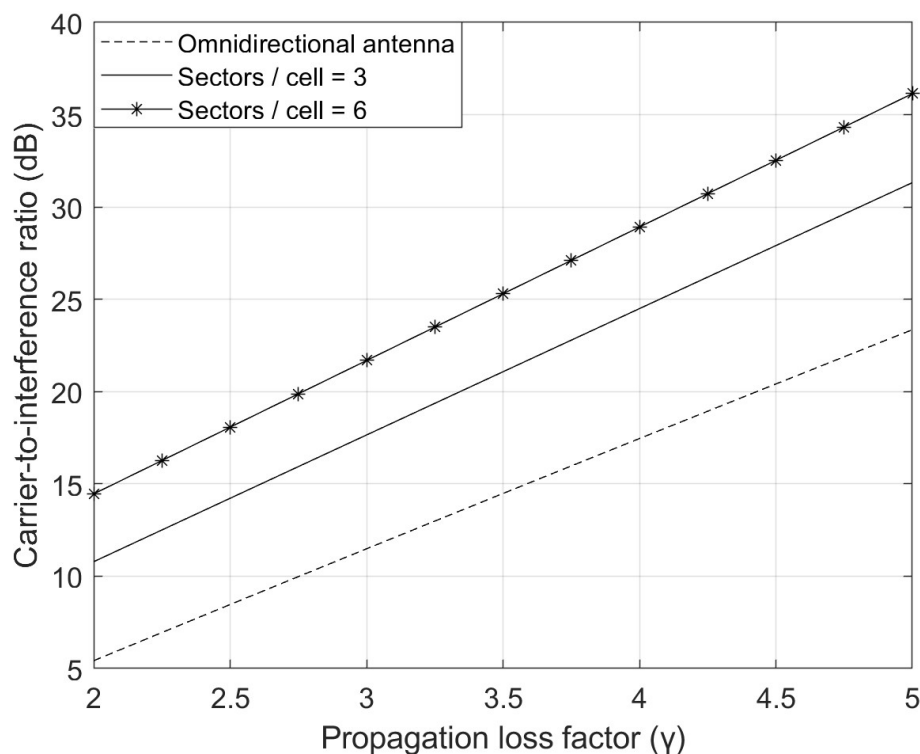


Figure. 2.11 Illustrate the relationship between the carrier-to-interference ratio (C/I) and propagation loss factor ( $\gamma$ ), utilizing Equations (2.8), (2.9), and (2.10), in the context of a cluster that includes omni cells, three-sector cells, and six-sector cells.

## 2.6 Network Layout

5G cells operating in higher frequency spectrum will provide coverage up to a few hundred meters, in contrast to several kilometers in 4G networks. This implies that to cover the same deployment area as a single 4G cell, MNOs will need to deploy hundreds of 5G cells. When multiple 5G cells are deployed to cover an area, a minimum Inter-Site Distance (ISD), illustrated in Figure 2.5, must be maintained between neighboring cells [30]. Users can get more than one dominant receive signal from nearby cell-sites if the minimum ISD

is not maintained called out of cell interference which can significantly degrade the network performances. Chapters 3 and 4 of this dissertation outline a fresh technique to compute 5G cell radius and Inter-Site Distance (ISD) by considering cell site parameters such as operating frequency, number of sectors per cell, antenna height, transmit power, and antenna downtilt angle.

To achieve faster 5G deployment, MNOs need to deploy a large number of cells for coverage of a specific region. This dissertation proposes a method where a group of cells with three sectors is formed initially, and can be scaled up as per deployment requirements. The network planning and RF coverage analysis in densely populated urban areas are emphasized in this dissertation. A hexagonal network layout consisting of 19 cells (i.e., tier-2), each having three sectors, is used as a test environment, shown in Figure 2.12.

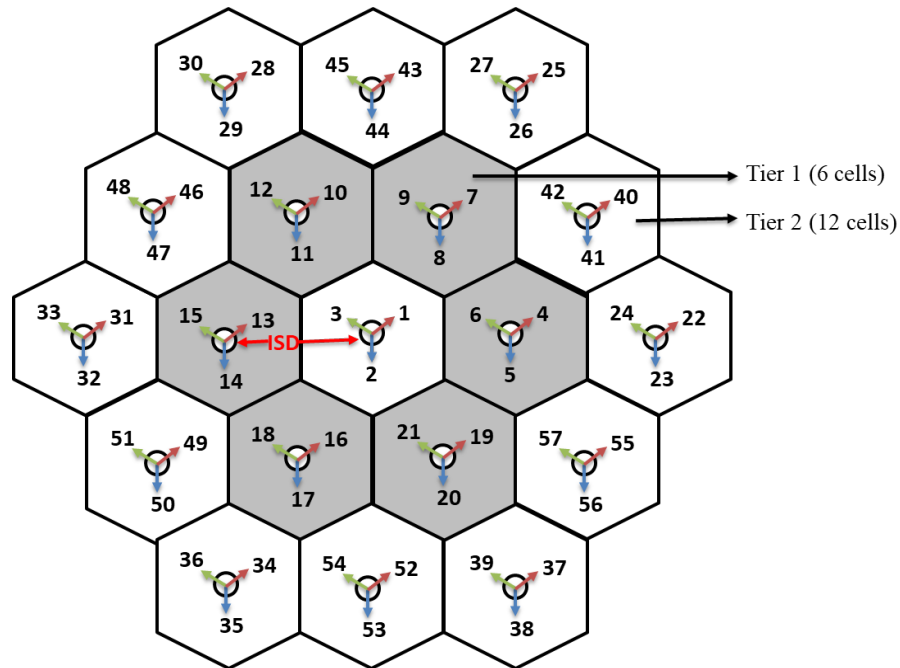


Figure. 2.12 A 5G network layout consisting of 19 cells, with each cell having three sectors. [7]



## 2.7 Define Transmitter Sites

Three transmitters are associated with each cell, shown in Figure 2.12. Each transmitter can be designed with a single antenna element or antenna array that contains a large number of antenna elements (e.g., 256 antenna elements for 30 GHz). Since the 5G network will use higher frequency bands (i.e., millimeter-wave bands), it is more practical to integrate a large number of antenna elements into a single array (e.g., 32-by-32 rectangular array) with a small form factor. According to IMT-2020 [30], the 5G base station can have up to 256 antenna elements for 30 GHz operating frequency and 1024 antenna elements for 70 GHz operating frequency.

## 2.8 Advanced Antenna System Design

### 2.8.1 *Design an Antenna Array*

An antenna array (or phased array) is a set of two or more connected antenna elements which work together as a single antenna to transmit or receive radio waves, shown in Figure 2.13 [31, 32]. Typically, the single element antenna provides a relatively wide radiation pattern with low gain (directivity). But, the radiation pattern of an antenna array is able to provide a narrower beam and can achieve higher gain (or directivity) as required for long-distance communications [31].

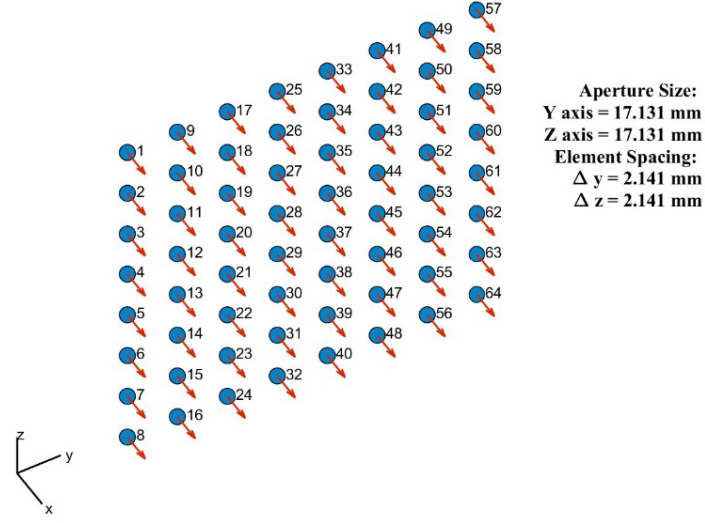


Figure. 2.13 An 8-by-8 uniform rectangular phased array antenna architecture for 70 GHz operating frequency

This dissertation uses the base station antenna characteristics defined by the ITU-R report for 70GHz operating frequency, shown in Table 2.1[30]. Figure 2.14 shows the 3D radiation pattern of a base station (i.e., cell site) with a single antenna element and an array with 8-by-8 antenna elements for 70 GHz operating frequency.

Table. 2.1 Characteristics of the antenna radiation pattern for a 5G cell. [30]

Parameters	Values
Antenna element vertical radiation pattern (dB)	$A_{E,V}(\theta'') = -\min\left[12\left(\frac{\theta'' - 90^0}{\theta_{3dB}}\right)^2, SLA_V\right], \theta_{3dB} = 65^0, SLA_V = 30$
Antenna element horizontal radiation pattern (dB)	$A_{E,H}(\phi'') = -\min\left[12\left(\frac{\phi''}{\phi_{3dB}}\right)^2, A_m\right], \phi_{3dB} = 65^0, A_m = 30$
Combining method for 3D antenna element pattern (dB)	$A''(\theta'', \phi'') = -\min\{-[A_{E,V}(\theta'') + A_{E,H}(\phi'')], A_m\}$

Maximum directional gain of an antenna element $G_{E,max}$	8 dBi
---	-------

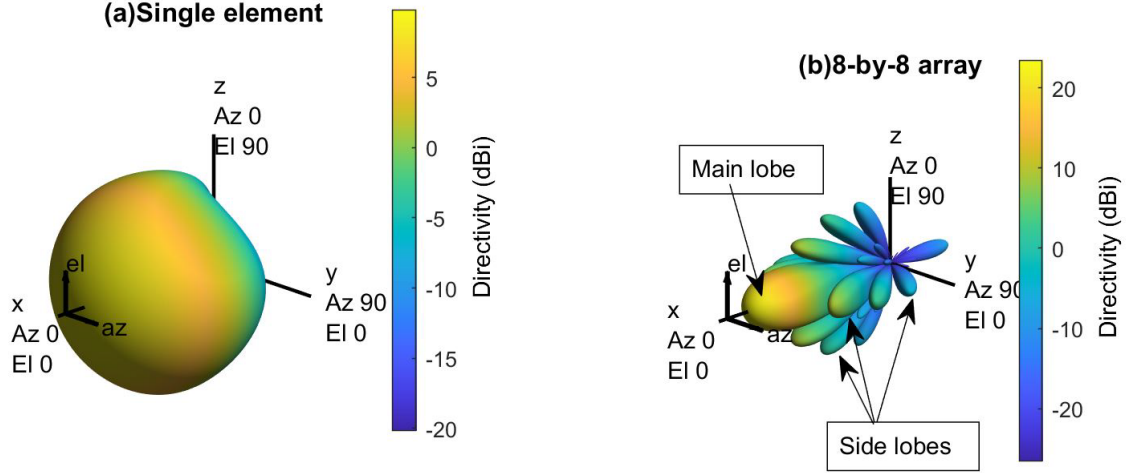


Figure. 2.14 Simulated 3D radiation pattern of a single rectangular patch antenna element and an 8-by-8 array comprised of rectangular patch antenna elements

It is not necessary, but it is often convenient and more practical to use identical elements in the array. The radiation pattern of such an antenna array depends on the following factors [31]:

1. The geometrical configuration (e.g., linear, circular, rectangular, etc.) of the array
2. The relative spacing between the elements
3. The radiation pattern of each element
4. The excitation phase and amplitude of the individual elements

This dissertation considers a uniform rectangular phased array that uses identical elements and uniform spacing between elements. Since the array antenna provides path diversity, also called Multiple-Input Multiple-Output (MIMO), the path diversity increases with the sizes of the array (i.e., number of elements in the array) [31]. The 5G networks

will use the larger antenna array ( $\sim 1024$  antenna elements) on the transmitter (i.e., cell-site) and receiver (i.e., mobile phone) to take advantage of the massive MIMO, which will increase the network reliability [33, 34].

The phased array antenna also allows changing the phase of each element electronically, which can be used to steer the beam in the desired direction to avoid interference from a specific direction [32]. This dissertation shows that the Signal-to-Interference-Plus-Noise-Ratio (SINR) of 5G networks can also be improved by using the larger array for individual cell-site transmitters.

### **2.8.2** *Antenna Array with Reduced Side Lobes*

The vector addition of the radio waves radiated by the individual antenna elements determines the array's radiation pattern. The radiated waves of each individual element interfere constructively in one direction that produces a strong beam in one direction called the main lobe, shown in Figure 2.14 (b). But, all the radiated waves interfering destructively are canceling out, reducing the powers radiated in other directions. However, the uniform array (i.e., arrays with uniform spacing between elements) will have a series of weaker radiated beams at different angles than the main lobe. These are called sidelobes [31, 32, 35], and they are undesirable in most array applications (shown in Figure 2.14).

Figure 2.15 shows the 3D radiation pattern of an 8-by-8 uniform phased array with different antenna element spacing (i.e.,  $\frac{1}{4}$  wavelength,  $\frac{1}{2}$  wavelength, and one wavelength) for 70GHz operating frequency. The main lobe becomes more directive (high gain) as the element spacing increases. But the number of sidelobes and sidelobes power increases. It must be reduced to direct the maximum power towards the main lobe.

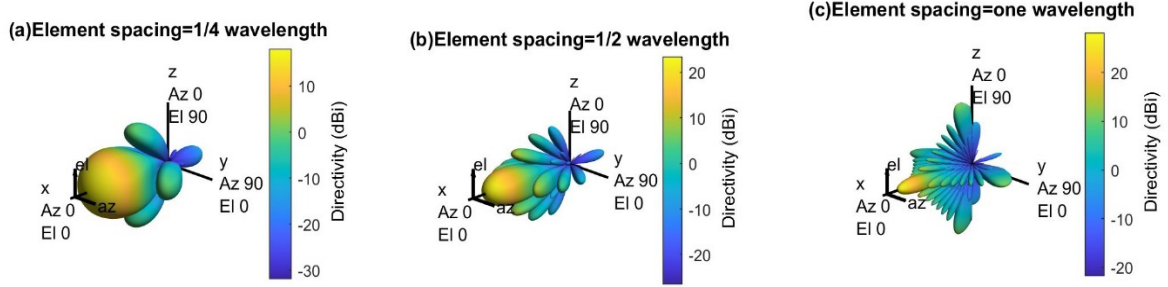


Figure. 2.15 3D radiation pattern of an 8-by-8 antenna array composed of rectangular patch antenna elements, with varying element spacing: (a) element spacing of  $\frac{1}{4}$  wavelength, (b) element spacing of  $\frac{1}{2}$  wavelength, and (c) element spacing of one wavelength.

Figure 2.16 represents the 3D radiation pattern of a single transmitter with different array antenna sizes (e.g., 8-by-8 array and 16-by-16 array) for 70 GHz operating frequency. The antenna radiation becomes more directive (i.e., high gain) as the number of elements in the antenna array increases. Since the directional gain increases with the size of the antenna array, it will also increase the peak SINR (signal-to-interference-plus-noise ratio). Eventually, it will improve the overall network performance.

However, the number of sidelobes and the sidelobes power increases if we increase the number of antenna elements per array, shown in Figure 2.16 (b) and Figure 2.16 (c), respectively. These sidelobes power must be reduced before implementing this transmitter with any base stations.

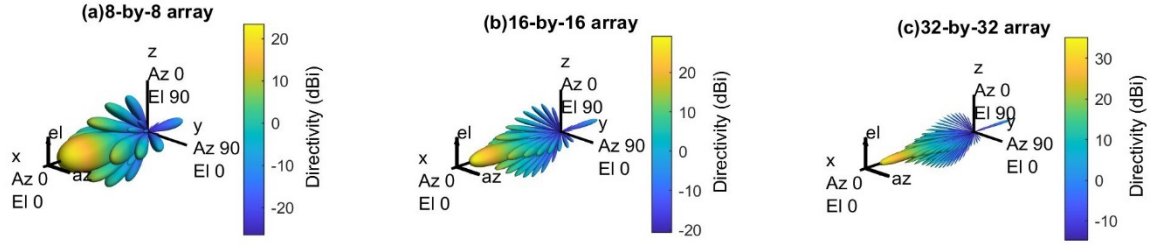


Figure. 2.16 3D radiation pattern of a rectangular patch antenna array without amplitude tapering, with various array sizes: (a) an 8-by-8 array, (b) a 16-by-16 array, and (c) a 32-by-32 array

There are several methods of amplitude tapering (e.g., Dolph-Chebyshev, Taylor, and Binomial) to reduce the sidelobes power, where the array elements are tapered maximum at the center and minimum at the edges [36, 37]. But, this dissertation uses the Dolph-Chebyshev amplitude tapering method to reduce the side lobe's power discussed in this section.

Figure 2.16 shows that the largest sidelobes are closer to the main lobe and the smallest sidelobes are far away from the main lobe. To achieve a minimum sidelobe power of  $R$  dB (e.g., 30 dB), a window can be designed where the sidelobes closer to the main lobe will be attenuated by  $R$  dB (e.g., 30 dB); the sidelobes far away from the main lobe will be attenuated higher than  $R$  dB. This optimum window is known as the Dolph-Chebyshev window, and it is constructed with the Chebyshev polynomials [31, 32]. The  $m^{\text{th}}$  Chebyshev polynomial can be calculated by the following Equation 2.11 [32]:

$$T_m(X) = \cos(m \arccos(x)) \quad (2.11)$$

If  $|x| > 1$ , the value of  $\arccos(x)$  will be imaginary. Therefore, the Equation (2.11) can be written in terms of hyperbolic cosines:  $T_m(X) = \cosh(m \operatorname{acosh}(x))$ .

By setting  $x = \cos \theta$ , or  $\theta = \arccos(x)$ ,  $T_m(x) = \cos(m\theta)$ . Now, the  $\cos(m\theta)$  can be expanded as a polynomial in powers of  $\cos\theta$ , where the expansion coefficients are the Chebyshev polynomial, shown below:

$\cos(0\theta) = 1$	$T_0(x) = 1$
$\cos(1\theta) = \cos \theta$	$T_1(x) = x$
$\cos(2\theta) = 2 \cos^2 \theta - 1$	$T_2(x) = 2x^2 - 1$
$\cos(3\theta) = 4 \cos^3 \theta - 3 \cos \theta$	$T_3(x) = 4x^3 - 3x$
$\cos(4\theta) = 8 \cos^4 \theta - 8 \cos^2 \theta + 1$	$T_4(x) = 8x^4 - 8x^2 + 1$

The Chebyshev polynomial has equal ripples when  $|x| < 1$ , but it increases like  $x^m$  when  $|x| > 1$ .

### 2.8.3 Antenna Array Analysis with Amplitude Tapering

This section shows the following effects of Dolph-Chebyshev amplitude tapering with the 8-by-8, 16-by-16 array, and 32-by-32 array antenna:

- Sidelobes power
- Beamwidth
- Directivity

#### a) Effect on Sidelobes Power

Figure 2.17 shows the 3D radiation pattern of the uniform phased array antenna (i.e., 8-by-8, 16-by-16 array, and 32-by-32 array) with Dolph-Chebyshev amplitude tapering. In this simulation, 30 dB amplitude tapering is applied to reduce the sidelobes power. It is found that the amplitude tapering reduces the sidelobes power significantly for all arrays.

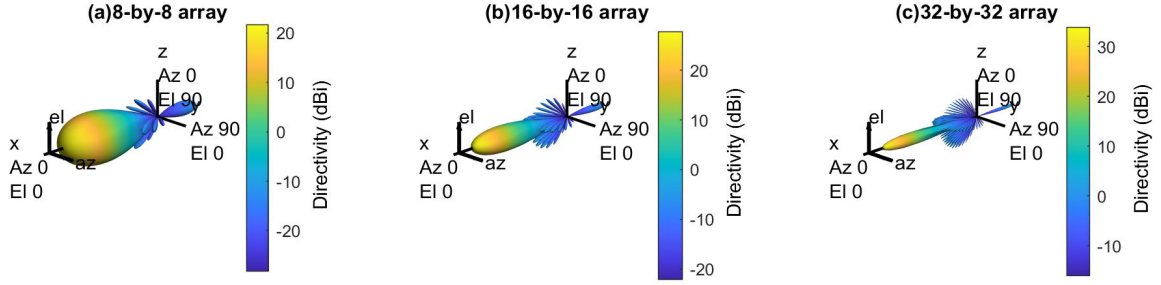


Figure. 2.17 3D radiation pattern of a rectangular patch antenna array with amplitude tapering, varying in size: (a) an 8-by-8 array, (b) a 16-by-16 array, and (c) a 32-by-32 array

To understand the effect of sidelobes power after amplitude tapering, Figure 2.18 shows the normalized power distribution of the array (i.e., 8-by-8, 16-by-16, and 32-by-32 array) with and without the Dolph-Chebyshev amplitude tapering. It is found that the sidelobes' power closer to the main lobe reduced by 30 dB and the other sidelobes far away from the main lobe reduced more than 30 dB as expected. However, the main lobe beamwidth gets a little wider for all arrays after the amplitude tapering. It will reduce the antenna directivity (i.e., gain) for all arrays shown in part (d).



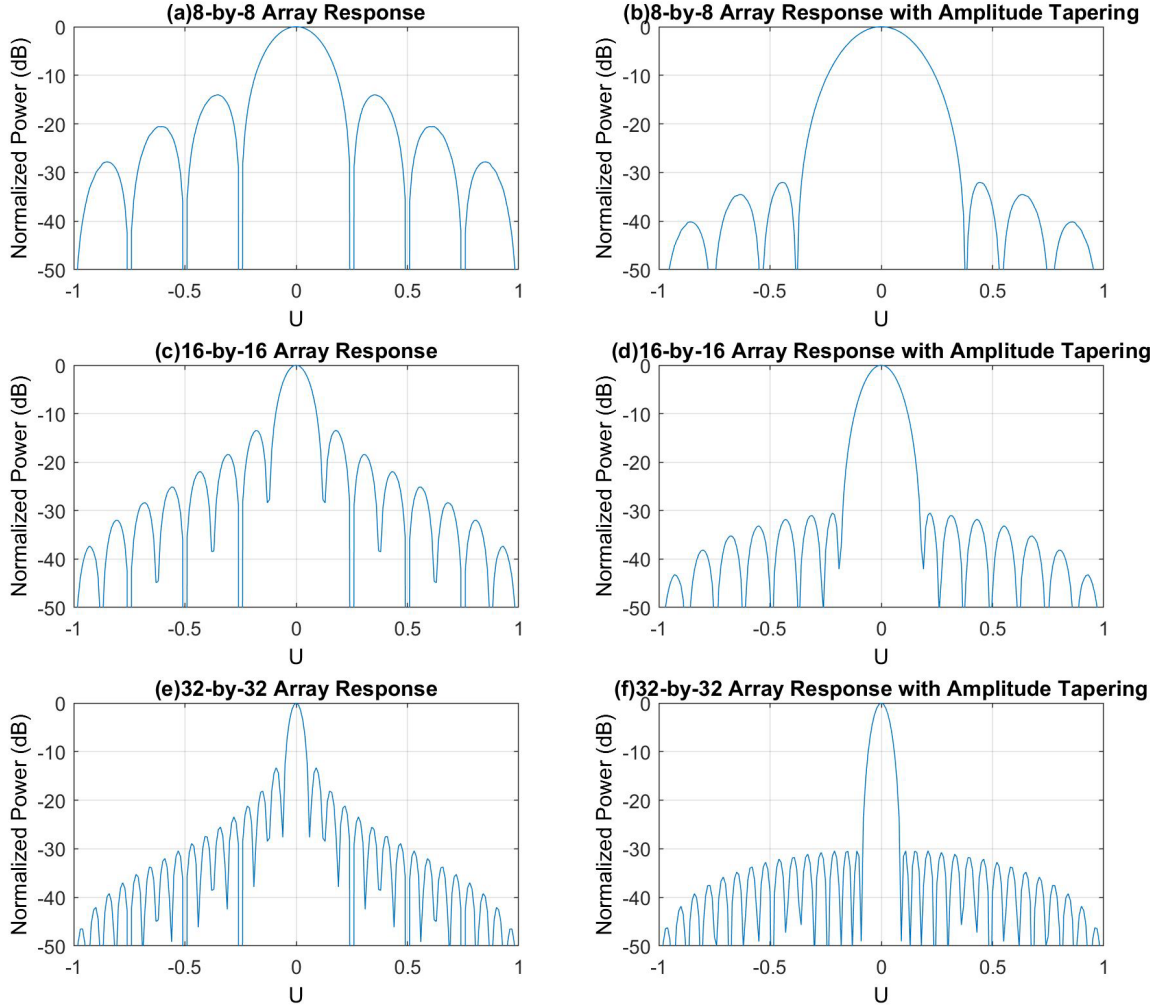


Figure. 2.18 Normalized power distribution of various arrays, with and without 30dB amplitude tapering: (a) the response of an 8-by-8 array, (b) the response of an 8-by-8 array with amplitude tapering, (c) the response of a 16-by-16 array, (d) the response of a 16-by-16 array with amplitude tapering, (e) the response of a 32-by-32 array, and (f) the response of a 32-by-32 array with amplitude tapering

#### b) Effect on Beamwidth

In the antenna radiation pattern, the main lobe is the antenna's main beam, where maximum energy is radiated by the antenna. The angular separation between the half power

point (or -3dB) of the main lobe is called the Half Power Beam Width (HPBW), shown in Figure 2.19 [31]. The beamwidth or HPBW has an inverse relation with the antenna gain and directivity. For example, if beamwidth increases, the antenna directivity will decrease.

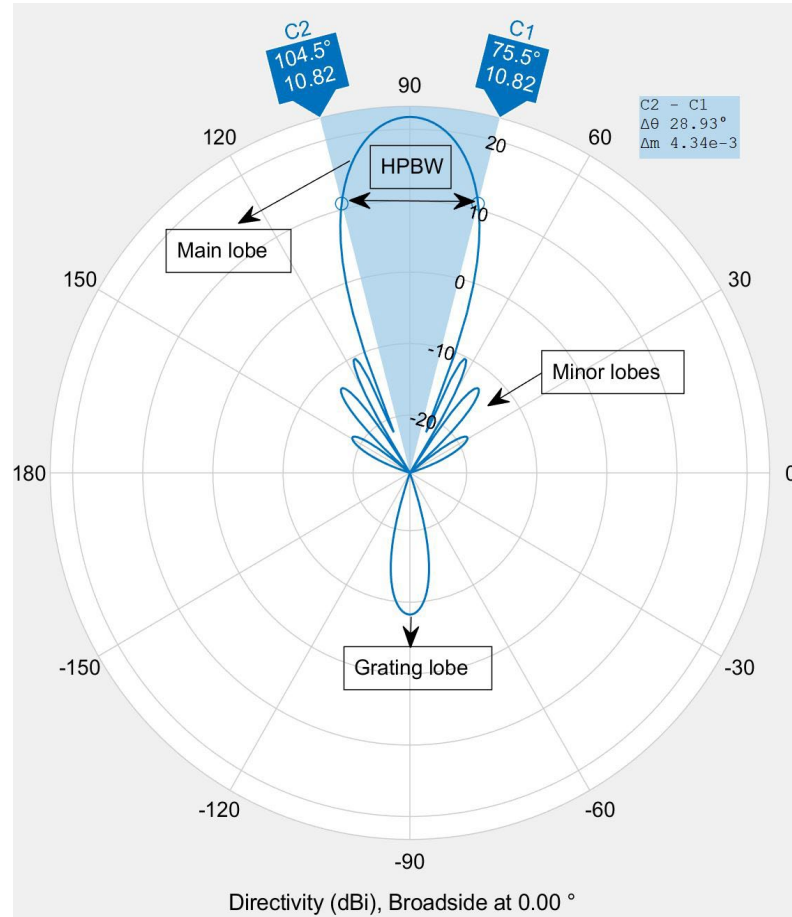


Figure. 2.19 An illustration of the radiation pattern of an 8-by-8 antenna array, which displays the half power beam width, main lobe, minor lobes, and grading lobe.

The amplitude tapering greatly impacts all arrays' beamwidth (i.e., 8-by-8, 16-by-16 array, and 32-by-32 array), shown in Figure 2.18. It is found that the beamwidth of the 8-by-8 array increases by  $7.9558^\circ$ , the 16-by-16 array increases by  $3.9116^\circ$ , and the 32-by-32 array increases by  $0.7558^\circ$ , respectively. Since the beamwidth increase after the amplitude, tapering will reduce the maximum directivity for all arrays, shown in part (d).

It is clear that the lower size array (i.e., 8-by-8 array) will be impacted significantly by amplitude tapering compared to the larger size array (i.e., 32-by-32 Array). Therefore, the system designer must maximize the size of the array for better beamwidth and maximum directivity.

However, the beamwidth of the antenna array also depends on the level (e.g., 30 dB or 50 dB) of amplitude tapering. Figure 2.20 shows the normalized power distribution of the array (i.e., 8-by-8, 16-by-16, and 32-by-32 array) with 30 dB and 50 dB Dolph-Chebychev amplitude tapering. It is found that the beamwidth increases for all arrays if we increase the amplitude tapering level from 30 dB to 50 dB, listed in Table 2.2. The beamwidth of the 8-by-8 array antenna is impacted significantly, and it increases by  $11.9337^0$  with 50 dB amplitude tapering compared to  $7.95580$  with 30 dB amplitude tapering.

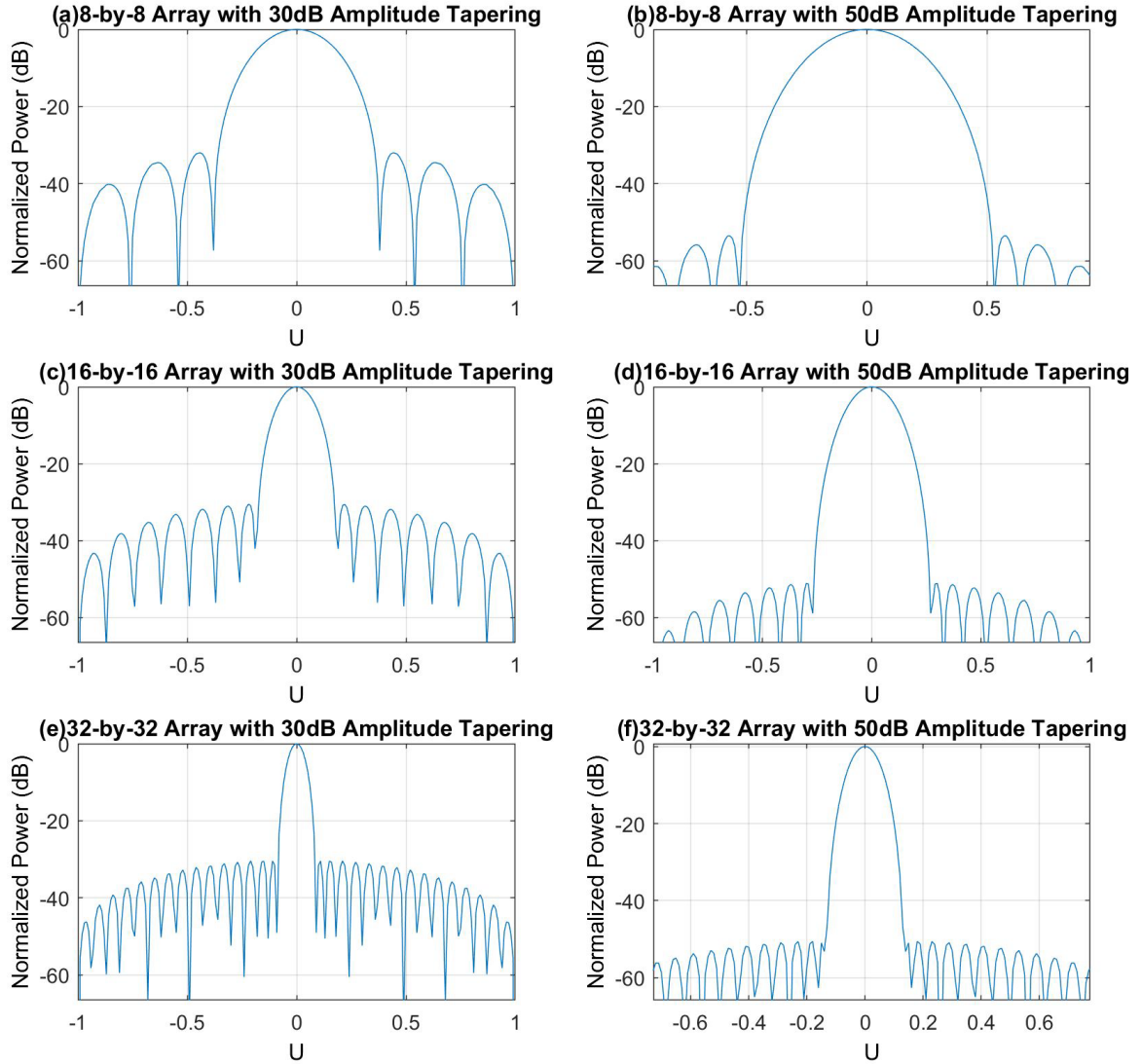


Figure. 2.20 Comparison of the normalized power distribution of various arrays with 30dB and 50dB amplitude tapering in contrast to Figure 2.18: (a) the response of an 8-by-8 array with 30dB amplitude tapering, (b) the response of an 8-by-8 array with 50dB amplitude tapering, (c) the response of a 16-by-16 array with 30dB amplitude tapering, (d) the response of a 16-by-16 array with 50dB amplitude tapering, (e) the response of a 32-by-32 array with 30dB amplitude tapering, and (f) the response of a 32-by-32 array with 50dB amplitude tapering.

Table. 2.2 Half power beam width of uniform phased array antenna with various level of amplitude tapering.

Antenna array size	HPBW with 0dB Amplitude tapering	HPBW with 30dB Amplitude tapering	HPBW with 50dB Amplitude tapering
8-by-8 Array Antenna	27.8453 <sup>0</sup>	35.8011 <sup>0</sup>	39.7790 <sup>0</sup>
16-by-16 Array Antenna	12.0 <sup>0</sup>	15.9116 <sup>0</sup>	19.8895 <sup>0</sup>
32-by-32 Array Antenna	7.2 <sup>0</sup>	7.9558 <sup>0</sup>	11.9337 <sup>0</sup>

Since the beamwidth increases with increasing amplitude tapering, the maximum directivity will also reduce significantly, shown in part (d). Therefore, the system designer must find an optimum amplitude tapering value level that minimizes the side lobes power but provides better beamwidth and maximum directivity. This dissertation uses 30 dB amplitude tapering for the uniform phased array.

#### c) Effect on Directivity

The results presented in Figure 2.20 show that amplitude tapering significantly reduces the sidelobe power for all arrays. However, as shown in Table 2.2, the half power beamwidth increases with varying levels of amplitude tapering. This causes a decrease in the antenna directivity for all arrays, as shown in Table 2.3. The 8-by-8 uniform phased array experiences a directivity loss of 1.73 dBi, the 16-by-16 array experiences a loss of 1.43 dBi, and the 32-by-32 array experiences a loss of 1.2 dBi after amplitude tapering.

The largest size array, the 32-by-32 array, achieves the maximum directivity of 33.97 dBi. Therefore, it is recommended that system designers use the maximum size array for each transmitter to achieve optimal results.

In addition, the directivity of the antenna array also depends on the level (e.g., 30 dB or 50 dB) of amplitude tapering, listed in Table 2.3. It is found that the directivity decreases for all arrays if we increase the amplitude tapering from 30 dB to 50 dB. For example, the directivity of an 8-by-8 array antenna reduces by 1.73 dBi for 30 dB amplitude tapering and 3.17 dBi for 50 dB amplitude tapering. Therefore, the system designer must find an optimum amplitude tapering level that reduces the side lobes power but provides better beamwidth and maximum directivity.

Table. 2.3 Maximum directivity of the array antenna with different levels of amplitude tapering.

Tapering Level	8-by-8 Array Maximum Directivity	16-by-16 Array Maximum Directivity	32-by-32 array Maximum Directivity
0 dB	23.45 dBi	29.25 dBi	35.17 dBi
30 dB	21.72 dBi	27.82 dBi	33.97 dBi
50 dB	20.28 dBi	25.95 dBi	32.01 dBi

In summary, the amplitude tapering significantly reduces sidelobes power and directs the maximum power towards the main lobe regardless of small directivity loss for all arrays (i.e., 8-by-8, 16-by-16, and 32-by-32 array). Therefore, it will reduce interferences (i.e., out-of-cell or intercell interference) and improve network performance.

## 2.9 Propagation modeling

The radiated energy of the transmitter spreads over the surface of a sphere as it propagates from the transmitter to the receiver and the total signal attenuation depends on a variety of factors. Some key factors are listed below [11, 38]:

- Operating frequency (e.g., 30 GHz, 70 GHz, etc.)
- Distance between transmitter and receiver
- Cell site location (i.e., indoor or outdoor)
- Propagation environment (e.g., rural, urban, dense urban, etc.)
- Actual terrain (e.g., open, forest, sea, etc.)
- Atmospheric conditions (e.g., rainfall, fog, and clouds, etc.)
- Antenna height (e.g., transmitter height and receiver height)

A propagation model is a mathematical equation that describes the behavior of the signal as it propagates from the transmitter to the receiver in a communication link. Such a model can be used to estimate the maximum path loss from the transmitter to the receiver and thus provide an estimate of the maximum cell range [11, 38]. The Friis transmission formula is used to calculate received signal power under ideal conditions for a transmitter and a receiver separated by a specific distance [39]. However, additional losses are experienced in any wireless communication links, which can be integrated into Friis transmission formula, as demonstrated in the Equation (2.12):

$$P_{RX} = \frac{P_{TX} G_{TX} G_{RX}}{L_{TX} L_{RX} L_{Pol} L_{FS} L_R L_C L_G L_M} \quad (2.12)$$

Where  $P_{RX}$  is the received signal power, expressed in dBm, while  $P_{TX}$  signifies the transmit signal power, also expressed in dBm. The receiver and transmitter antenna gains are

represented by  $G_{RX}$  and  $G_{TX}$ , respectively; both are expressed in dBi units.  $L_{TX}$  and  $L_{RX}$  (in dB) account for losses associated with the transmitter and receiver antennas, including factors like cable loss, feeder, and connector loss. Additionally,  $L_{Pol}$  quantifies losses attributed to polarization mismatch and expressed in dB. Moreover,  $L_{FS}$  characterizes free space path loss,  $L_r$  pertains to path loss due to rain,  $L_c$  accounts for path loss due to cloud or fog, and  $L_g$  represents the path loss due to gaseous atmospheric; all are expressed in dB. All other types of losses (e.g., fading margin, body loss, etc) are represented by the single parameter  $L_M$ , expressed in dB. This section provides an overview of propagation modeling basics for the 5G network.

### **2.9.1 Free Space Propagation Modelling**

In optimal propagation conditions, the signal travels through free space with a clear line of sight between the transmitter and receiver, without any barriers that could absorb or reflect the signal. In this scenario, the energy radiated from the transmitter spreads over a sphere centered on the transmitting antenna, and only a portion of this energy is captured by the receiving antenna. The energy that is not captured by the receiving antenna is treated as a loss term in the propagation model. This type of signal attenuation is called ‘free-space path loss’ and is determined as shown in Equation (1.2). Figure 2.21 illustrates the total free space path loss for various operating frequencies, which increases as the frequency increases. Furthermore, if the signal must travel a greater distance, the total attenuation also increases according to that distance squared. For instance, if we extend the cell range for a 70GHz frequency from 100m to 600m, the propagation loss will increase by 15.6dB. Therefore, 5G networks restrict the cell range to a few hundred meters to ensure strong



signal strength throughout the deployment area instead of several kilometers for the 4G networks.

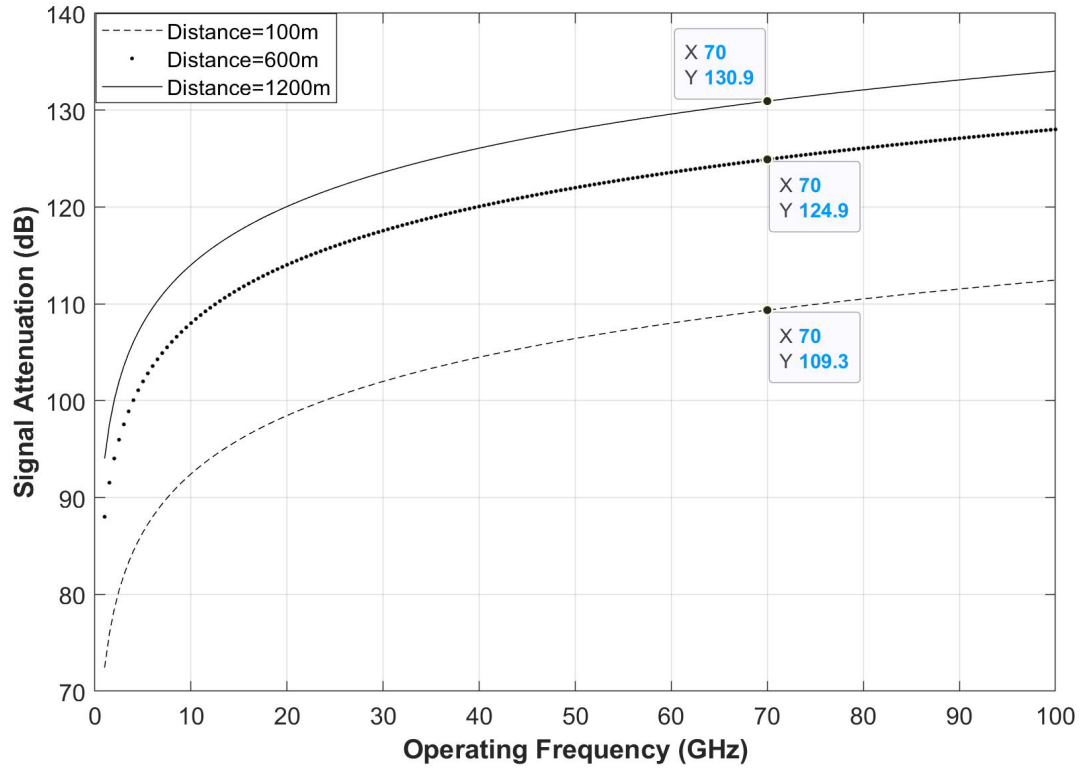


Figure. 2.21 RF signal attenuation in free space as a function of operating frequency obtained using Equation (1.2) for cell ranges of 100m, 600m, and 1200m.

### 2.9.2 RF Signal Attenuation Due to Rainfall

RF signals experience attenuation when propagation occurs in the presence of rainfall. The total RF signal attenuation due to rainfall can be calculated by ITU rainfall model Recommendation ITU-R P.838-3, shown in Equation (2.13) [40]. This specific attenuation model is valid for frequencies from 1–1000 GHz.

$$L_r = d_{\text{eff}} k R^\alpha \quad (2.13)$$

Where  $R$  is the rain rate in mm/hr. The parameter  $k$  and  $\alpha$  are determined experimentally and depend on frequency, polarization state, and elevation angle of the signal path, as shown in Table 5 of reference [40]. The parameter  $d_{\text{eff}}$  is the effective propagation distance and is equal to the geometric distance,  $d$ , multiplied by a scaling factor,  $r$ , that is given by Equation (2.14) [40, 41]. In this equation, the parameter  $f$  represents the operating frequency.

$$r = \frac{1}{0.477d^{0.633}R_{0.01}^{0.073\alpha}f^{0.123} - 10.579(1 - \exp(-0.024d))} \quad (2.14)$$

Figure 2.22 shows the total RF signal attenuation due to rainfall versus operating frequency for propagation path length of 100m and differing rainfall rates of 1mm/hr, 6mm/hr, 20mm/hr, 50mm/hr, and 100mm/hr. Here we see that the signal attenuation increases with increasing the operating frequency. The signal attenuation also increases if the rainfall increases from light rain (i.e., rainfall=1 mm/hr) to heavy rain (i.e., rainfall=50 mm/hr). However, the total attenuation due to rainfall remains relatively low for all millimeter-wave frequencies. For example, for an operating frequency of 70 GHz operating in violent rainfall (i.e., rainfall = 100mm/hr) scenario, the signal experience attenuation of approximately 7.592dB. This amount of loss can be easily overcome through increased transmit power. This idea is discussed in greater detail in section 2.9.9.

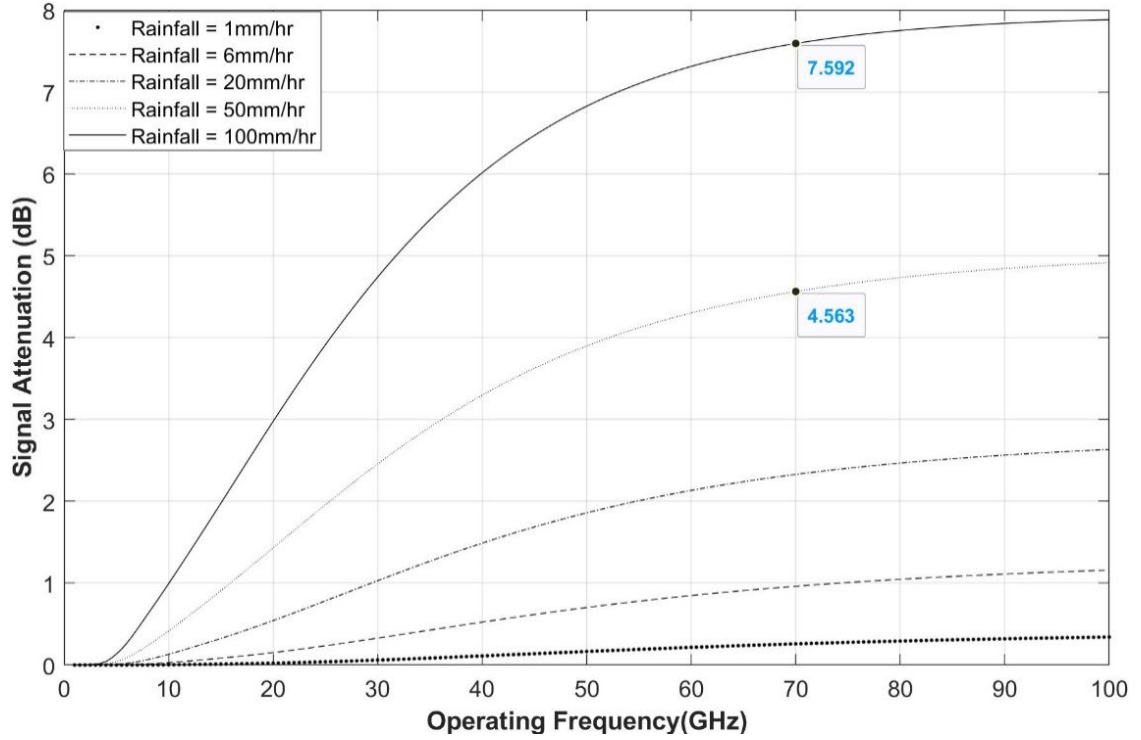


Figure. 2.22 RF signal attenuation at various operating frequencies for a 100m propagation path obtained using Equation (2.13) for the rainfall rates of 1 mm/hr, 6 mm/hr, 20 mm/hr, 50 mm/hr, and 100 mm/hr

RF signal attenuation due to rainfall greatly depends on the propagation path length, shown in Figure 2.23. Total signal attenuation due to rainfall increases significantly if the path length increases from 100m to 300m or 1000m. However, if we limit the 5G cell site radius to 100 m, the total signal attenuation can be below 8 dB for the heavy rainfall. Therefore, the system designer must use the average rainfall rate for any deployment area to estimate the signal loss in the worst-case scenario (i.e., heavy/violent rainfall).

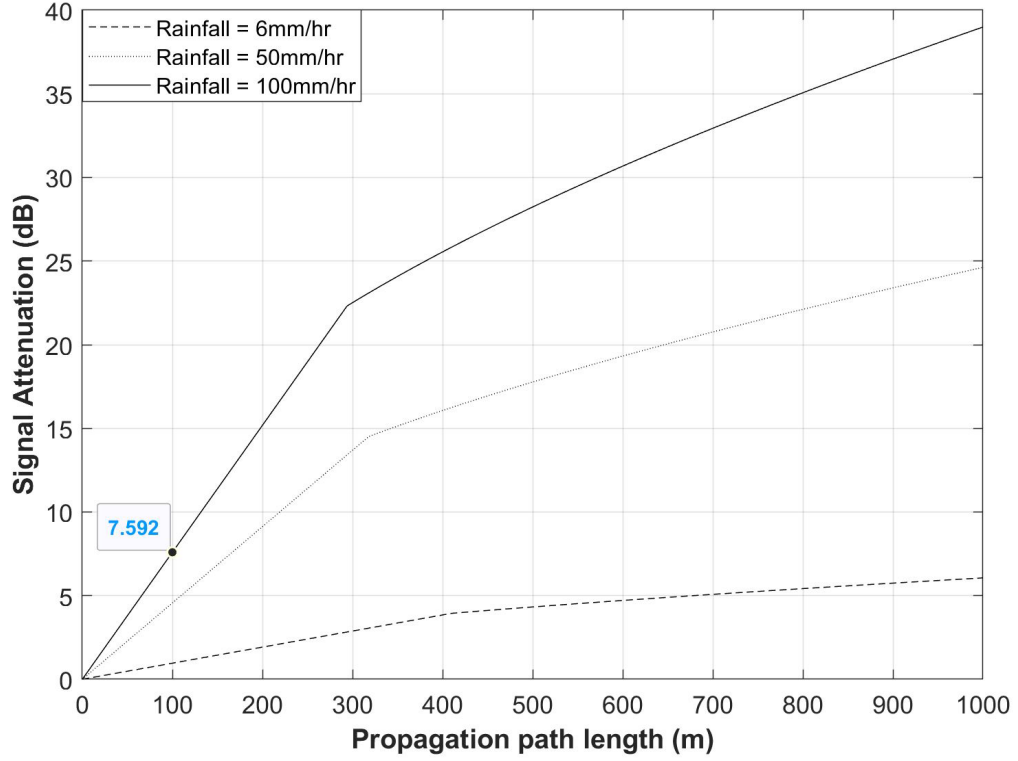


Figure. 2.23 RF signal attenuation over distance for 70 GHz operating frequency obtained using Equation (2.13) for the rainfall rates of 6 mm/hr, 50 mm/hr, and 100 mm/hr

### 2.9.3 RF Signal Attenuation Due to Fog and Clouds

Fog and clouds represent the same atmospheric phenomenon, differentiated only by height above the ground. Both effects induce attenuation in propagating RF signals. The total signal attenuation can be calculated by the ITU model (Recommendation ITU-R P.840-6), shown in Equation (2.15) [25].

$$L_c = K_l(f) M R \quad (2.15)$$

Where  $M$  is the liquid water density in  $\text{gm/m}^3$ , and  $R$  represents the propagation path length. The quantity  $K_l(f)$  is the specific attenuation coefficient and depends on the operating frequency. This attenuation model is valid for frequencies in the range 10-

100GHz and can be used to account for the effects of both fog and clouds, depending on the height above the ground [25].

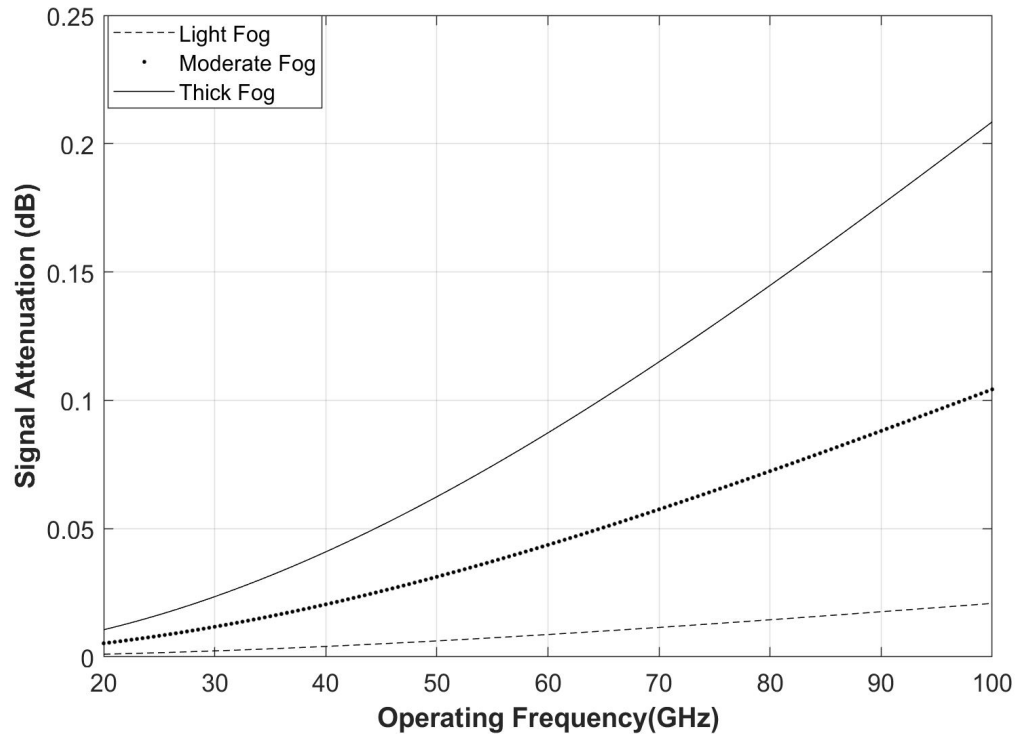


Figure. 2.24 RF signal attenuation at different operating frequencies obtained using Equation (2.15) for light fog, moderate fog, and thick fog

Figure 2.24 shows the total signal attenuation due to various densities of fog (i.e., light fog to thick fog) for a 100m propagation path at different operating frequencies. It is found that the signal attenuation increases with the operating frequency and the fog densities (i.e., liquid water density is  $0.05\text{g/m}^3$  for light fog and  $0.5\text{ g/m}^3$  for thick fog). However, the total signal attenuation is lower than 0.25 dB even in the dense fog scenario and at an operating frequency of 70 GHz because of the relatively short propagation path length (i.e., cell radius is 100m).

#### 2.9.4 RF Signal Attenuation Due to Atmospheric Gas

Even in clear skies with no wind and not rain, fog, or other effects already discussed, RF signals experience attenuation in the atmosphere due to a variety of small particles that are present. This phenomena is primarily due to adsorption by water vapor, molecules of oxygen, and other gaseous atmospheric constituents [42]. Total RF signal attenuation due to the combination of oxygen and water vapor can be estimated by the International Telecommunication Union (ITU) atmospheric gas attenuation model ITU-R P.676-13 [43, 44]; this attenuation model is valid for operating frequencies from 1-1000 GHz. The total RF signal attenuation due to these gaseous constituents is given by Equation (2.16) [44].

$$\gamma = \gamma_o + \gamma_w = 0.1820 f \left( N''_{Oxygen}(f) + N''_{WaterVapor}(f) \right) \quad \text{dB/km} \quad (2.16)$$

Where  $\gamma_o$  is the specific attenuation (dB/km) due to dry air (oxygen, pressure-induced nitrogen attenuation above 100 GHz, and non-resonant Debye attenuation of oxygen below 10GHz), and  $\gamma_w$  is the specific attenuation (dB/km) due to water vapor. The operating frequency is represented by  $f$  (GHz). Additionally,  $N''_{Oxygen}(f)$  and  $N''_{WaterVapour}(f)$  represents the imaginary components of the frequency-dependent complex refractivities computed using Equation (2.17) and (2.18), respectively.

$$N''_{Oxygen}(f) = \sum_{i(Oxygen)} S_i F_i + N''_D(f) \quad (2.17)$$

$$N''_{WaterVapor}(f) = \sum_{i(WaterVapor)} S_i F_i \quad (2.18)$$

Where  $S_i$  stands for the line strength of oxygen or water vapor, and  $F_i$  represents the line shape factor for oxygen or water vapor, as defined in Equation (2.19) and (2.21).

Furthermore,  $N_D''(f)$  represents the dry continuum resulting from pressure-induced nitrogen absorption and the Debye spectrum as described by Equation (2.19).

$$\begin{aligned} S_i &= a_1 \times 10^{-7} \left(\frac{300}{T}\right)^3 \exp\left[a_2\left(1 - \left(\frac{300}{T}\right)\right)\right] P && \text{(for oxygen)} \\ &= b_1 \times 10^{-1} \left(\frac{300}{T}\right)^{3.5} \exp\left[b_2\left(1 - \left(\frac{300}{T}\right)\right)\right] W && \text{(for water vapor)} \end{aligned} \quad (2.19)$$

Where T is the operating temperature (kelvin), and P is the dry air pressure (hPa). The oxygen and water vapor dependent parameters (e.g.,  $a_1$ ,  $a_2$ ,  $b_1$ , and  $b_2$ ) as functions of frequency is listed in Table 1 and Table 2 of ITU model ITU-R P.676-13 [44]. Moreover, W is related to the water vapor density ( $\rho$ ) given by Equation (2.20):

$$W = \frac{\rho T}{216.7} \quad (2.20)$$

The line shape factor is given by:

$$F_i = \frac{f}{f_i} \left[ \frac{\Delta f - \delta (f_i - f)}{(f_i - f)^2 + \Delta f^2} + \frac{\Delta f - \delta (f_i + f)}{(f_i + f)^2 + \Delta f^2} \right] \quad (2.21)$$

Where  $f_i$  is the oxygen or water vapor line frequency. The width of the line is represented by  $\Delta f$  and computed by Equation (2.22).

$$\begin{aligned} \Delta f &= a_3 \times 10^{-4} \left( p \left(\frac{300}{T}\right)^{(0.8-a_4)} + 1.1 W \left(\frac{300}{T}\right) \right) && \text{(for oxygen)} \\ &= b_3 \times 10^{-4} \left( p \left(\frac{300}{T}\right)^{b_4} + b_5 W \left(\frac{300}{T}\right)^{b_6} \right) && \text{for water vapor} \end{aligned} \quad (2.22)$$

$\delta$  is a correction factor that arises due to interference effects in oxygen lines and calculated by Equation (2.23):

$$\delta = (a_5 + a_6(\frac{300}{T})) \times 10^{-4}(p + e)(\frac{300}{T})^{0.8} \quad (\text{for oxygen}) \quad (2.23)$$

$$= 0 \quad (\text{for water vapor})$$

The dry air continuum results from the non-resonant Debye spectrum of oxygen below 10 GHz and pressure-induced nitrogen attenuation above 100 GHz given by Equation (2.24):

$$N_D''(f) = f p \left(\frac{300}{T}\right)^2 \left[ \frac{6.14 \times 10^{-5}}{d \left[1 + \left(\frac{f}{d}\right)^2\right]} + \frac{1.4 \times 10^{-12} p \left(\frac{300}{T}\right)^{1.5}}{1 + 1.9 \times 10^{-5} f^{1.5}} \right] \quad (2.24)$$

Where d is the width parameter for the Debye spectrum as described in Equation (2.25):

$$d = 5.6 \times 10^{-4}(p + e)(\frac{300}{T})^{0.8} \quad (2.25)$$

Figure 2.25 shows the RF signal attenuation due to gaseous atmospheric constituents as a function of frequency. In the simulation, the propagation path length is considered as 100 m (i.e., 5G cell-site range) and the atmospheric pressure is 101300.0 Pa. This figure shows several prominent attenuation peaks that occur at specific frequencies, coinciding with the resonant frequencies of the individual gaseous molecules contained in the atmosphere. Total attenuation due to gaseous constituents increases as humidity increases. For example, the water vapor density for dry air is 0 g/m<sup>3</sup>, where the signal attenuation is lowest for all frequencies. Still, attenuation increases significantly with increasing water vapor density (e.g., 30 g/m<sup>3</sup>).



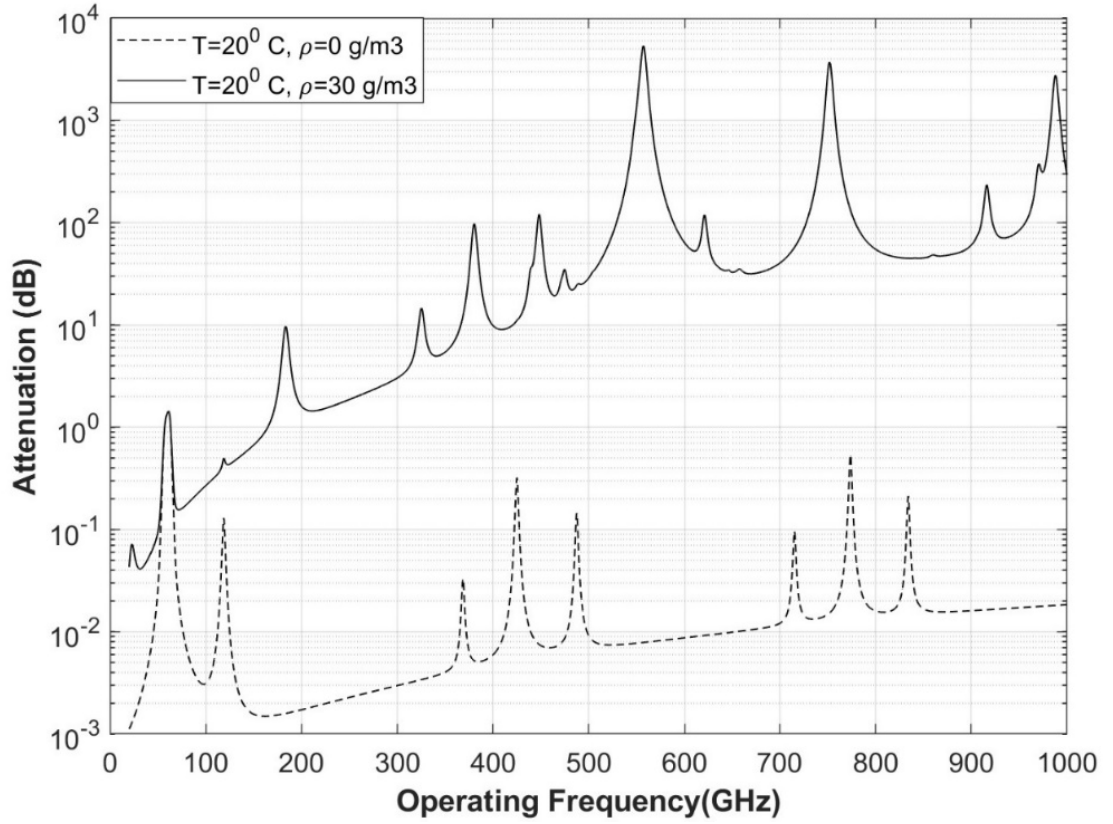


Figure. 2.25 RF signal attenuation at different operating frequencies with a 100m cell radius obtained using Equations (2.16) and (2.17) for the water vapor density of  $0\text{ g/m}^3$  (i.e., dry air) and  $30\text{ g/m}^3$  (i.e., humid air)

Gaseous atmospheric attenuation also significantly varies with propagation path length. Figure 2.26 shows the gaseous atmospheric attenuation over propagation path length for 70 GHz operating frequency. It shows that the total attenuation will not be significant (i.e., below 0.2 dB) if we limit the 5G cell site radius to 100m.

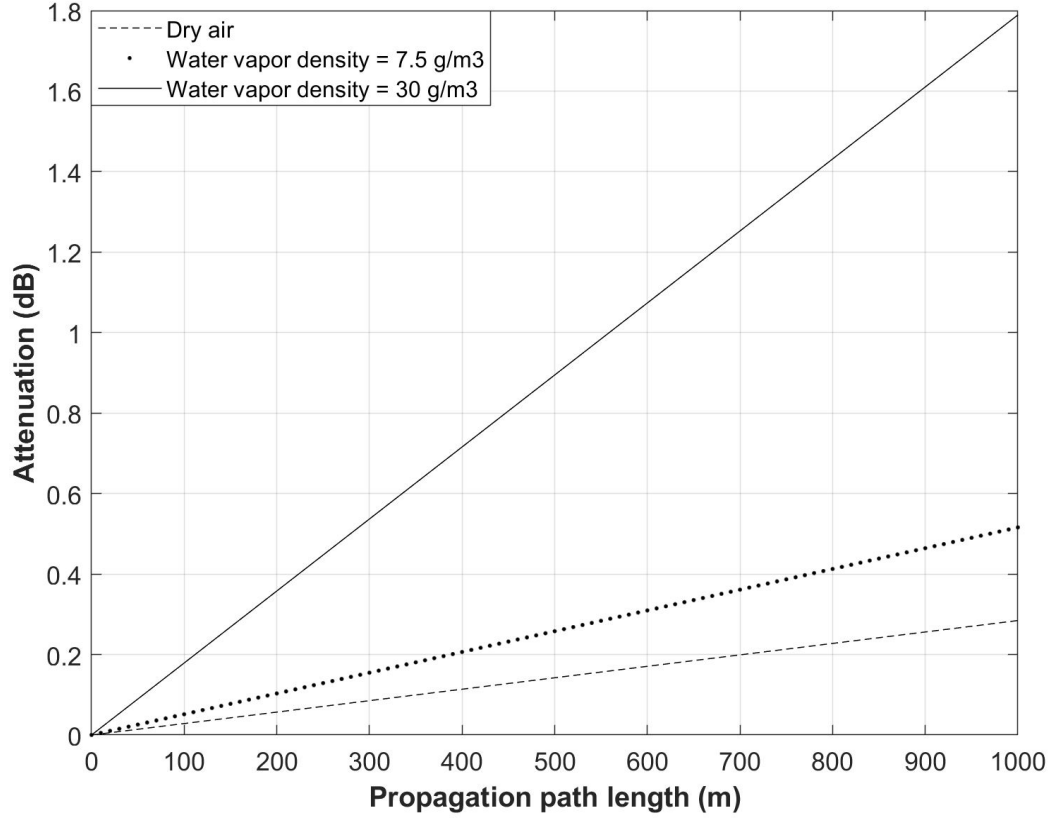


Figure. 2.26 RF signal attenuation over propagation path length at 70GHz operating frequency obtained using Equations (2.16) and (2.17) for the water vapor density of 0 g/m<sup>3</sup> (i.e., dry air), 7.5 g/m<sup>3</sup>, and 30 g/m<sup>3</sup> (i.e., humid air)

### 2.9.5 Total RF Propagation Loss

According to the above discussion, the millimeter-wave signal will not only suffer free space propagation loss but the signal quality will also be adversely impacted by the real-time atmosphere in the deployment area. For example, the signal strength will be impacted by heavy rain, thick fog, and high-water vapor density in the air (i.e., high humidity) as well as other gaseous constituents in the air. Therefore, the total propagation path loss is given by Equation (2.26).

$$L_{\text{total}} (\text{dB}) = L_{\text{FS}} (\text{dB}) + L_{\text{r}} (\text{dB}) + L_{\text{c}} (\text{dB}) + L_{\text{g}} (\text{dB}) \quad (2.26)$$

Where,  $L_{FS}$  is the free space path loss,  $L_r$  is the path loss due to rain,  $L_c$  is the path loss due to cloud/fog, and  $L_g$  is the path loss for gaseous atmospheric constituents.

Figure 2.27 compares RF signal attenuation in an ideal free space propagation condition versus a realistic propagation environment including atmospheric impairments (e.g., rainfall, thick fog, humidity, etc.). The simulation parameters are listed in Table 2.4. The results depicted in Figure 2.27 illustrate a total signal attenuation increase of 7.885 dB at an operating frequency of 70 GHz when considering atmospheric factors such as heavy rainfall, thick fog, and high humidity.

Table. 2.4 Simulation parameters to calculate total propagation loss

<b>Propagation path length</b>	100 m
<b>Rainfall rate</b>	100 mm/hr
<b>Cloud liquid water density</b>	0.5 g/m <sup>3</sup>
<b>Temperature</b>	20 <sup>0</sup> C
<b>Atmospheric pressure</b>	101300.0 Pa
<b>Water vapor density</b>	30 g/m <sup>3</sup>

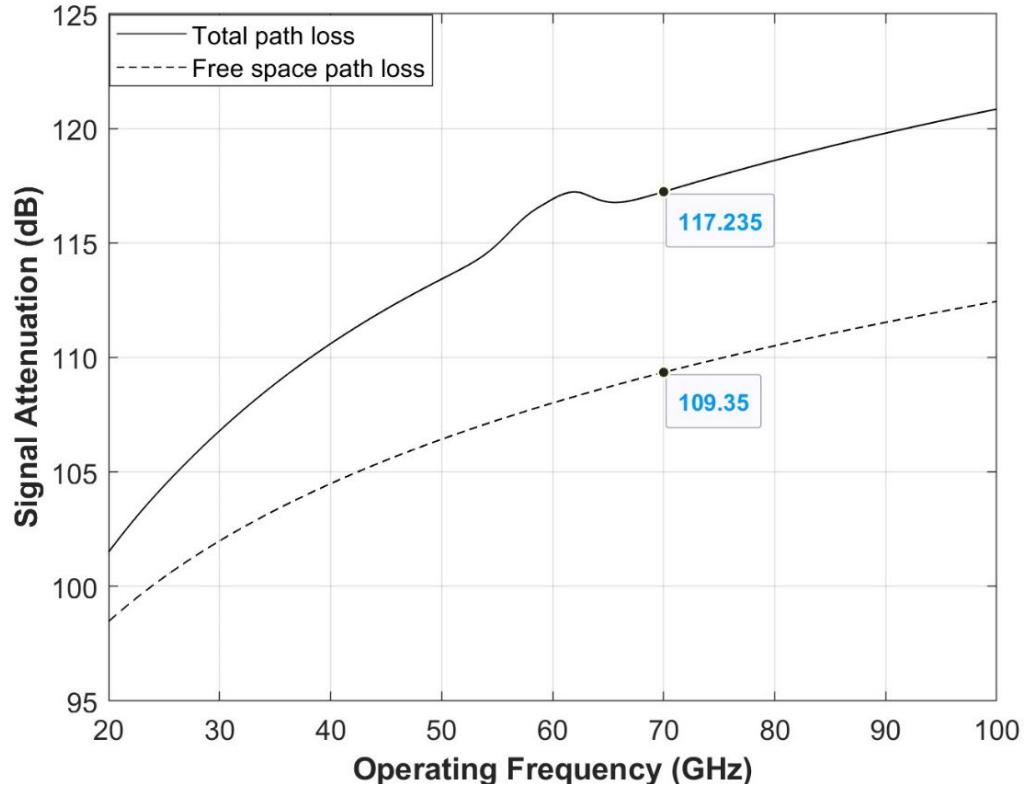


Figure. 2.27 Total signal attenuation at various operating frequencies obtained using Equation (2.13) for the free space and realistic propagation environment

In addition, total signal attenuation not only increases with the operating frequency but also increases significantly with propagation path length, as shown in Figure 2.28. This figure illustrates that for an operating frequency of 70 GHz, the signal attenuation increases by approximately 14 dB when path length increases from 100m to 200m. In order to achieve an acceptable receive signal level of at least -70 dBm throughout the deployment area, identification of ideal path length (i.e., cell radius) for each frequency spectrum (e.g., 30 GHz, 70 GHz, etc.) will be of utmost importance.

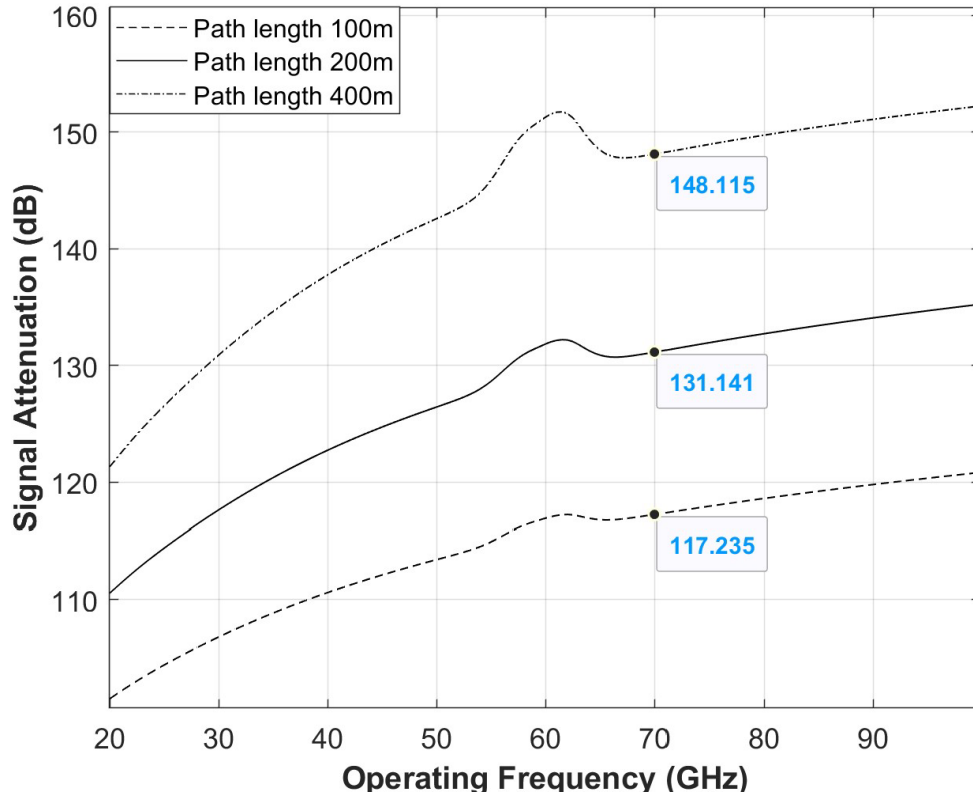


Figure. 2.28 Received signal attenuation (dB) at various operating frequencies (GHz) obtained using Equation (2.26) for the path length of 100m, 200m, and 400m

### 2.9.6 Signal Power Losses Associated with Transmitting and Receiving Antenna

In addition to the RF signal attenuation caused by the propagation medium between transmitter and receiver antennas, there are additional factors that result in RF signal losses associated with the transmitting and receiving antennas. This section illustrates the common sources of RF signal losses related to these antennas.

#### a) Feeder Loss / Cable Loss

Figure 2.29 provides an illustration of a typical 5G cell-site, emphasizing the RF cable connections between the antenna and the cell-site equipment. As the RF signal travels through the cable, a portion of the energy is absorbed by the cable known as feeder loss /

cable loss [45]. The total signal loss depends on factors such as the material properties of the cable, cable length, and operating frequency. The signal loss increases with both cable length and higher operating frequencies [46]. To minimize feeder loss, 5G network operators require high-quality RF cables (i.e., low loss cable) and should aim to reduce the cable length. In addition, routine monitoring and maintenance of these cables are essential to ensure optimal network performance.

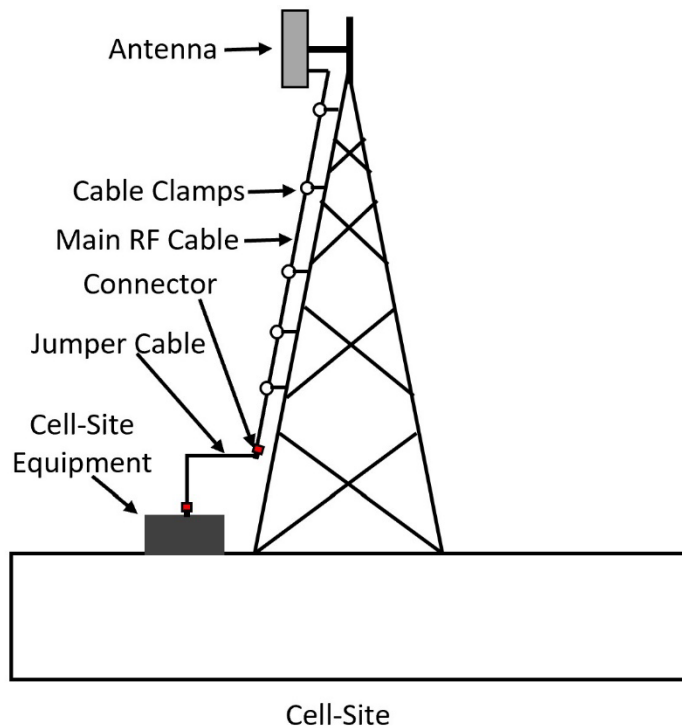


Figure. 2.29 A visual representation of the antenna feeder cable system in a 5G cell-site

#### b) Connector Loss

Various RF connectors are essential for establishing the link between the antenna and the cell-site equipment via RF cables, as depicted in Figure 2.29. As the RF signal travels through the cable, some of its energy is absorbed by these connectors, resulting in what is termed "connector loss." Improperly installed connectors can notably amplify

signal loss. To minimize connector loss, it's imperative to maintain connectors in good condition and tighten them to the correct torque value. Given that connectors can deteriorate over time due to weather conditions, regular maintenance and monitoring are necessary to uphold optimal performance.

c) Impedance Mismatch-Induced Loss

Typically, both the RF cable and antenna are designed to adhere to a standard impedance of 50 ohms [45]. Maintaining this matching impedance is essential to facilitate maximum power transfer to the antenna, enabling to emit a strong signal. When an impedance mismatch occurs, it can result in RF reflections, causing a portion of the RF power to be reflected back towards the cell-site equipment. These reflections can lead to a loss of efficiency and degrade signal quality in the system. To ensure optimal performance, it's important to measure both cable loss and the magnitude of RF reflections to identify and rectify any impedance mismatches within the cable and antenna system.

d) Polarization Mismatch-Induced Loss

The orientation of the radiated electric fields from the antenna is referred to as the polarization of the antenna. In wireless communication, antennas are typically designed to transmit and receive signals with a specific polarization. When the polarization of the transmitted signal differs significantly from the polarization of the receiving antenna, it results in what's known as polarization mismatch [31, 47]. This mismatch leads to a decrease in received signal power, as the antenna becomes less efficient at capturing signals with a different polarization.

Polarization of signals can change unpredictably in dense urban environments due to dynamic shifts in user device orientation, signal reflections, and multipath propagation

[48]. To mitigate such losses, 5G networks may utilize antennas with adjustable polarization or employ advanced polarization diversity techniques. Reference [48] illustrates a cell site antenna array with tunable polarization to minimize polarization mismatch.

e) Antenna Efficiency

As per the standard definition, antenna efficiency represents the ratio of power supplied to the antenna in comparison to the power emitted by the antenna [49]. Antenna efficiency decreases when the antenna cannot effectively convert received electrical signals into radiated electromagnetic waves or when it fails to capture incoming signals efficiently. The efficiency of an antenna is influenced by various factors, including its design and the quality of its materials. Inefficient antennas can cause a portion of the transmitted or received signal to be lost or wasted, resulting in reduced overall wireless communication system performance. To minimize losses due to antenna efficiency in 5G networks, network designers must choose and deploy high-quality antennas suitable for the required operating frequencies [50]. Additionally, regular antenna maintenance and monitoring are crucial to ensure they consistently operate at peak efficiency levels.

f) Body Loss

When the RF signal traverse through human body, it encounters signal attenuation due to absorption, scattering, and reflection, commonly referred to as body loss [51]. The total attenuation contingent on several factors such as the operating frequency of the signal, the composition and density of the object, and the distance between the transmitter and receiver antennas [51-53].



In LTE networks, a standard estimation for body loss is approximately 3dB [54]. Conversely, in the case of mmWave signals, there's minimal penetration but significant reflection and scattering due to the exceptionally small wavelength compared to the human body, resulting in substantial signal losses. Reference [55] demonstrates an average body loss of approximately 8.5 dB for measurements conducted at 28 GHz. However, it can escalate to as much as 25-30 dB for an individual at 60 GHz, as illustrated in [56].

Body loss can profoundly impact the performance of 5G networks, particularly when devices are placed close to users' bodies [51, 53, 56]. Network designers must account for body loss effects when planning and optimizing 5G network deployment to ensure that users receive a robust signal, even in challenging environment.

#### *2.9.7 RF Link Budget Analysis*

RF link budget is a mathematical equation that describes all power gain and loss experienced by the RF signal when propagating from transmitter to receiver along a communication link. This analysis is used to calculate the total power presented to the receiver. A typical RF link budget is shown in Equation (2.27) [11, 28, 38]:

$$P_{RX} = P_{TX} + G_{TX} - L_{TX} - L_{FS} - L_M + G_{RX} - L_{RX} \quad (2.27)$$

Where the  $P_{RX}$  is the receive signal power (dBm), and  $P_{TX}$  is the transmitted signal power (dBm). The transmitter and receiver antenna gains are represented by  $G_{TX}$  and  $G_{RX}$ , respectively; both are expressed in dBi.  $L_{TX}$  and  $L_{RX}$  represent the transmitter and receiver associated losses (e.g., cable loss, feeder, and connector loss, etc.), respectively and are expressed in dB.  $L_{FS}$  is the free space path loss between the transmitter and receiver. All other losses (e.g., atmospheric loss, fading margin, body loss, polarization mismatch, etc) are represented by the single parameter  $L_M$ , expressed in dB.

### 2.9.8 Signal-to-Noise Ratio (SNR)

Signal-to-Noise Ratio (SNR) is a critical parameter in wireless communication systems and represents the ratio of the received signal power to the noise power (i.e., external and internal system noise power) at the receiver. Equation (2.28) demonstrates the ratio of the signal power and thermal noise power in linear form [57]:

$$\frac{P_{Signal}}{P_{Noise}} = \frac{P_{RX}}{k T_s B_w} \quad (2.28)$$

Where  $P_{RX}$  denotes the received signal power, measured in watts. The Boltzmann constant is represented as  $k = 1.38 \times 10^{-23}$  Joules/Kelvin. The effective system noise temperature,  $T_s$ , is measured in  $^{\circ}\text{Kelvin}$ , and the system bandwidth,  $B_w$ , is measured in Hertz. Additionally, the system noise power at the receiver can be approximated at room temperature (i.e., 300 Kelvin) in dBm, shown in Equation (2.29):

$$P_{Noise}(dBm) = 10 \log_{10}(k T_s B_w) = 10 \log_{10}(B_w) dB - 173.8 dBm \quad (2.29)$$

Therefore, the Signal-to-Noise Ratio is represented in decibel, as depicted in Equation (2.30):

$$SNR (dB) = 10 \log_{10}(P_{RX}) dB - (10 \log_{10}(B_w) dB - 173.8 dBm) \quad (2.30)$$

In wireless communication, SNR is used to measure the quality of the received signal and is typically expressed in decibels (dB). A higher SNR indicates a stronger, more reliable received signal relative to the noise, which leads to better communication quality. Conversely, a lower SNR implies that the received signal is weaker and could be more susceptible to errors and degradation in quality. Once the antenna parameters (i.e., gain and losses) are known, the transmit power can be adjusted to overcome the total losses and

meet the required SNR [38]. This dissertation uses the 5G network specifications of IMT-2020 for 70 GHz operating frequency [30].

### 2.9.9 Calculate Required Transmit Power

Once the minimum required SNR value is determined from the 5G network specification (i.e., IMT 2020 [30]), the required receive signal threshold can be calculated for a certain propagation path length by using Equation (2.28). Finally, the required transmit power can be calculated by Equation (2.27).

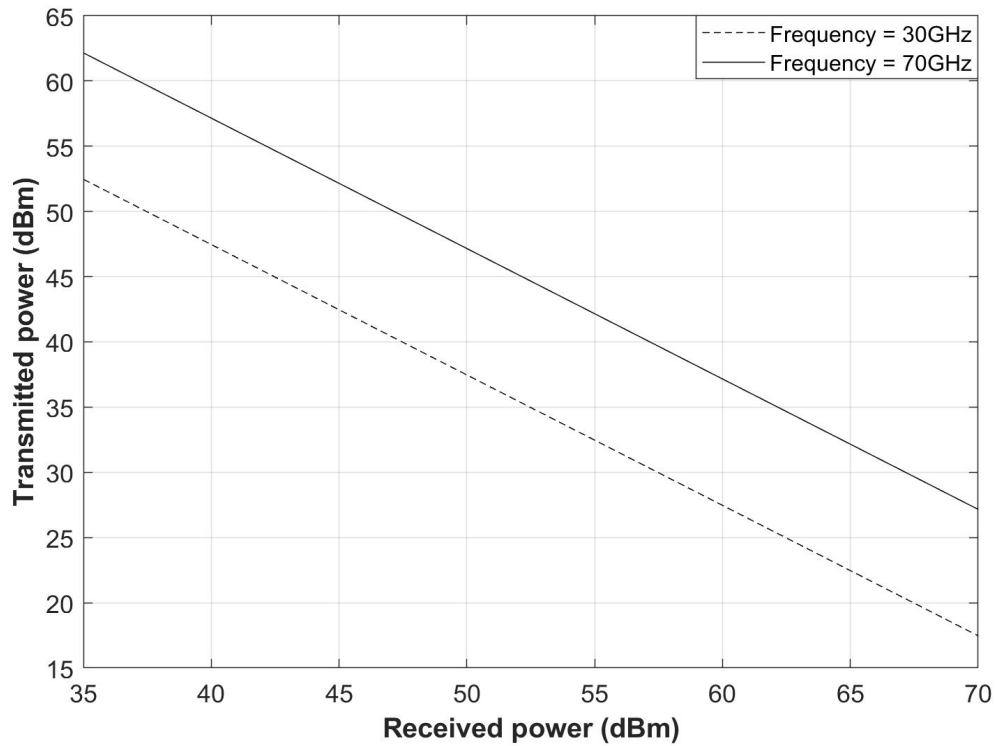


Figure. 2.30 The relationship between transmit signal power and received signal power obtained using Equation (2.27) for the operating frequency of 30GHz and 70GHz

Figure 2.30 shows the required transmit power versus the expected received power threshold for the 30 GHz and 70 GHz operating frequencies. The parameters used to generate this figure are listed in Table 2.5. From this figure we can deduce that the received

signal power is improved by increasing transmit power and that higher frequency signals require more transmit power to maintain a minimum received signal power threshold due to propagation loss. Therefore, the optimum transmitted power can be calculated for each cell site if the total propagation loss is estimated and the received power threshold is known from the specification (i.e., IMT 2020 [30]).

Table. 2.5 Simulation parameters to determine the required transmit power for strong signal coverage across the deployment area

Parameters	Values
Operating frequency	30 GHz and 70 GHz
Propagation path length	100 m
Rainfall rate	50 mm/hr
Cloud liquid water density	0.5 g/m <sup>3</sup>
Temperature	20 <sup>0</sup> C
Atmospheric pressure	101300.0 Pa
Water vapor density	30 g/m <sup>3</sup>
Transmit power	40 dBm
Transmitter antenna gain	10 dBi
Receiver antenna gain	8 dBi
Transmitter cable loss	3 dB/100m
Receiver cable loss	0.2 dB

### ***2.9.10 Literature Review for RF Propagation Modeling Candidates of 5G***

Several empirical propagation models (e.g., Okumura-Hata Propagation Model for rural, suburban, urban, and dense urban, etc.) are widely used for the 4G network planning

[58-60]. Although these empirical models do not perfectly predict absorption, their accuracy are sufficiently high to be appropriate for initial coverage planning and analysis.

Other models have been development, such as WINNER II [61] and 3rdGenerationPartnership Project (3GPP) [62] propagation models are well-known and widely used in industry due to diversity of deployment scenario (e.g., indoor office, shopping mall, and outdoor, etc.) [63]. However, these models are only applicable for operating frequencies below 6 GHz. For the same reason, all empirical models currently used in 4G networks can not be used for the millimeter wave spectrum (e.g., 70 GHz).

A number of measurement campaigns and channel modeling efforts have been conducted worldwide, such as by Nokia [64], Samsung [65, 66], and Kyro et al. from Aalto University [67]. Extensive measurements were carried out for indoor and outdoor channel measurement for 28, 38, 60, and 73 GHz operating frequencies [68-70]. 3GPP also releases traditional measurement-based statistical channel models applicable for frequencies 0.5 to 100 GHz [63, 71].

Three candidate propagation models for millimeter-wave spectra have shown promise for high accuracy. These models are the Alpha–Beta–Gamma (ABG) model [72], the Close-In (CI) free-space reference distance model [72], and the CI model with a frequency-weighted path loss exponent (CIF) [72, 73]. While these models have demonstrated accurate results under certain conditions, their accuracy greatly varies with operating frequency, propagation path length, and certain deployment scenarios. The authors in [73] show that all three models under-predict path loss when closer to the cell site and overpredict the path loss far from the cell site. It is also demonstrated that the CI

propagation model, as shown in Equation (2.31) [74], exhibits higher accuracy for outdoor environments. [74]:

$$PL^{CI}(f, d)[dB] = FSPL(f, d_0)[dB] + 10n \log_{10} \left( \frac{d}{d_0} \right) + X_{\sigma}^{CI}, \text{ where } d \geq d_0 \quad (2.31)$$

Where  $f$  is the operating frequency,  $d$  is the propagation path length,  $d_0$  is the close-in free space reference distance (i.e., 1 m),  $n$  is the path loss exponent,  $FSPL(f, d_0)$  denotes the free space path loss, and  $X_{\sigma}^{CI}$  is the zero-mean Gaussian random variable with a standard deviation  $\sigma$  in dB.

## 2.10 Define 5G cell site radius

The cell site radius is defined by the maximum distance from the cell site to the user at which the user receives a signal that meets the minimum SNR requirement and, as shown in Figure 2.1. The cell signal strength is typically reported in terms of Reference Signal Received Power (RSRP), measured in dBm [75]. The typical cell signal strength ranges from -60dBm (i.e., very strong signal) to -100dBm (i.e., extremely poor signal) [76]. For 3G and 4G networks, the desired cell signal strength throughout the deployment area was -70 dBm.

A robust cell signal results in a significantly higher signal-to-noise ratio, ensuring a superior network connection for users, as discussed in section 2.9.8. For instance, if the received signal level is -70dBm and the cell experiences a background noise level of -90dBm (i.e., low-level noise), the resulting signal-to-noise ratio will be much higher (i.e.,  $(-70\text{dBm}) - (-90\text{dBm}) = 20\text{dBm}$ ) [77]. It will favor the cell signal over noise and provide a better-quality network connection for the user. Conversely, when the cell signal strength is very weak (e.g., -85dBm) with a background noise level of -90dBm, the resulting signal-to-noise ratio is much lower (i.e.,  $(-85\text{dBm}) - (-90\text{dBm}) = 5\text{dBm}$ ). Consequently,

recovering the signal and sustaining traffic becomes challenging with such a feeble cell signal (e.g., -85dBm). Users may even experience signal outages due to a poor cell signal, significantly diminishing signal reliability.

The signal power attenuates as it propagates from the transmitter (i.e., 5G cell) towards the receiver (i.e., user), as described by Equation (2.27). Figure 2.31 displays received signal power at varying path lengths of 100m, 200m, 300m, and 400m, as a function of operating frequency, based on the parameters listed in table 2.5. Here we see that the received signal power of a 70 GHz operating frequency is attenuated by approximately 10.87 dBm with an increase in distance from 100m to 200m, although the received power in both cases is still acceptably strong (i.e., greater than -70 dBm). However, the signal attenuates an additional 8.38 dBm when increasing the distance further to 300m, and leads to a weak signal (i.e., less than -70 dBm). To maintain a strong signal throughout the deployment area, the 5G cell radius for 70GHz operating frequency can be close to 200m, and it must be less than 300m to avoid a weak signal.

Figure 2.31 also shows that the received signal power is strong (i.e., higher than -70dBm) with a 400m cell radius for 30GHz operating frequency but very weak for 70GHz operating frequency. Therefore, the cell radius will not be constant for 5G in different frequency spectrums (i.e., 6GHz, 30GHz, ant 70GHz, etc.). The MNOs must identify the appropriate cell radius for a specific operating frequency in a deployment area.

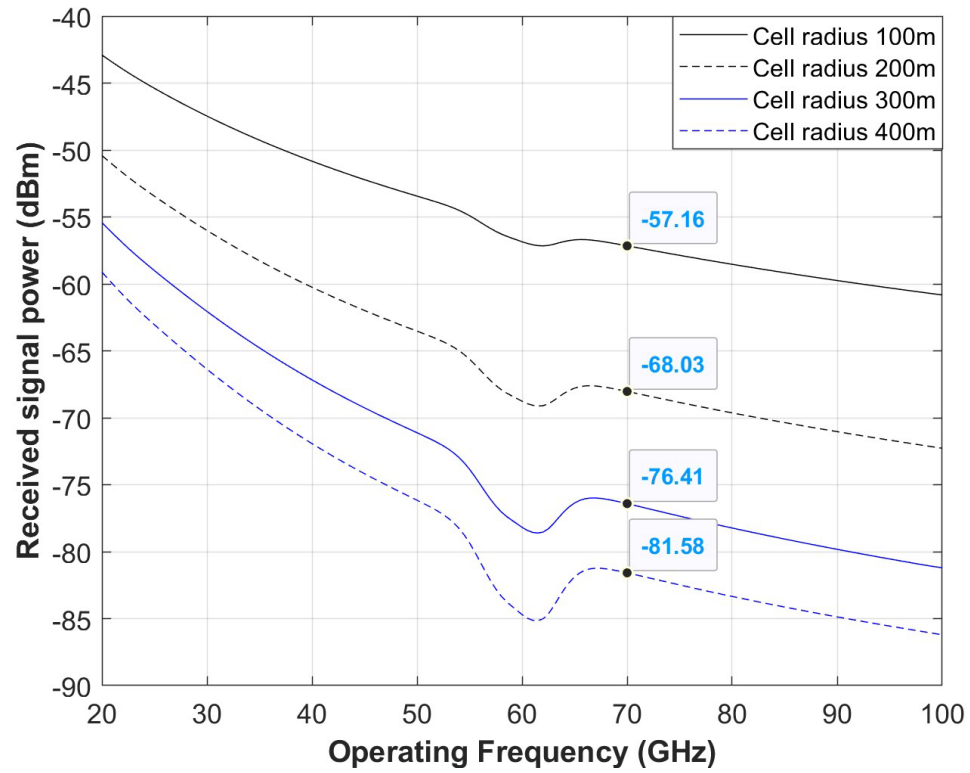


Figure. 2.31 Received signal power (dBm) at various operating frequencies (GHz) obtained using Equation (2.27) for the cell radius of 100m, 200m, 300m, and 400m



## CHAPTER 3

### RF COVERAGE SIMULATION AND ANALYSIS

#### 3.1 Introduction

Free-space propagation loss increases with frequency, as described in section 2.9.1. At millimeter-wave frequencies in the vicinity of 70 GHz this loss mechanism combines with the very short wavelength to lead to increased adverse effects of signal blockage. To mitigate these concerns and achieve optimal network performance at high frequency bands, a direct line of sight connection between the user (e.g., mobile phone handset) and cell site is needed [69, 70, 73]. This need for line of sight coverage leads to significant challenges in the design of 5G cell sites, especially in a dense urban environment. To estimate the coverage of the 5G network operating at millimeter-wave frequencies, this dissertation employs the free space propagation model described in Chapter 2, with special consideration given to line of sight coverage in the determination of candidate cell sites. This chapter presents simulation results of millimeter-wave coverage using the traditional three sector cells and discusses ways to optimize RF coverage for these networks. Options that are discussed include the use of advanced antenna arrays, optimum antenna downtilt angle and height, and appropriate operating frequency.

#### 3.2 RF Coverage Simulation Tool and Configuration of Simulation Parameters

##### *3.2.1 Embracing RF Coverage Simulation Tool*

Mobile operators can unlock substantial cost savings by adopting more advanced Radio Access Network (RAN) planning tools during the deployment of new networks [78]. A report by Infovista, a software company, highlights the potential for accurate RAN

planning to reduce a nationwide operator's capital expenditure costs by \$2 billion over a 10-year period [79].

Over the years, numerous RAN planning tools have been developed by different telecommunications companies. Among these tools, several are widely recognized for their support of mmWave frequency, including Planet (developed by Infovista) [80], Atoll (developed by Forsk) [81], and ASSET Radio (developed by TEOCO) [82]. These tools offer comprehensive support for multi-technology wireless networks, spanning GSM, UMTS, LTE, 5G, and more, all within a single project. Their popularity in RF coverage planning stems from their ability to provide up-to-date terrain profiles, encompassing surface elevation, buildings, trees, roads, and more, for precise RF coverage estimations.

However, these tools may have limitations when it comes to accommodating new propagation modeling techniques. For instance, Atoll employs Aster propagation modeling, while Planet leverages an AI-driven 3D propagation model. Designers using these tools may find themselves constrained in terms of incorporating new antennas outside of the tools' predefined selections. As these tools are typically developed around existing wireless network standards (e.g., GSM, UMTS, LTE), their suitability for emerging networks like 5G in the mmWave spectrum can be limited, offering little room for designers to integrate new design elements, such as custom propagation modeling or unconventional antennas.

In contrast, MATLAB provides an open platform for designers, granting them the flexibility to create antennas tailored to their specific needs and implement their own propagation models for RF coverage estimation. However, the accuracy of RF coverage estimates in MATLAB heavily relies on access to updated terrain profiles for the desired

geographical area. These profiles must encompass crucial data, including surface elevation, new buildings, trees, and roads.

It's worth noting that the RF coverage simulations presented in Chapters 3 and 4 in this dissertation employ a free terrain profile from Google Earth, which does not account for the impact of buildings and trees. In Chapter 5, the simulations use a terrain profile from OpenStreetMap [83], incorporating data on buildings and trees for more precise signal strength measurements.

For the RF coverage simulations throughout Chapters 3, 4, and 5, this dissertation leverages MATLAB in conjunction with Communications Toolbox, Antenna Toolbox, and Phased Array System Toolbox, offering a versatile and customizable platform for in-depth analysis. It's noteworthy that the University of North Dakota offers licenses for MATLAB along with these supplementary toolboxes. However, it should be noted that subscriptions for the RAN planning tools mentioned earlier come with a substantial cost.

### *3.2.2 Parameters Configuration for RF Coverage Simulations*

This dissertation follows the IMT-2020 guidelines [30] for 5G network planning, which encompass critical antenna-related parameter configurations. These parameters encompass operating frequency, bandwidth, single antenna radiation pattern, transmit power, cell site, receiver antenna height above ground, antenna gain, noise figure, inter-site distance, and more. Table 3.1 provides a comprehensive overview of the essential simulation parameters employed for the RF coverage simulations presented in this chapter.

To illustrate realistic simulation scenarios, Iowa State University serves as the designated deployment area. Throughout Chapters 3, 4, and 5, all RF coverage simulations rely on the total loss Equation (2.26), as developed in section 2.9, to estimate the overall

signal attenuation across the deployment area. As an example, these simulations assume specific environmental conditions, including moderate rain (with a rainfall rate of 50 mm/hr), moderate fog (with a liquid water density of 0.25 g/m<sup>3</sup>), and humid air (with a water vapor density of 155 g/m<sup>3</sup>). These factors are considered in addition to the free space propagation loss when calculating the total signal attenuation.

Table. 3.1 The parameters employed for simulating RF coverage and computing Signal-to-Interference-plus-Noise-Ratio (SINR) values in the simulation

<b>Parameters</b>	<b>Values</b>
<b>Operating Frequency</b>	70 GHz
<b>Bandwidth</b>	80 MHz
<b>BS Antenna height (above ground level)</b>	25 m
<b>BS Transmit power</b>	40 dBm
<b>BS Antenna gain</b>	10 dBi
<b>BS Antenna noise figure</b>	7 dB
<b>Receiver height (above ground level)</b>	1.5 m
<b>Receiver noise figure</b>	7 dB
<b>Receiver gain</b>	8 dBi
<b>BS Antenna downtilt</b>	15 <sup>0</sup>
<b>Inter-site distance</b>	400 m
<b>Individual cell site radius</b>	200 m
<b>No. of cell sites</b>	7
<b>No. of sectors per cell</b>	3
<b>Cell sector angles</b>	30 <sup>0</sup> , 150 <sup>0</sup> , and 270 <sup>0</sup>

### 3.3 RF Coverage Simulations: Employing Single Antenna Element in Every Sector

Figure 3.1 depicts the results of RF coverage and signal strength simulations for a cluster of seven cells. To illustrate, the central cell is situated behind the Stanton Memorial Carillon at Iowa State University. The hexagonal shapes surrounding each cell approximate the respective cell boundaries. It's crucial to emphasize that the simulation results presented in the following sections of this chapter rely on a terrain profile obtained from Google Earth. This profile, however, does not account for the influence of buildings and trees within the deployment area.

The simulation outcomes reveal robust signal strength of approximately -50 dBm in areas proximate to each cell and in the direction of their respective sectors. However, a significant portion of the deployment area experiences weak signal strength, registering below -70 dBm.

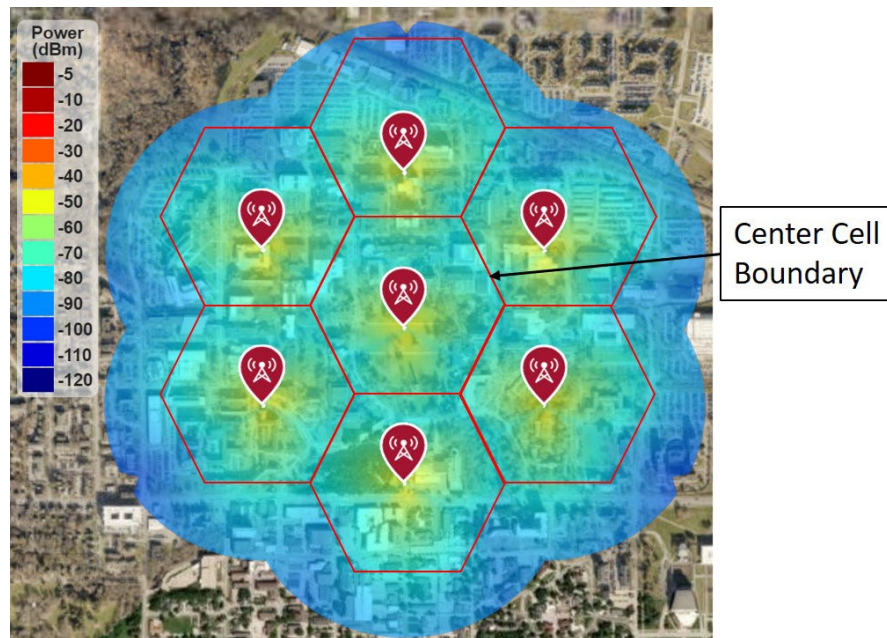


Figure 3.1 A map of RF coverage and signal strength for a collection of seven cell sites.

Each site is equipped with three sectors, each with one antenna element.

To assess the impact of interfering signals across the entire deployment area (i.e., same as Figure 3.1), Figure 3.2 provides RF coverage and SINR simulation results. Notably, the single antenna element used here exhibits a radiation pattern with a considerably wider beamwidth (Half Power Beam Width of 65 degrees), as detailed in section 2.8.1. This wider beamwidth leads to RF signals overlapping with the neighboring sectors of each cell, thereby introducing interference. Consequently, areas where the neighboring sectors of each cell overlap experience a lower SINR value.

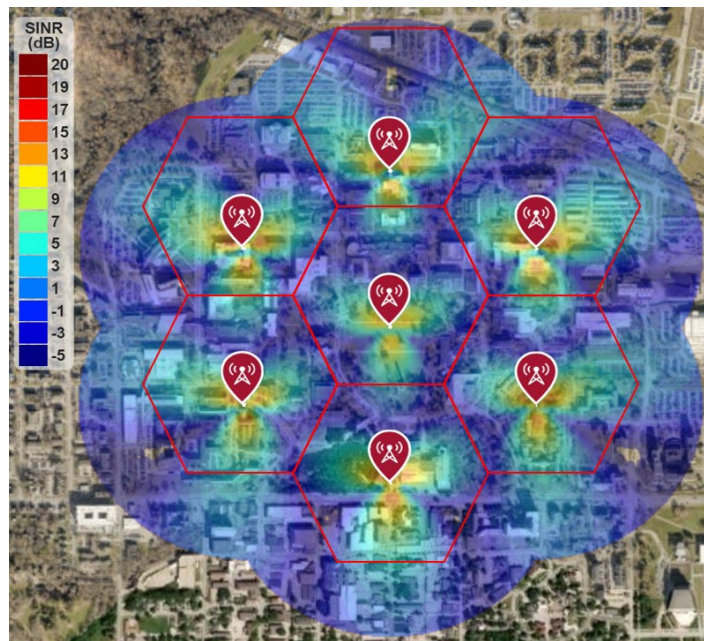


Figure 3.2 A map of RF coverage and SINR for a collection of seven cell sites. Each site is equipped with three sectors, each with one antenna element.

Moreover, owing to the combination of a small cell radius (200 meters), a compact inter-cell distance (400 meters), and high-gain directional antennas, RF signals extend beyond the boundaries of each cell. To illustrate, the central cell encounters interference from all six neighboring cells. Consequently, a substantial portion of the central cell's area



exhibits a diminished SINR, often falling below 7 dB, except for regions in close proximity to the cell and aligned with each of its individual sectors.

### 3.4 RF Coverage Simulations: Employing 8-by-8 Antenna Array in Every Sector

Section 2.8.3 elucidates that the 8-by-8 Antenna Array furnishes a radiation pattern characterized by high directivity, measuring at 21.72 dBi, and a narrow beamwidth, boasting a Half Power Beam Width of merely 35.8 degrees. In the subsequent Figure 3.3, we delve into RF coverage and signal strength simulations to examine the implications of RF signal strength across an extended deployment area encompassing 19 cell sites. The central cell retains its position, coinciding with the configuration in Figures 3.1 and 3.2.

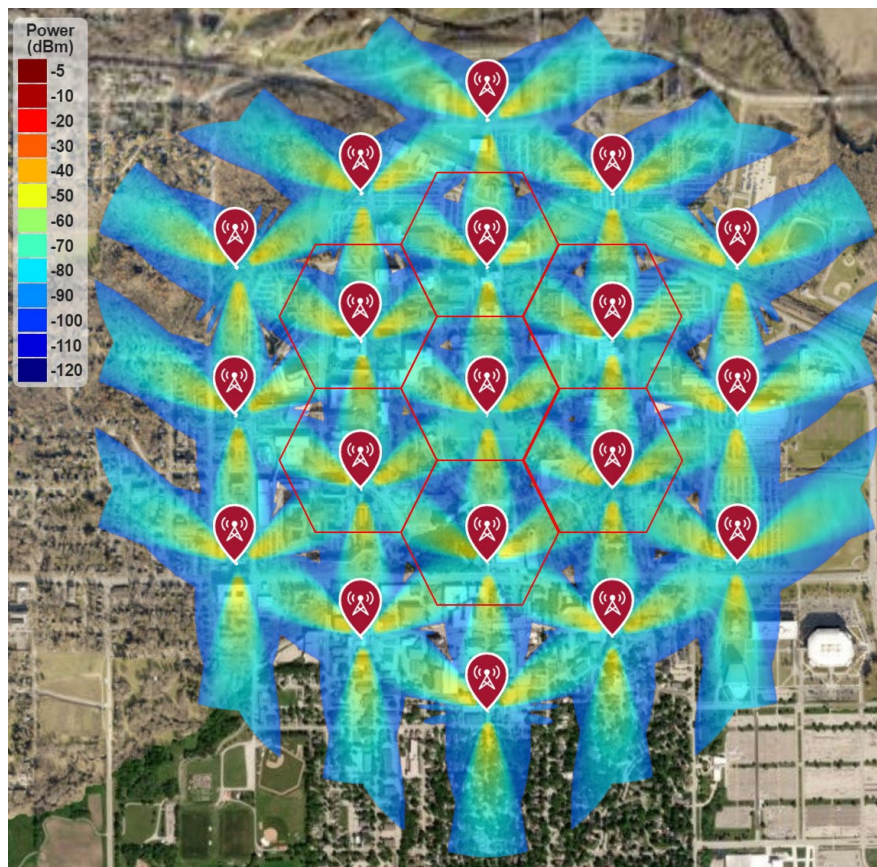


Figure 3.3 A map of RF signal strength for a collection of seven cell sites. Each site is equipped with three sectors, each with an 8-by-8 Antenna Array in contrast to Figure 3.1.

The simulation outcomes unveil that RF signal strength reaches its pinnacle in the direction of each sector, attaining a maximum signal strength of -50 dBm. Conversely, RF signal strength significantly diminishes in all other directions, plummeting below -70 dB. Furthermore, the simulations underscore that an increase in high-power interfering signals emanating from neighboring cells amplifies interference levels, shown in Figure 3.4.

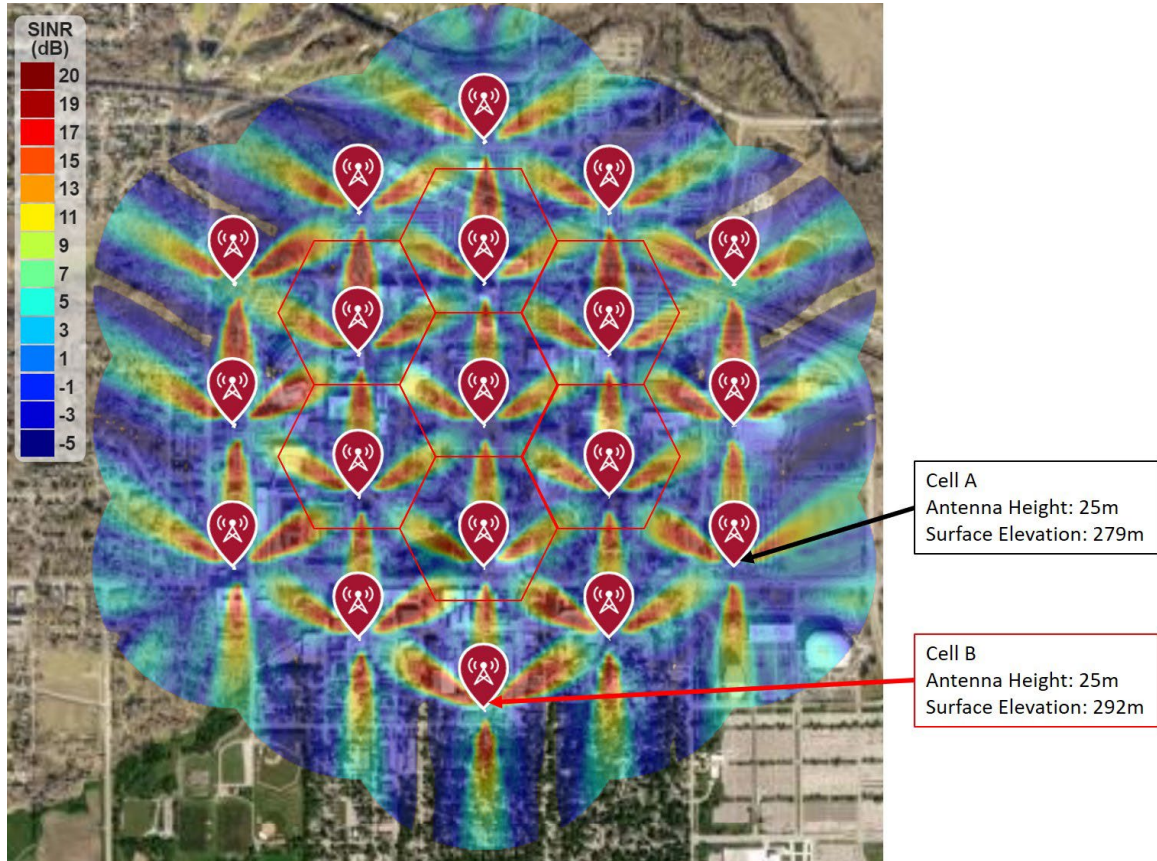


Figure 3.4 A map of RF coverage and SINR for a collection of 19 cell sites. Each site is equipped with three sectors, each with an 8-by-8 Antenna Array in contrast to Figure 3.2

By replacing the single antenna element of each sector with an 8-by-8 uniform phased array antenna, the SINR significantly improves throughout the deployment area as shown in Figure 3.4. The maximum SINR level reaches 20dB in the direction of each



sector, compared to 13dB with the single antenna element. However, the SINR level is not uniform for each cell site, even when using the same antenna height of 25m Above Ground Level (AGL), due to differences in surface elevation throughout the deployment area. For instance, Figure 3.4 shows that Cell A has a surface elevation of 279m, while Cell B has 292m. Thus, the SINR level will differ for these two cell sites, and the MNOs will need to adjust the AGL according to the surface elevation to achieve the expected SINR level across the deployment area.

### 3.5 RF Coverage Simulations: Employing 16-by-16 Antenna Array in Every Sector

However, enlarging the array size from 8-by-8 to 16-by-16 for each transmitter results in a decrease in average signal strength across most deployment areas, as illustrated in Figure 3.5.

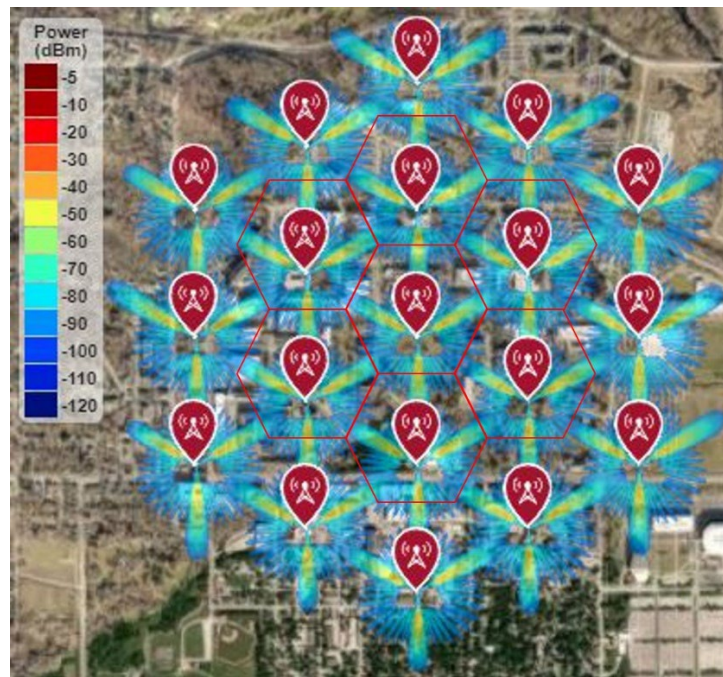


Figure 3.5 A map of RF signal strength for a group of 19 cell sites, each of which is equipped with three sectors, each featuring a 16-by-16 Antenna Array in contrast to Figure 3.3

The findings also indicate that a majority of the deployment areas will exhibit weak signals, measuring below -70 dB, thereby leading to suboptimal network performance. This is primarily attributed to the narrow and highly directional radiation beam produced by the 16-by-16 array antenna, resulting in maximum RF signal strength (exceeding -60 dB) exclusively in the direction of each sector and minimal signal strength in all other directions. To potentially address this challenge, one proposed solution is to incorporate a larger number of sectors per cell site, such as 6, 9, or 12. This approach is comprehensively discussed in section 4.3.

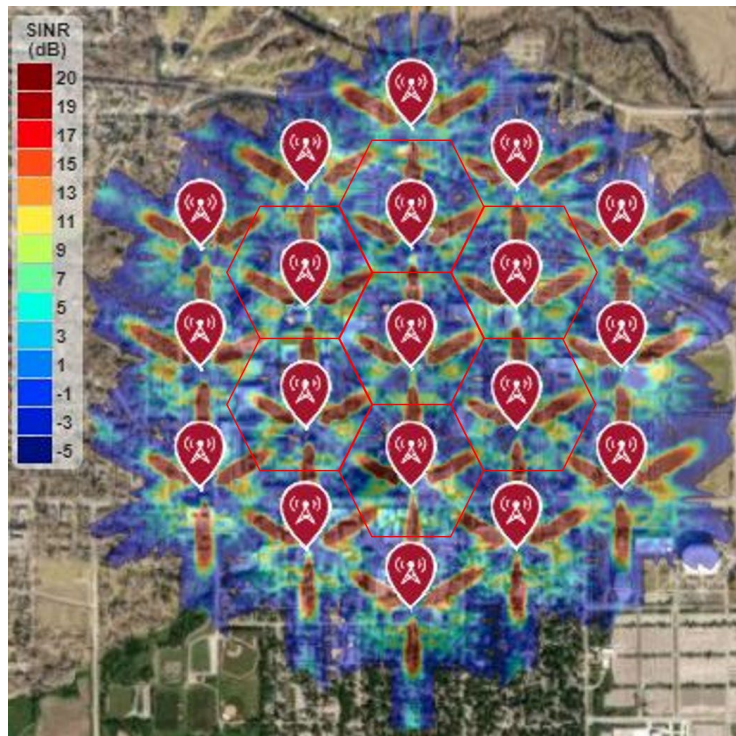


Figure 3.6 A map of RF coverage and SINR for a collection of 19 cell sites. Each site is equipped with three sectors, each with a 16-by-16 Antenna Array in contrast to Figure 3.4

Figure 3.6 illustrates that the best SINR is attained when all transmitters utilize a 16-by-16 uniform phased array antenna. As the number of elements in the array increases,

the array gain (i.e., directivity) improves, resulting in a significant enhancement in peak SINR. The radiation pattern of the array becomes highly directional as the number of antenna elements increases, leading to the highest SINR in the direction of each sector, while other directions experience lower SINR levels. Consequently, some areas enjoy excellent SINR (i.e., 20dB), while others experience poor SINR levels (i.e., below -5dB of SINR).

It's essential to highlight that elevated SINR levels are fundamental for achieving optimal 5G network performance, which encompasses critical metrics like ensuring 99.99% network availability, maintaining 99% network reliability, and achieving maximum data rates. As exemplified by the simulation results discussed in sections 3.3, 3.4, and 3.5, increasing the number of antenna elements per array results in improved SINR levels in the direction of each sector, while the rest of the deployment area experiences lower SINR levels.

To address this challenge, Chapter 4 introduces the concept of higher-order cell-sectorization, as expounded upon, aimed at enhancing the average SINR across the entire deployment area. Furthermore, the utilization of phased array antennas is explored, allowing for precise adjustment of the phase of individual elements to steer the primary signal beam in various directions, thereby augmenting 5G network coverage.

### **3.6 Improved RF Coverage Through the use of Advanced Antenna Systems**

Section 2.5 elucidates the concept of Carrier-to-Interference (C/I) ratios within a hexagonal cell geometry, emphasizing that an increase in interference signals from neighboring cells results in a decreased Carrier-to-Interference Ratio (C/I), thereby leading to diminished network performance. Given that all the simulation results in the preceding

section consistently demonstrate signal overlap from neighboring cells throughout the entire deployment area, it is evident that this situation results in a reduced C/I and, consequently, suboptimal network performance. Consequently, meticulous RF coverage planning becomes imperative to ensure a robust C/I ratio across the deployment area.

One effective strategy to manage RF signals within cell boundaries and mitigate interference with neighboring cells is Base Station (BS) antenna downtilt, as outlined in reference [19]. Figure 3.9 provides an illustrative representation of a typical downtilt scenario. This section examines the impact of downtilt on RF coverage and signal strength.

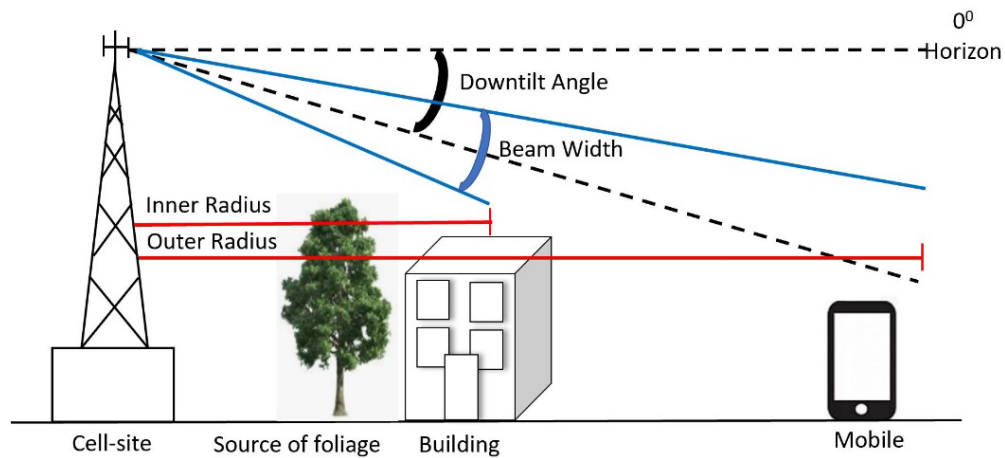


Figure 3.7 A visual representation of RF coverage incorporating antenna downtilt [7]

### 3.6.1 Types of Base Station (BS) Antenna Downtilt

Two primary methods are used for BS antenna downtilt: (a) Mechanical downtilt and (b) Electrical downtilt; these two methods are illustrated in Figure 3.8. The system design can use either method to tilt the radiated beam.

- a) Mechanical downtilt: The simplest installation has an antenna mounted directly to a vertical mast, as illustrated in Figure 3.8 (a), resulting in a radiation pattern that points towards the horizon. Mechanical downtilt physically orients the antenna to

point the radiated beam in the desired downtilt direction as illustrated in Figure 3.8 (b). While this approach is very simple, it does not uniformly reduce coverage.

b) Electrical downtilt: The electrical downtilt is achieved by changing the phase of each element of the phased array antenna, as illustrated in Figure 3.8 (c). The resulting radiated beam reduces coverage uniformly. Several methods have been identified to achieve electrical downtilt, including:

- Fixed electrical downtilt: This approach employs a BS antenna with a main beam that points in a fixed direction that cannot be adjusted after fabrication.
- Remote electrical downtilt: This approach uses a BS antenna that incorporates circuit elements that can be used to adjust the antenna beam direction remotely.

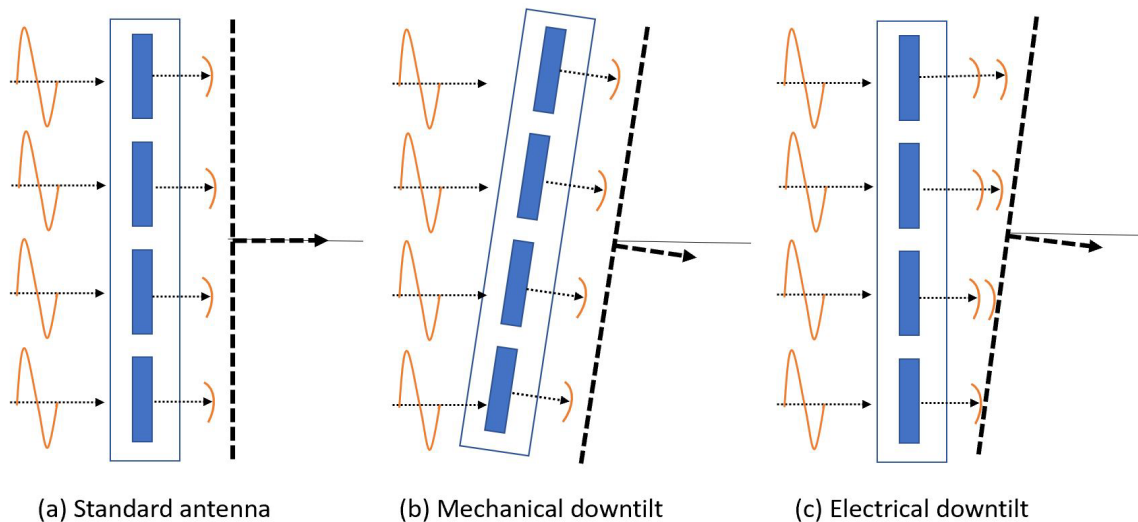


Figure 3.8 An illustration showing the antenna downtilt of a base station using (a) a standard antenna, (b) mechanical downtilt, and (c) electrical downtilt. [7]

The system designer has the option of using any of these methods to achieve electrical downtilt. However, variable electrical downtilt methods are typically more expensive than fixed electrical downtilt methods.

### **3.6.2** *RF Coverage Versus BS Antenna Downtilt Angle*

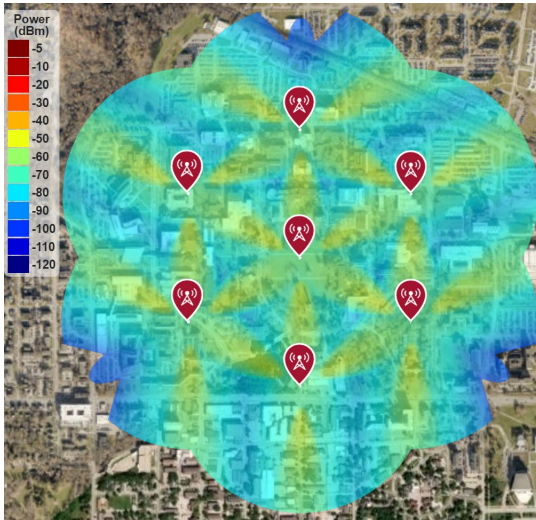
With the increase in the number of antenna elements, transitioning from a single antenna element to 8-by-8 and 16-by-16 configurations, the radiation beam becomes narrower and highly directional, a concept explored in section 2.8. Consequently, determining the appropriate downtilt angle becomes paramount for constraining RF coverage within the cell boundary and minimizing interference to neighboring cells. It's important to note that all the simulation results presented in this section adhere to the simulation parameters outlined in section 3.2.2, with the exception of the total signal attenuation calculation, which considers light rain (16 mm/hr) and dry air (water vapor density 7.5 g/m<sup>3</sup>) in addition to free space propagation loss.

- a) **Determining Appropriate Downtilt Employing 8-by-8 Antenna Array in Every Sector:** Figure 3.9 presents a comparative analysis of RF coverage and signal strength simulations for a cluster of seven cells, each equipped with three sectors, and employing 8-by-8 antennas in each sector. For the sake of illustration, all simulation parameters (e.g., 25m AGL and 400m inter-site distance) remain consistent across the simulations displayed in Figure 3.9, except for variations in the downtilt angle.

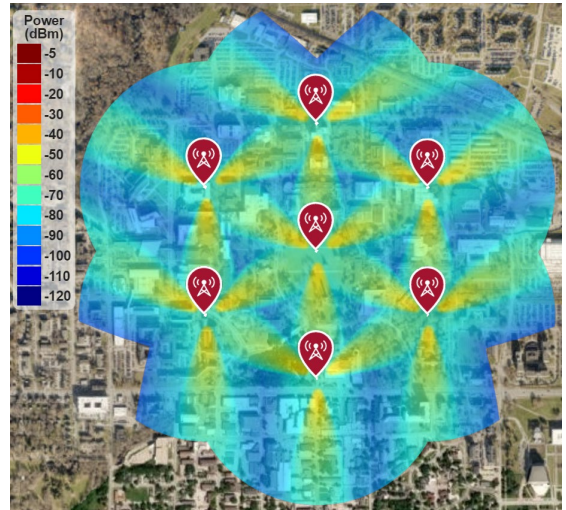
The results illustrate that when the downtilt angle is set at 30 degrees, RF coverage is constrained within the cell boundary. However, if the downtilt angle is increased to 40 degrees, the RF signal does not reach the cell boundary. Conversely, when the downtilt angle is reduced to 15 degrees, it reveals more significant signal overlap throughout the deployment area from neighboring cells. The maximum signal overlap is observed when the downtilt angle is set to zero degrees.



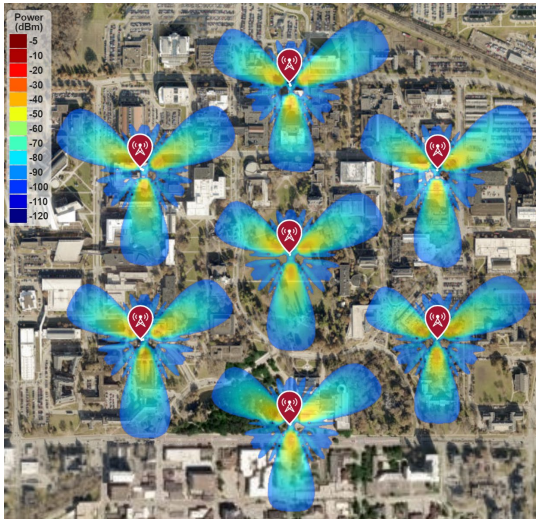
(a) 8-by-8 array and  $0^\circ$  downtilt



(b) 8-by-8 array and  $15^\circ$  downtilt



(c) 8-by-8 array and  $30^\circ$  downtilt



(d) 8-by-8 array and  $40^\circ$  downtilt

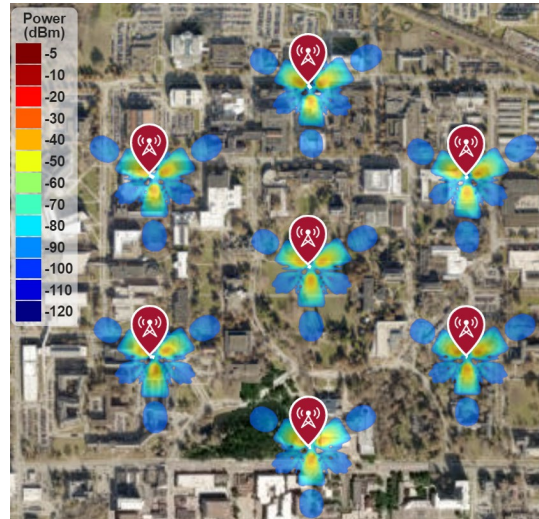


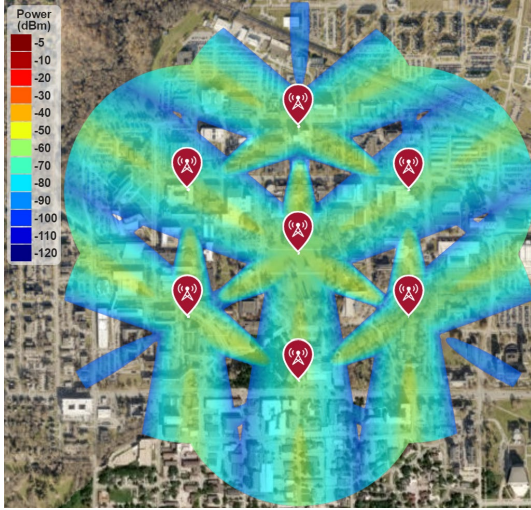
Figure 3.9 A comparison of RF signal strength is depicted for a group of seven cell sites in contrast to Figures 3.1, 3.3, and 3.5. Each site is fitted with three sectors, each having 8-by-8 antenna arrays and different downtilt angles.

- b) Determining Appropriate Downtilt Employing 16-by-16 Antenna Array in Every Sector: To illustrate, assume that the simulation parameters remain consistent with the previous simulation results depicted in Figure 3.9, with the exception of replacing the 8-by-8 Antenna Array with a 16-by-16 Antenna in every sector. The

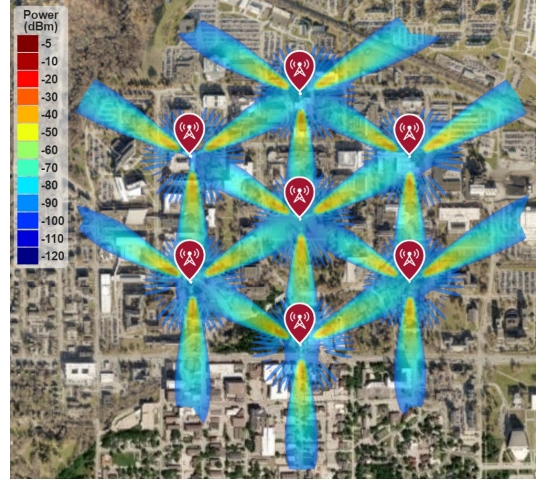


outcomes demonstrate that when the downtilt angle is established at 20 degrees, RF coverage is confined within the cell boundary.

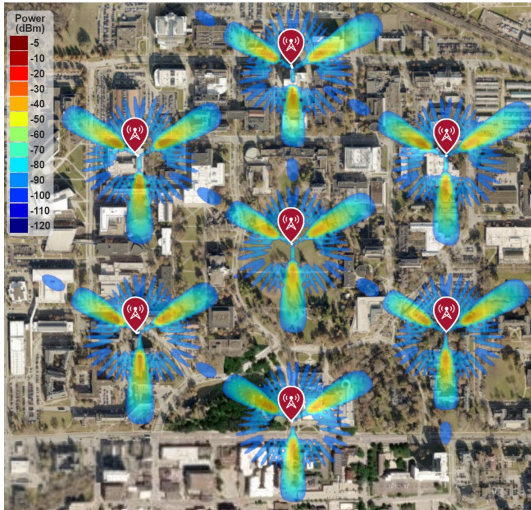
(a) 16-by-16 array and  $0^0$  downtilt



(b) 16-by-16 array and  $15^0$  downtilt



(c) 16-by-16 array and  $20^0$  downtilt



(d) 16-by-16 array and  $40^0$  downtilt

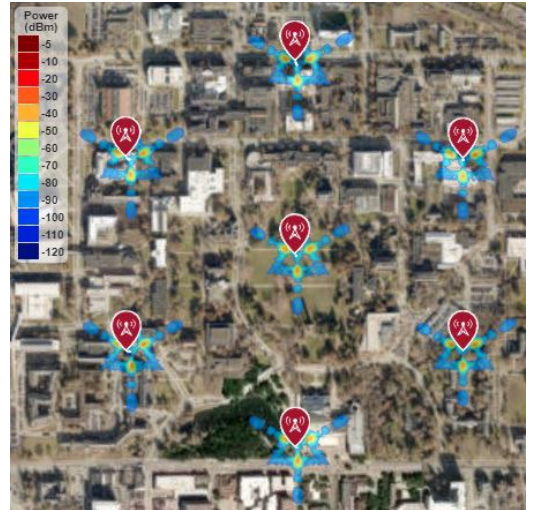


Figure 3.10 A comparison of RF signal strength is depicted for a group of seven cell sites in contrast to Figures 3.9. Each site is fitted with three sectors, each having 16-by-16 antenna arrays and different downtilt angles.

However, increasing the downtilt angle to 40 degrees results in the RF signal remaining close to the cell boundary without reaching it. Conversely, reducing the downtilt



angle to 15 degrees reveals more pronounced signal overlap throughout the deployment area from neighboring cells. The maximum signal overlap is observed when the downtilt angle is set to zero degrees, mirroring the findings from previous antenna configurations.

### 3.6.3 RF Coverage Versus Operating Frequency

As outlined in Section 2.9, RF propagation loss increases significantly in the millimeter-wave spectrum, with signal attenuation amplifying as the operating frequency rises. Figure 3.11 vividly illustrates the impact on RF coverage within a cluster of seven cell-sites, each housing three sectors and employing a transmitter equipped with an 8-by-8 uniform phased array antenna. For illustrative purposes, let's maintain the simulation parameters consistent with those seen in Figure 3.9 (c), while adjusting the frequency from 70GHz to 30GHz.

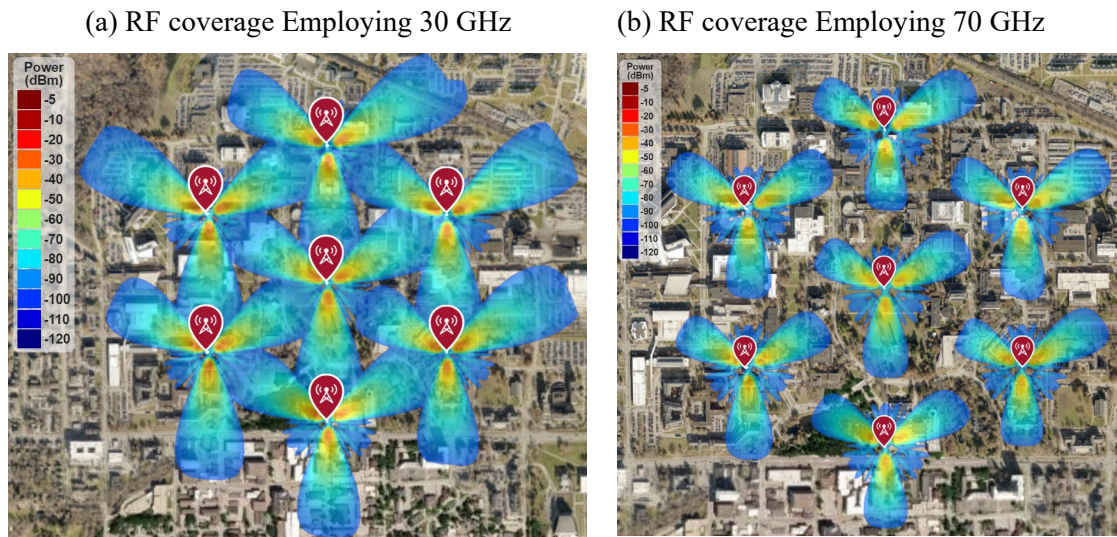


Figure 3.11 A comparison of RF signal strength among seven cell sites, each with three sectors and a transmitter using an 8-by-8 uniform phased array antenna for operating frequencies of 30GHz and 70GHz, in contrast to Figure 3.10

It is noteworthy that, with a 30-degree downtilt, RF signals were constrained to the cell boundary at the 70GHz operating frequency. However, for the 30GHz operating frequency, the RF signals extend beyond the cell boundary. Therefore, it becomes evident that operating frequency also plays a crucial role in determining the optimal downtilt angle, especially when considering transmitter settings, such as the use of an 8-by-8 or 16-by-16 antenna array.

#### **3.6.4** *RF Coverage Versus BS Antenna Height*

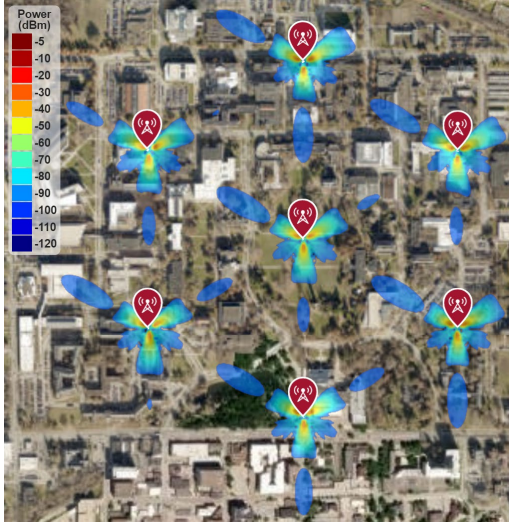
5G networks are expected to use higher frequency spectra (e.g., 24, 28, 39, 47 GHz) and larger array antennas (e.g., 32-by-32 elements). The ITU-2020 guidelines [30] specify a standard antenna height of 25 m for a 70 GHz frequency, but adjustments may be needed based on the cell site's physical location. Figure 3.12 illustrates the impact of varying antenna heights (15m, 20m, 25m, and 35m) on RF coverage for a transmitter with an 8-by-8 uniform phased array antenna, 30° antenna downtilt, and 70GHz operating frequency, in comparison to Figure 3.9(c).

The simulation results reveal that altering the antenna height above ground level (AGL) from the standard 25m to 30m introduces significant disparities in RF signal strength across the deployment area, potentially leading to RF signal spillage beyond the cell boundary and causing interference with neighboring cells. Conversely, reducing the antenna height AGL to 20m confines the RF coverage within the cell boundary but fails to reach the cell edge. The RF signal coverage further deteriorates when the antenna height is reduced to 10m, where the RF signal doesn't extend even halfway to the cell radius.

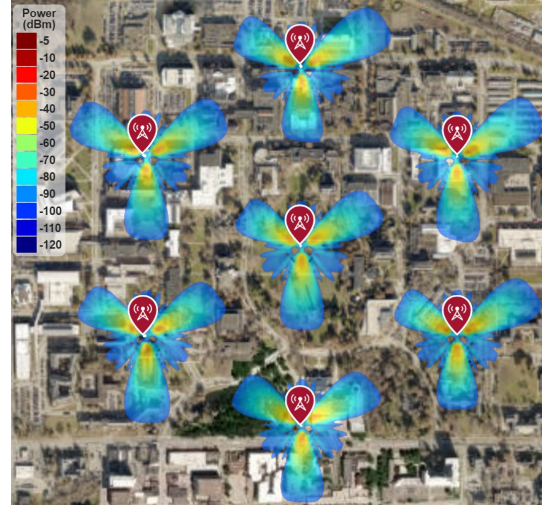
This effect is exacerbated when the antenna height is increased without the corresponding adjustment of the downtilt angle. Hence, it is essential for system designers

to conduct a comprehensive examination and precise calibration of transmitter settings in order to achieve the most favorable RF coverage for particular operating frequencies, taking into careful consideration the influence of both antenna height and downtilt angle on RF coverage.

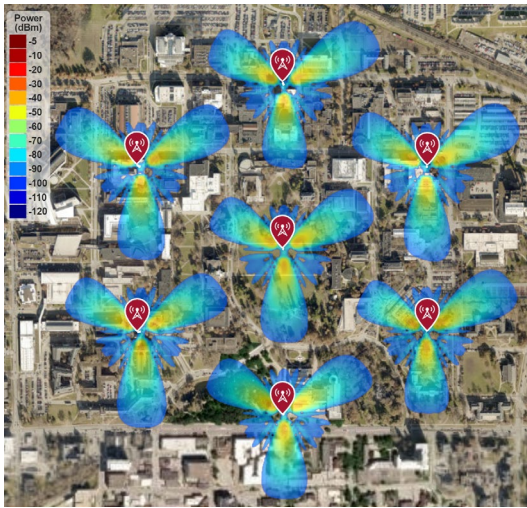
(a) 10m BS antenna height and  $30^\circ$  downtilt



(b) 20m BS antenna height and  $30^\circ$  downtilt



(c) 25m BS antenna height and  $30^\circ$  downtilt



(d) 30m BS antenna height and  $30^\circ$  downtilt

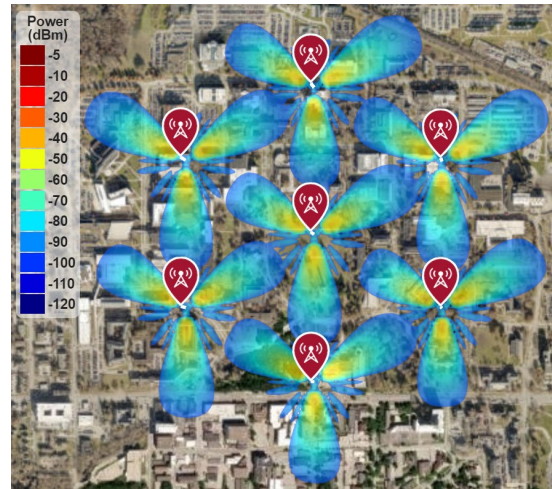


Figure 3.12 Comparison of RF Signal Strength Across Seven Cell Sites at 70GHz

Frequency with Varying Antenna Heights (10m, 20m, 25m, and 30m) Using an 8-by-8 Uniform Phased Array Antenna and  $30^\circ$  Antenna Downtilt, Contrasted with Figures 3.9 and 3.11.

## CHAPTER 4

### HIGHER-ORDER CELL-SECTORIZATION FOR 5G AND BEYOND

#### 4.1 Introduction

Chapter 2 underscores the efficacy of employing directional antennas for cell-sectorization, primarily to mitigate cochannel interference and bolster the Carrier-to-Interference ratio (C/I) within a system. Given the stringent performance demands of 5G networks, where achieving exceptionally high C/I value is paramount, there's a compelling need for advanced antenna systems characterized by narrow beamwidth and substantial directivity. As expounded upon in Chapter 3, the adoption of such highly directive antennas introduces an inherent challenge: substantial regions within the cell experience a notable absence of discernible RF power when employing a conventional three-sector configuration.

To surmount this limitation, the dissertation proposes higher-order cell-sectorization, specifically considering 9 or 12 sectors per cell. This strategic combination of highly directive antennas and higher-order sectorization effectively reconciles the imperatives of robust RF coverage, elevated C/I, and judicious energy consumption in the emerging 5G network paradigm. Figure 4.1 provides a visual representation of the architectural configurations for 9-sector ( $40^\circ$  each) and 12-sector ( $30^\circ$  each) cells, showcasing their interplay in achieving these objectives.

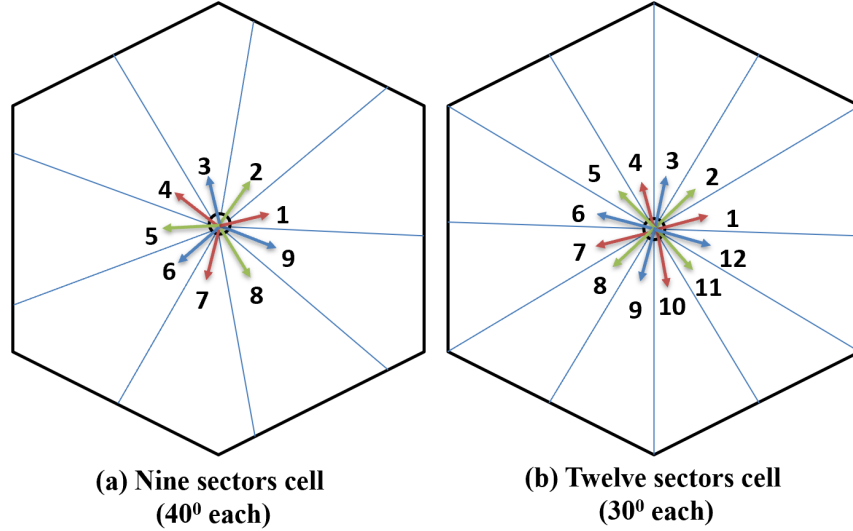


Figure 4.1 An illustration showing a revised 5G cell architecture in comparison to Figure 2.3: (a) a 5G cell divided into nine sectors, each with a 40-degree radiation pattern, and (b) a 5G cell divided into twelve sectors, each with a 30-degree radiation pattern.

#### 4.2 Literature Review on Higher-order Cell-Sectorization

Cell-sectorization is an appealing approach to cell site design as it allows full coverage within the cell using a collection of antennas that point in different directions and allows reuse of the frequency spectrum for sectors that point in different directions [19, 28]. The ability to reuse spectrum has allowed Mobile Network Operators (MNOs) to avoid the high cost [74] of installing additional cell sites in the same region to meet high traffic loads. In the current 4G network, highly directional antennas are often used to support up to 6 sectors per cell site [84].

Numerous research teams have delved into the application of higher-order cell-sectorization within 3G networks to attain substantial gains in capacity and network throughput [85-88]. Notably, reference [87] highlighted a significant capacity and throughput enhancement in a 3G/HSPA cell site when the number of sectors increased



from three to six, nine, twelve, and fifteen sectors deployed across Telefonica UK's network, spanning both Central London and the wider U.K. The study also revealed that adopting 6, 9, 12, and 15 sectorized cells, as opposed to the standard three sectors, expanded the cell site coverage area by 14%, 22%, 26%, and 31%, respectively. The authors presented an array of simulation results aimed at determining the optimal beamwidth for implementing a higher number of sectors per cell, such as 34 degrees for six sectorized cells, 20 degrees for nine sectorized cells, and 18 degrees for twelve sector cells. However, the authors did not elucidate the methods for achieving these specific beamwidth for each sector. Moreover, the paper did not delve into the appropriate antenna parameter configurations (e.g., antenna downtilt, antenna height AGL, etc.) required to optimize RF coverage when employing a higher number of sectors per cell.

In [89], the author conducted a comparison of capacity gain and RF coverage between 2.1GHz and 28GHz frequencies employing three and six sectorized cells. The results revealed a remarkable 556% increase in capacity when transitioning from a three sectorized cell to a six sectorized cell at the 28GHz frequency. However, it is noteworthy that the authors also observed a mean received signal strength 18dB higher at 2.1GHz compared to 28GHz. This discrepancy in signal strength underscores the influence of higher propagation loss at 28GHz relative to 2.1GHz, which would inevitably result in differences in cell radius when using identical simulation parameters (e.g., antenna height AGL, downtilt, etc.). Unfortunately, the authors did not offer insights into optimizing RF coverage when deploying higher frequency spectrums (e.g., 28GHz) with an increased number of sectors.

In [90], the study investigates the impact of higher-order sectorization on the performance of Millimeter Wave 5G Networks. The findings reveal a significant increase in data throughput as the number of sectors per cell increases to 4, 6, 8, and 10. However, it's noteworthy that the authors observed a decrease in the number of users achieving satisfactory SINR as the number of sectors per cell increased. Importantly, the authors did not provide in-depth insights into the implementation of 4-sector and 8-sector cells with appropriate beamwidth per sector. Additionally, guidance on optimizing RF coverage to improve SINR for users was not included in their findings.

In [85], the authors introduce a novel network tessellation for the deployment of 12-sector sites. They conducted a comparative analysis of throughput gains between twelve sectored cells and three sectored cells, varying the Inter Site Distance (ISD). The study reported a significant throughput gain of 210% for twelve sectored cells compared to three sectored cells when the ISD was set to 1000 meters. However, it's important to note that the authors did not examine the impact on RF coverage across the deployment area when the ISD was increased from 500 meters to 1000 meters.

In essence, previous research suggests that increasing the number of sectors per cell beyond three can lead to higher capacity and throughput gains. However, these studies often lack detailed insights into determining optimal antenna-related parameters (e.g., antenna downtilt and antenna height AGL) for optimizing RF coverage when deploying six, nine, or twelve sectored cells. Furthermore, these prior works typically assume a fixed set of antennas for implementing these configurations. For instance, if a designer initially deploys a cell with three sectored cells and later decides to upgrade it to a six-sectored cell, a completely new set of antennas must be acquired to provide the specific beamwidth

required for the six sectored cells. This integration of new antennas increases deployment costs for the operator.

To address these challenges, this dissertation introduces an adaptive cell sectorization technique that utilizes advanced phased array antennas. These antennas allow designers to adjust the number of sectors per cell without the need for additional antennas. The phased array antennas enable the creation of adaptive beamwidth by changing the number of antenna elements radiating in the array and adjusting the direction of the radiation beam by manipulating the phase of each antenna element, as discussed in Section 4.5. Additionally, this dissertation demonstrates the potential for energy savings through adaptive cell sectorization, particularly in deployment areas with variable traffic patterns, such as the contrast between maximum peak-hour traffic and minimal traffic during off-peak hours.

### **4.3 RF Coverage Versus the Number of Sectors Per Cell**

The conventional three sectors cell site architecture is effective for lower frequency spectra, such as sub 6 GHz for 5G, when utilizing smaller size array architecture, for instance, a 4-by-4 array. However, when we increase the operating frequency to the millimeter wave spectrum (e.g., 70 GHz) and employ a larger size array (e.g., 16-by-16 array), the antenna beam becomes highly directional and narrow, as discussed in section 2.8. As a result, the RF signal strength is at its peak in the line of sight direction for each sector but significantly diminishes in all other directions. This section investigates the effect on RF coverage when the number of sectors per cell site is increased to 6, 9, and 12 as opposed to the traditional three sectors cell site.



It's important to note that all the simulation results presented in this section adhere to the simulation parameters outlined in section 3.2.2, with the exception of the total signal attenuation calculation, which considers light rain (16 mm/hr) and dry air (water vapor density 7.5 g/m<sup>3</sup>) in addition to free space propagation loss. For illustration purposes, the same deployment area discussed in section 3.2.2 has been utilized to generate the RF coverage simulation results in this section.

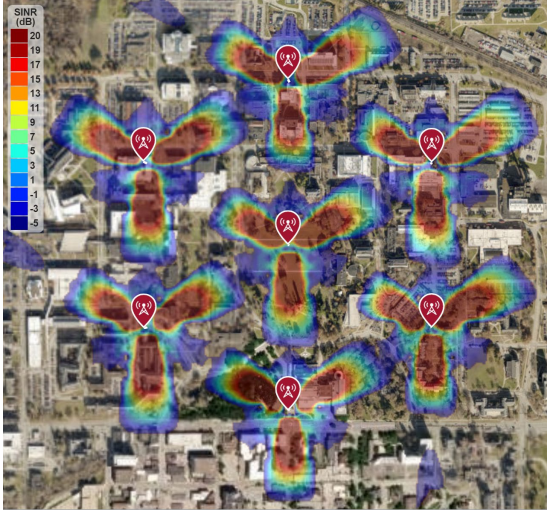
#### *4.3.1 Improved RF Coverage Employing 8-by-8 Antenna Array in Every Sector*

Figure 4.2 presents RF coverage and SINR results at 70 GHz, utilizing an 8-by-8 antenna array, with varying sector counts per cell site while keeping simulation parameters constant. The findings reveal that for a three-sectored cell architecture, as depicted in Figure 4.2(a), SINR peaks at 20 dB within the cell boundary and drops below 3 dB at the cell edge. However, much of the deployment area experiences poor SINR below 3 dB.

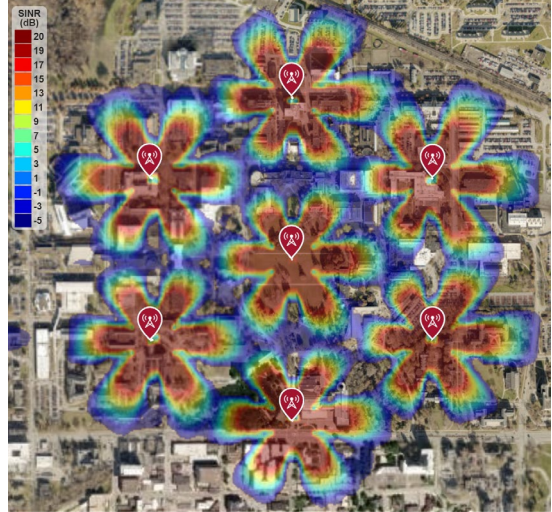
By transitioning to a six-sectored cell configuration, as shown in Figure 4.2(b), significantly enhances average SINR across the deployment area, achieving excellent SINR of 20 dB across most of the area. However, some regions still exhibit poor SINR below 11 dB.

The most optimal RF coverage is achieved when each cell site employs nine sectors, covering the entire deployment area with an excellent SINR of 20 dB, as demonstrated in Figure 4.2(c). However, employing twelve sectored cells, as shown in Figure 4.2(d), has a substantial impact on RF coverage. While it results in a maximum SINR of 20 dB in the direction of each sector, much of the deployment area experiences SINR below 11 dB. Nonetheless, the average SINR across the deployment area remains superior compared to the three-sectored cell configuration.

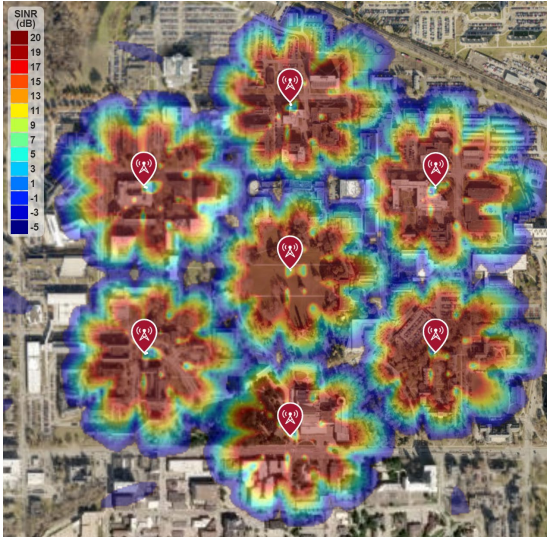
(a) RF coverage with 3 sectors cell



(b) RF Coverage with 6 sectors cell



(c) RF coverage with 9 sectors cell



(d) RF Coverage with 12 sectors cell

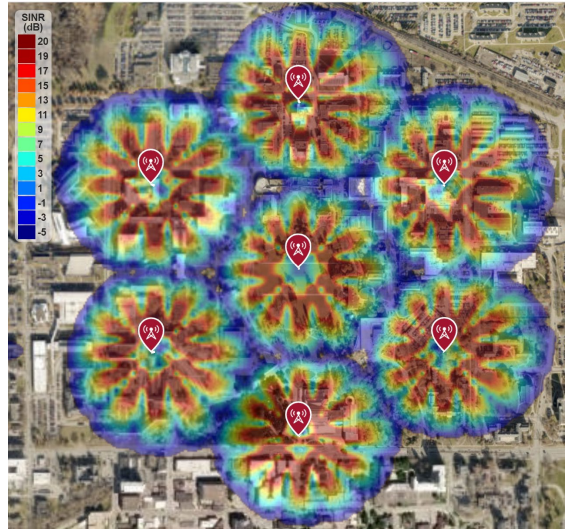


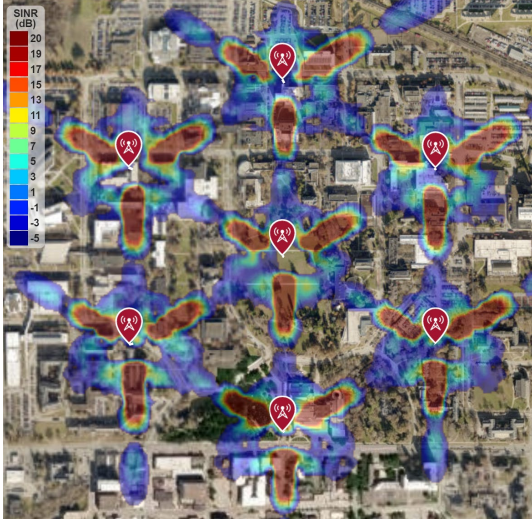
Figure 4.2 A comparison of RF coverage and SINR is depicted for a group of seven cells by varying the number of sectors per cell and equipped with 8-by-8 antenna arrays in each sector.

#### 4.3.2 Improved RF Coverage Employing 16-by-16 Antenna Array in Every Sector

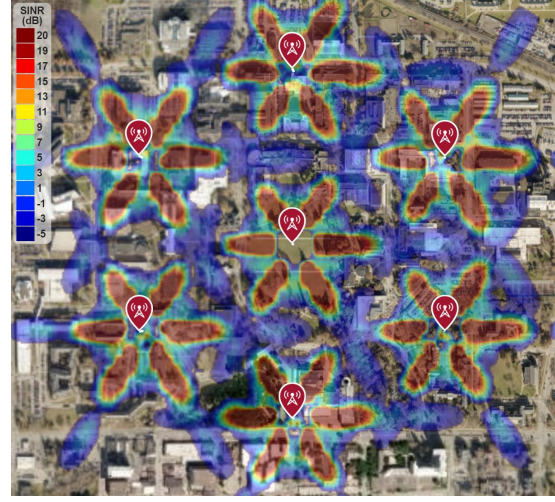
Figure 4.3 provides a comparison of RF coverage and SINR at 70GHz operating frequency, utilizing a 16-by-16 antenna array in each sector, with varying numbers of sectors per cell site.



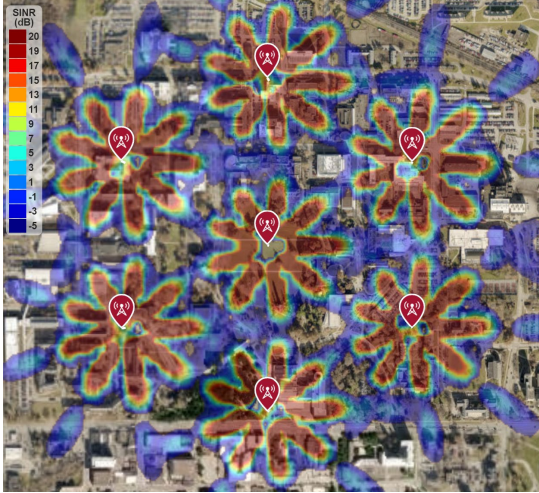
(a) RF coverage with 3 sectors cell



(b) RF Coverage with 6 sectors cell



(c) RF coverage with 9 sectors cell



(d) RF Coverage with 12 sectors cell



Figure 4.3 A comparison of RF coverage and SINR is depicted for a group of seven cells by varying the number of sectors per cell and equipped with 16-by-16 antenna arrays in each sector in contrast to Figure 4.2.

In Figure 4.3(a), the simulation results reveal poor SINR for the conventional cell architecture (with three sectors per cell site), with most of the deployment areas experiencing SINR below 3 dB.

The RF coverage improves when each cell site employs 6 sectors, as demonstrated in Figure 4.3(b). This configuration achieves a good SINR of 20 dB across a significant portion of the deployment area. However, some areas still exhibit poor SINR below 3 dB.

Figure 4.3(c) illustrates a substantial improvement in RF coverage when the number of sectors per cell site increases to 9. This configuration achieves an excellent SINR of 20 dB across the maximum deployment area. However, some areas may still experience SINR below 5 dB.

The most optimal RF coverage is attained when each cell site utilizes 12 sectors, as shown in Figure 4.3(d). This configuration results in excellent SINR of 20 dB throughout the entire deployment area. Therefore, opting for 9 or 12 sectors, instead of the traditional 3 sectors, yields exceptional SINR performance when each cell sector employs a 16-by-16 antenna array.

#### **4.4 Cell Site Power Consumption with Higher-Order Cell-Sectorization**

The individual cell site is one of the main elements that consume the highest power in the cellular network. Studies suggest that the cell site consumes about 60% of the total Radio Area Network (RAN) power [91]. This section describes a power consumption model for the 5G cell site and shows the effect of higher-order cell-sectorization in cell site power consumption.

Based on the traffic conditions, the cell site power consumption can be modeled for the following two scenarios [91, 92]:

- a) Dynamic mode power consumption:** This parameter represents the total power consumption expressed as a function of average offered traffic, as given by Equation (4.1) [91]. The major components of the dynamic power consumption

include maximum transmit power, backhaul power, baseband signal processing unit, transceiver, and power amplifier.

- b) Static/sleeping mode power consumption:** This parameter represents the scenario when traffic load is equal to zero, but some essential components such as baseband processing unit, AC-DC converter, Cooling unit, etc are still active. This parameter is expressed by Equation (4.2) [91].

The total cell site power consumption will be the sum of static and dynamic power for a specific time duration. If we consider the observation time to be  $T_{OH}$ , the total power consumption will be given by Equation (4.3).

$$P_{in} = P_{bh} + P_{cool} + \eta_{sector} \cdot (P_{rect} + P_{bb}) + \eta_{sector} \cdot \alpha \cdot \eta_t \cdot (P_{trx} + \frac{P_{max}}{\eta_{pa} \cdot \sigma_{feed}}) \quad (4.1)$$

$$P_{in-sleep} = N_{TRX} \cdot P_{sleep} \quad (4.2)$$

$$P_{total} = T_{OH} \cdot (P_{in} + P_{in-sleep}) \quad (4.3)$$

Where  $\eta_{sector}$  is the number of sectors per cell,  $P_{trx}$  is the transceiver power consumption,  $P_{max}$  is the maximum radiated power in W,  $\eta_{pa}$  is the power amplifier efficiency,  $\sigma_{feed}$  is the feeder cable loss,  $P_{bh}$  is the backhaul power consumption,  $P_{cool}$  is the cooling system power consumption,  $P_{rect}$  is the power supply power consumption,  $P_{bb}$  is the baseband signal processing power consumption,  $\eta_t$  is the number of transmit antennas,  $\alpha$  is the average traffic load per sector (between 0 and 1), and  $T_{OH}$  is the total observation time.

#### 4.4.1 Dynamic Mode Power Consumption

The 5G network in the higher frequency spectrum will use a larger number of transmitters and receivers (i.e.,  $T_x = 64$ , and  $R_x = 64$ ) to take advantage of massive MIMO.

The simulation results shown in Figure 4.5 and Figure 4.5 uses the parameters listed in Table 4.1 [91, 92].

Table. 4.1 The Parameters for simulating cell site power consumption [91, 92]

Parameters	Value
$P_{bh}$ (Watt)	10
$P_{rect}$ (Watt)	5
$P_{bb}$ (Watt)	3
$P_{cool}$ (Watt)	0
$P_{trx}$ (Watt)	1
$P_{max}$ (Watt)	10
$\eta_{pa}$	0.07
$\eta_t$	1, 2, 3, 4, ..... 64
$\eta_{sector}$	1, 3, 6, 9, and 12
$\sigma_{feed}$	1
$\alpha$	0 or 1

Figure 4.5 presents a comparison of the total power consumption for multi-sector cell sites with varying numbers of transmitters. The results underscore the strong correlation between power consumption and the number of transmitters. Increasing the number of transmitters leads to a corresponding increase in power consumption. For instance, a traditional three-sector cell site consumes 3.487 kW when equipped with eight transmitters per sector. However, power consumption surges to over 27 kW when employing 64 transmitters in each sector, as seen in the context of massive MIMO

technology. Consequently, as the number of transmitters escalates, expanding the number of sectors per cell site results in a significant upswing in overall power consumption. For example, the shift from 3-sector cells, each equipped with 64 transmitters, to 12-sector cells, each also featuring 64 transmitters, would lead to a fourteen-fold increase in power consumption, as depicted in Figure 4.5.

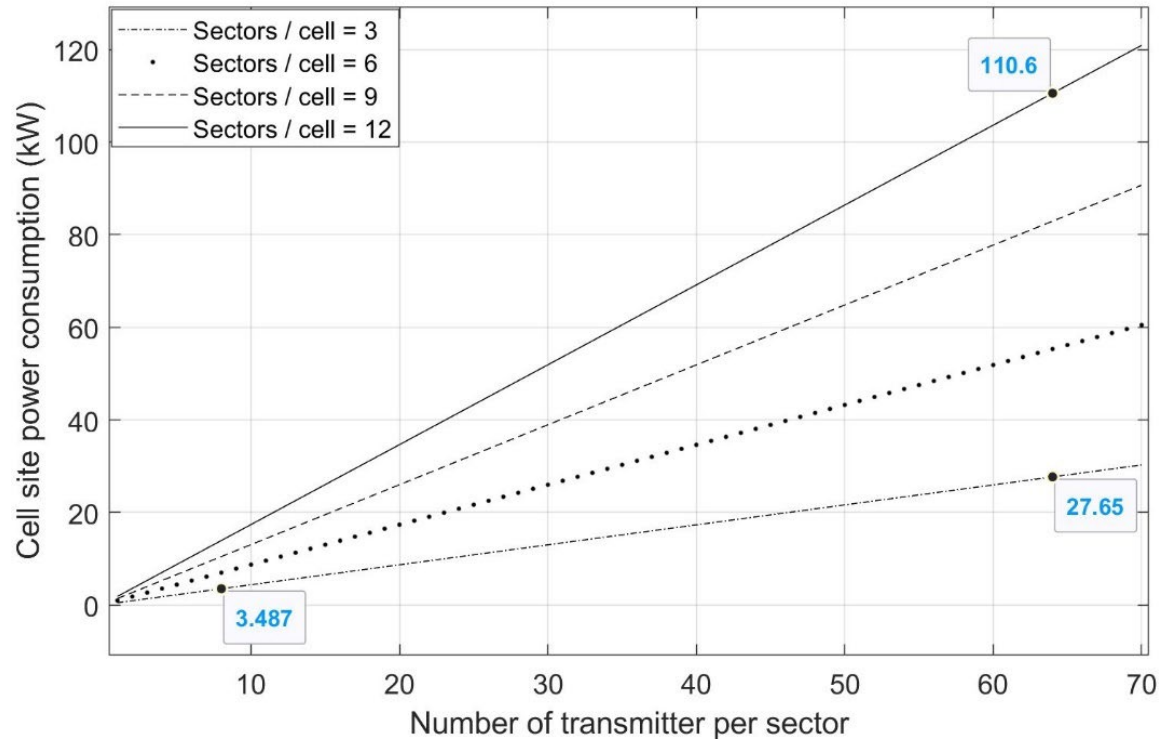


Figure 4.4 The power consumption of a cell site in dynamic mode as function of the number of transmitters per sector, obtained using Equation (4.1) and (4.3), for a cell with 3-sectors, 6-sectors, 9-sectors, and 12-sectors

#### 4.4.2 Sleeping Mode Power Consumption Simulation

Figure 4.6 depicts static power consumption as a function of the number of transmitters per cell. The results highlight that each individual cell site consumes power, even in the absence of traffic, due to the continued operation of essential components such

as the baseband processing unit, AC-DC conversion unit, and cooling unit. Static power consumption exhibits a direct relationship with the number of transmitters in use. For instance, a three-sector cell with 64 transmitters consumes 825.6W, while this consumption rises to 3.3kW when employing a 12-sector cell. Consequently, system designers must carefully determine the optimal number of transmitters and receivers to support massive MIMO without imposing excessive power demands on the cell site.

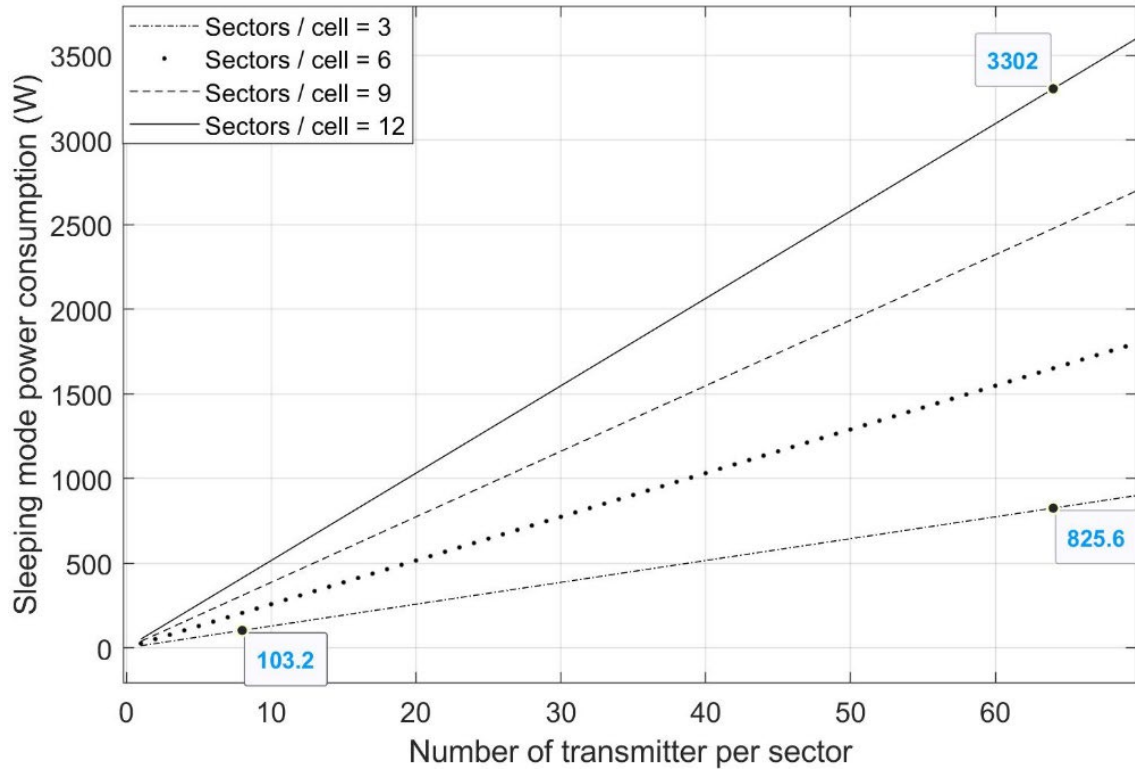


Figure 4.5 The power consumption of a cell site in sleeping mode as function of the number of transmitters per sector, obtained using Equation (4.2) and (4.3), for a cell with 3-sectors, 6-sectors, 9-sectors, and 12-sectors

As discussed in Section 4.3, the evolution of traditional cell site architecture from 3 sectors per cell to 9 or 12 sectors per cell is imperative for maintaining robust RF



coverage in the millimeter-wave spectrum. However, it's important to note that higher-order cell-sectorization, especially when combined with a large number of transmitters per sector, can result in substantial power consumption, both in dynamic mode (as shown in Figure 4.4) and in sleep mode (as shown in Figure 4.5).

Higher-order cell-sectorization, as depicted in Figure 4.2 (d), already achieves robust RF coverage and favorable SINR across the deployment area, obviating the need for an excessive number of transmitters, such as the 64 transmitters per sector. For instance, in a configuration utilizing a three-sector cell with 64 transmitters per cell, the dynamic power consumption soars to 27.65 kW. However, opting for a 12-sector cell with just 8 transmitters per sector significantly reduces dynamic power consumption to 13.92 kW. Despite employing four times the number of sectors in this scenario, the reduction in transmitters per cell yields nearly half the cell site's power consumption. This highlights the role of higher-order cell-sectorization not only in enhancing RF coverage but also in curbing cell site power consumption.

Moreover, it's worth emphasizing that higher-order cell-sectorization provides an optimal solution for striking a balance between RF performance and power efficiency. This approach allows network designers to achieve high-quality coverage without resorting to an excess of transmitters, ensuring efficient resource utilization and cost-effectiveness in millimeter-wave 5G networks.

## **4.5 Adaptive Beamforming and Cell-Sectorization**

### ***4.5.1 Traditional Phased Array Architecture***

Figure 4.6 showcases a phased array antenna configuration composed of eight rectangular microstrip patch antennas. The combined radiation from each of these antenna

elements determines the antenna's radiation pattern and primary beam direction. Importantly, each of these elements is equipped with a Transmit/Receive (T/R) switch and steering circuitry, enabling beam steering capabilities through phase adjustments of the array's individual elements. This represents a notable advantage over traditional linear arrays, which lack this beam steering capability. However, it's important to recognize that when a system necessitates a large number of antenna elements, the associated costs will increase significantly due to the inclusion of these additional circuit elements. Additionally, such a configuration will lead to heightened power requirements for the system.

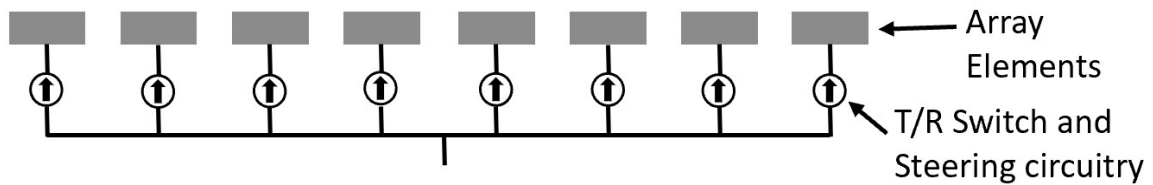


Figure 4.6 An illustration of a phased array antenna structure with eight antenna elements. Each of these elements includes a T/R (Transmit/Receive) switch and steering circuitry

#### 4.5.2 *Phased Array Architecture with Subarrays*

Figure 4.7 illustrates an enhanced phased array configuration comprising two subarrays, each equipped with four rectangular microstrip patch antennas. The total number of antenna elements matches that of Figure 4.6. In this architecture incorporates a single Transmit/Receive (T/R) switch and steering circuitry for every element within the array. However, it preserves the same radiation pattern as the conventional phased array antenna, where the radiation patterns of each subarray constructively interfere in the desired direction. Beam steering is accomplished by modifying the phase of each element within each subarray.

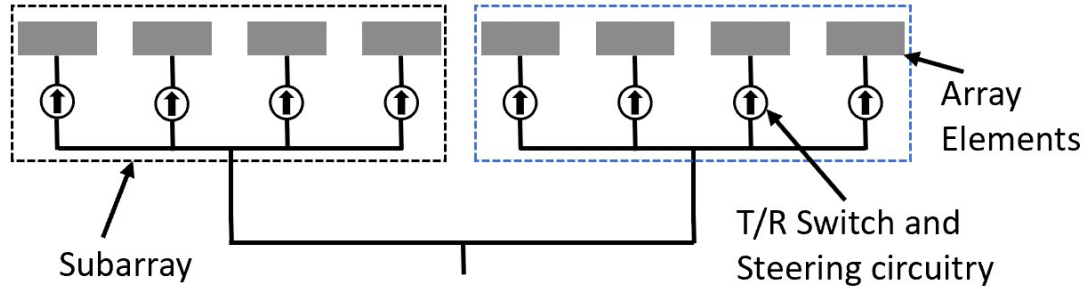


Figure 4.7 A visual representation of a phased array antenna configuration featuring two subarrays, each equipped with four antenna elements. Each of these elements includes a T/R (Transmit/Receive) switch and steering circuitry, in contrast to Figure 4.6

#### 4.5.3 Adaptive Beamforming

Chapter 7 of reference [93] delves into various adaptive beamforming methods. The following section presents one such adaptive beamforming and beam-steering technique facilitated through an improved phased array architecture, as depicted in Figure 4.8. In this setup, the array utilizes two feed networks to regulate the number of elements emitting radiation from each subarray. Feed network-1 is responsible for activating all four elements in each subarray, resulting in a narrow beam radiation pattern. Conversely, Feed network-2 is employed to activate two elements from each subarray, generating a broader beam radiation pattern.

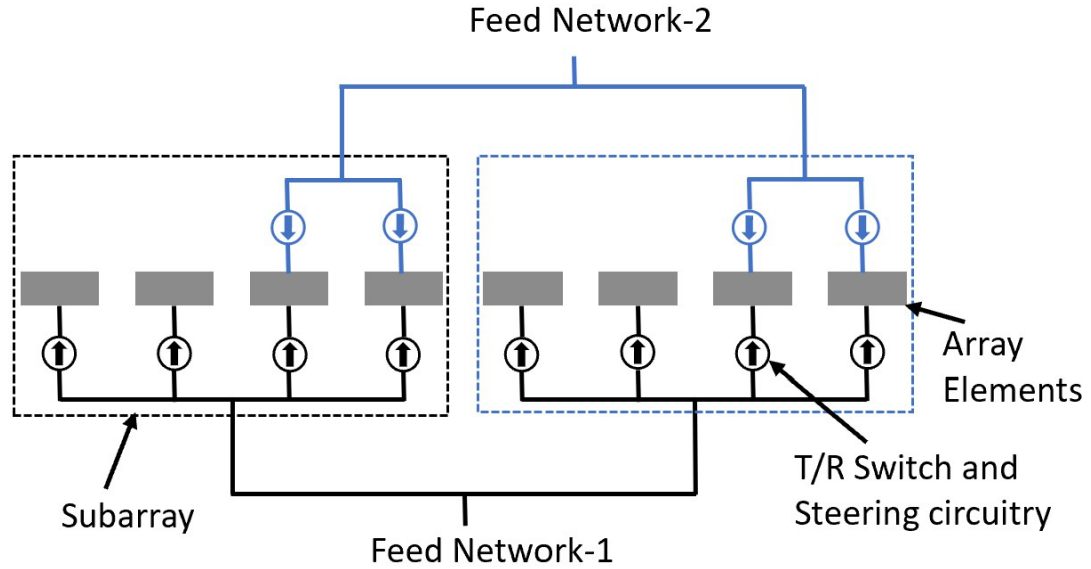


Figure 4.8 A visual representation of a phased array antenna configuration featuring two subarrays with duel feed architecture, each equipped with four antenna elements. Each of these elements includes a T/R (Transmit/Receive) switch and steering circuitry, distinguishing it from the setups depicted in Figures 4.6 and 4.7

To illustrate adaptive beamforming, consider a phased array antenna designed with the architecture described above for a 70 GHz operating frequency. This antenna comprises 16 subarrays, each equipped with 16 antenna elements, and it employs two feed networks to regulate the number of active elements radiated from each subarray. One feed network activates all 16 elements in each subarray, while the second feed network enables 8 out of the 16 elements in each subarray. Figure 4.9 illustrates the normalized power distribution of this array antenna as the number of active antenna elements varies, demonstrating the impact on antenna beamwidth.

The simulation results reveal that the beamwidth is extremely narrow when each subarray incorporates 16 active radiating elements, as depicted in Figure 4.9(a). This

narrow configuration provides maximum directivity. Conversely, the beamwidth becomes wider when the active number of elements per subarray is reduced to 8 as depicted in Figure 4.9(b). As such, the beamwidth can be precisely adjusted by controlling the number of radiating elements within the subarray. This adaptive beamwidth feature is employed in adaptive cell-sectorization, which will be discussed in the following section.

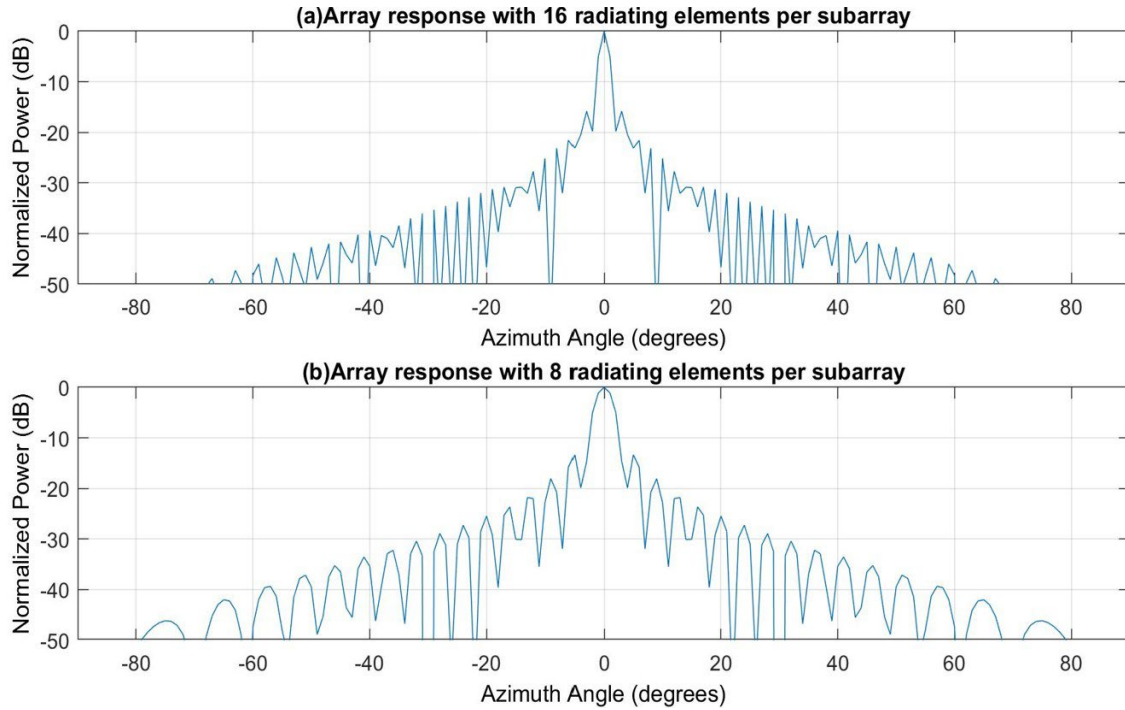


Figure 4.9 A comparison of array responses for a phased array operating at a frequency of 70GHz for different numbers of radiating elements per subarray in contrast to Figure 2.1: (a) array response with 16 radiating elements per subarray, (b) array response with 8 radiating elements per subarray, and (c) array response with 4 radiating elements per subarray

#### 4.5.4 Adaptive Beam Steering

Figure 4.10 depicts simulation outcomes for a phased array antenna comprised of 16 subarrays, each featuring 16 active radiating elements, designed for an operating frequency of 70 GHz. The results provide a comparison of the normalized power

distribution of the array with and without beam steering. Beam steering of twenty degrees is accomplished by adjusting the phase of each element within every subarray by 20 degrees, and the phase of each subarray also shifts by 20 degrees toward the broadsides. Given its electronic controllability, beam steering holds promise for applications in adaptive cell-sectorization, as elaborated upon in the subsequent section.

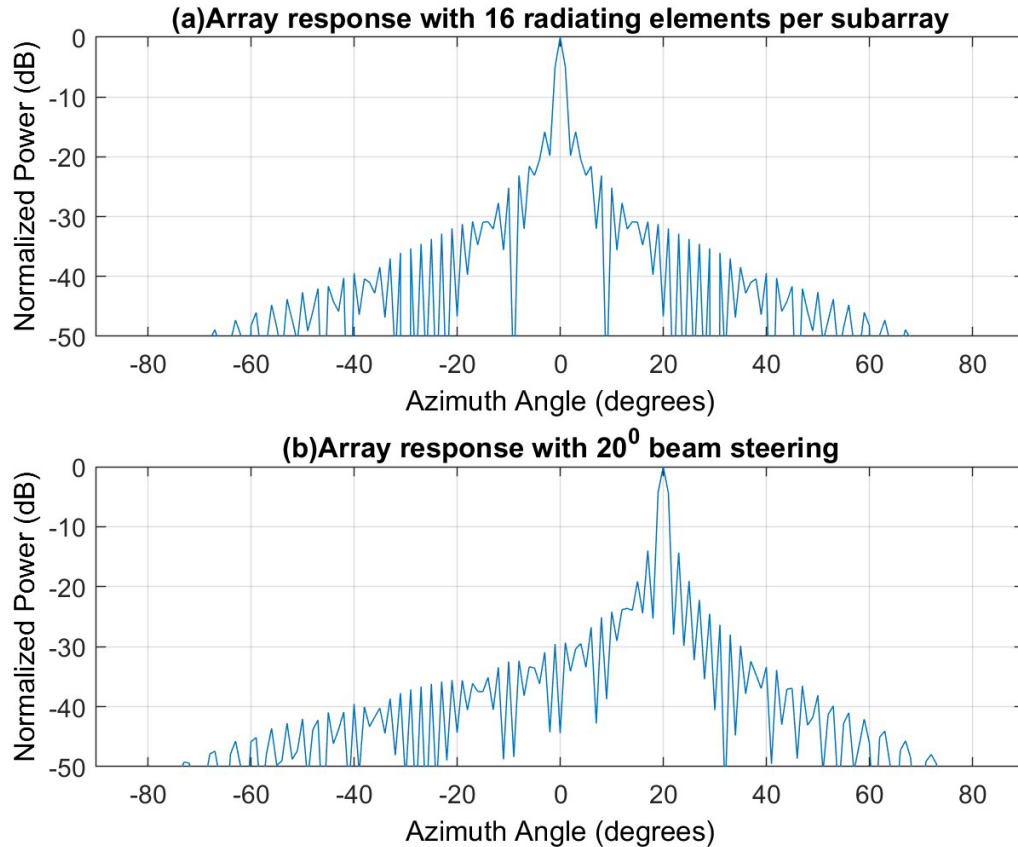


Figure 4.10 An array response comparison for a 70GHz phased array for different beam steering configurations, as compared to Figure 4.9: (a) array response with no beam steering using 16 radiating elements per subarray, and (b) array response with 20° beam steering using 16 radiating elements per subarray

#### 4.5.5 Proposed Adaptive Cell-Sectorization to Save Energy

The cellular network is dimensioned to support maximum traffic during the peak hours (i.e., maximum traffic). But, the traffic demand significantly varies throughout the day. Significant radio resources (e.g., baseband signal processing unit, backhaul, transceiver, amplifier, etc) remain unused much of the time causing unnecessary power consumption. Figure 4.4 demonstrates that power consumption is maximized for higher-order cell-sectorization when a large number of transmitters per sector are used.

This section proposes an adaptive cell-sectorization method, where higher-order cell-sectorization (e.g., 12 sectors per cell) is employed to support peak traffic and lower-order cell-sectorization is utilized for off-peak traffic. Since the number of active sectors varies with traffic demand, all unused radio resources (e.g., active transceiver, amplifier, etc.) will revert to idle mode to conserve energy. The advanced antenna array and adaptive beamforming method are used for adaptive cell-sectorization, sectorization, as described in the previous section. If  $T_{OH}$  is the total observation time, the total cell site power consumption for the standard cell-sectorization technique is calculated by Equation (4.3). To appreciate how the proposed solution could be employed in a practical scenario, assume an observation time is 24 hours with 16 hours ( $T_{OH}$ ) experiences variable traffic loading, and 8 hours with zero traffic. In this case, the following three scenarios are viable solutions to employ adaptive cell-sectorization:

**a) Scenario 1**

All twelve sectors remain active to support high traffic times (e.g.,  $T_{12} = 8$  hours), and nine sectors (e.g.,  $T_9 = 8$  hours) are used to support periods with low traffic. This solution is accomplished according to the following three steps:

**Step 1.** Turn off sectors 2, 6, and 10.

**Step 2.** Apply adaptive beam steering to sectors 1, 3, 4, 5, 7, 8, 9, 11, 12 in such a way that sector 1 is centered at  $0^0$ , sector 3 at  $40^0$ , sector 4 at  $80^0$ , sector 5 at  $120^0$ , sector 7 at  $160^0$ , sector 8 at  $200^0$ , sector 9 at  $240^0$ , sector 11 at  $280^0$ , and sector 12 at  $320^0$ , respectively.

**Step 3.** Apply adaptive beamforming with sectors 1, 3, 4, 5, 7, 8, 9, 11, and 12 to reduce RF coverage gaps.

**b) Scenario 2:**

All twelve sectors remain active to support high traffic times (e.g.,  $T_{12} = 8$  hours), and six sectors (e.g.,  $T_6 = 8$  hours) are used to support periods with low traffic. This solution is accomplished according to the following three steps:

**Step 1.** Turn off sectors 2, 4, 6, 8, 10, and 12.

**Step 2.** Apply adaptive beam steering to sectors 1, 3, 5, 7, 9, and 11 in such a way that sector 1 is centered at  $0^0$ , sector 3 at  $60^0$ , sector 5 at  $120^0$ , sector 7 at  $180^0$ , sector 9 at  $240^0$ , sector 11 at  $300^0$ , respectively.

**Step 3.** Apply adaptive beamforming with sectors 1, 3, 5, 7, 9, and 11 to reduce RF coverage gaps.

**c) Scenario 3:**

All twelve sectors remain active to support high traffic times (e.g.,  $T_{12} = 8$  hours), nine sectors (e.g.,  $T_9 = 4$  hours) are used to support periods of moderate traffic, and six sectors (e.g.,  $T_6 = 4$  hours) are used when traffic demand is very low.

The energy consumption gain for adaptive cell-sectorization is given by Equation (4.4):



$$ECG_{adaptive} = \frac{P_{in12} \cdot T_{OH}}{\sum_{i=12,9,6} (P_{ini} \cdot T_i)} \quad (4.4)$$

Where  $P_{in}$  is the cell power consumption for any sectors (e.g.,  $P_{in12}$  for 12 sectors cell),  $T_{OH}$  is the variable traffic observation time, and  $T_i$  is the observation time for any sectors.

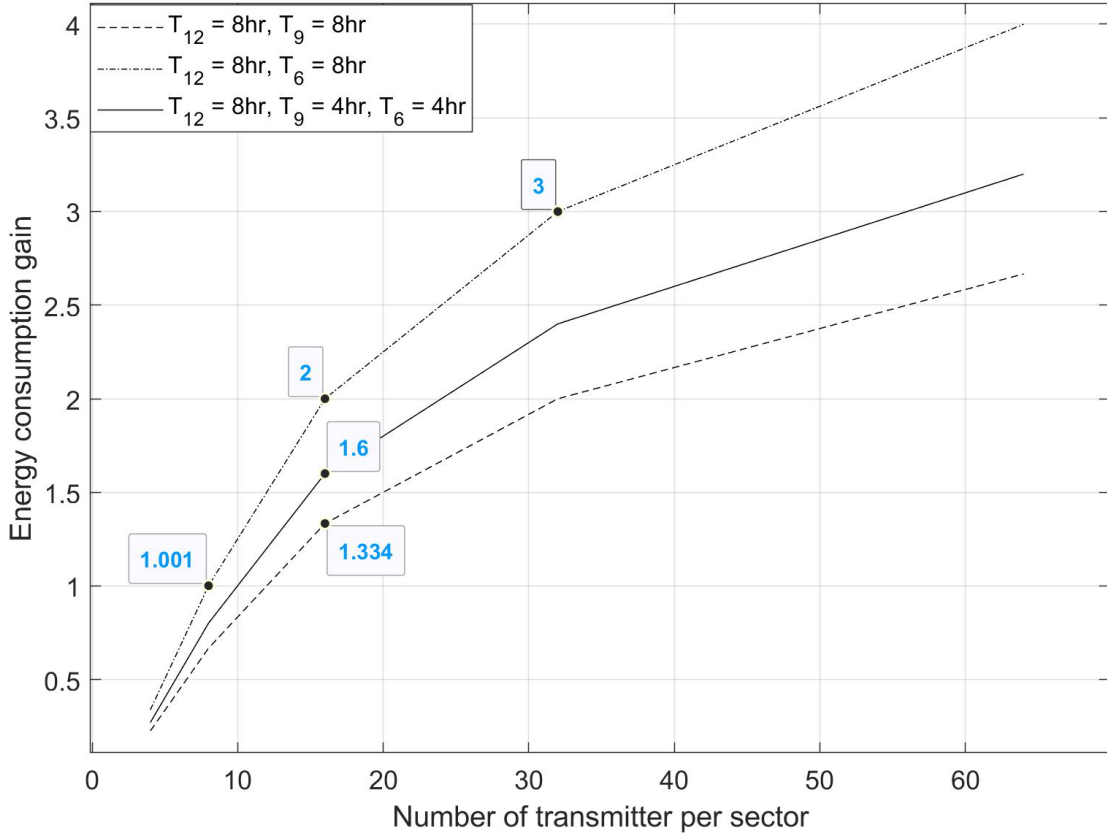


Figure 4.11 A comparison of cell site energy consumption gain as a function of the number of transmitters per sector for various numbers of active sectors and 16 hours of observation time: (scenario 1) twelve sectors active for 8 hours and nine sectors active for the remaining 8 hours, (scenario 2) twelve sectors active for 8 hours and six sectors active for the remaining 8 hours, and (scenario 3) twelve sectors active for 8 hours, nine sectors active for 4 hours, and six sectors active for the remaining 4 hours

Figure 4.11 shows the Energy Consumption Gain (ECG) versus the number of transmitters per sector simulation for three adaptive cell-sectorization scenarios. The simulation results show that the ECG gain is maximized when six sectors are utilized to support off-peak traffic when compared with nine sectors. Since six sectors employ a smaller number of transmitters than nine or twelve sectors, energy savings will be maximized when only six sectors are employed for the maximum amount of time. To provide an example, let's consider the ECG (Energy Consumption Gain) when using twelve sectors to accommodate high-traffic conditions and nine sectors to accommodate moderate traffic, with each sector equipped with 16 transmitters. In this scenario, the ECG gain is 1.33. However, if we maintain twelve sectors for high-traffic conditions while reducing the number of sectors to six for moderate traffic, while still using the same number of transmitters per sector, the ECG gain increases to 2

In conclusion, adaptive cell-sectorization presents energy-saving advantages when compared to a fixed-sector cell approach. Nevertheless, it may introduce an RF coverage gap, particularly when non-steerable antennas are employed in each sector. To enhance system performance and address this RF coverage gap, an advanced phased array antenna system with adaptive beamforming is recommended. Adaptive beamforming facilitates adjustments to antenna beamwidth and radiation direction, as explained in the previous section. This antenna system is proposed to eliminate RF coverage gaps when a reduced number of sectors are active

## CHAPTER 5

### RF COVERAGE ANALYSIS FOR NON-LINE-OF-SIGHT LOCATION

#### 5.1 Introduction

Because of the extremely short wavelength, the millimeter-wave spectrum is susceptible to multipath signals caused by phenomena like reflection, diffraction, and scattering. These multipath signals can lead to a reduction in the received signal level at the receiver. However, the impact of multipath signals can vary significantly depending on the types of objects present in the vicinity of a cell site, including buildings, vehicles, streetlights, lampposts, foliage, and more. The effect is particularly pronounced when users do not have a direct line-of-sight communication link with the cell site. Therefore, this section is dedicated to demonstrating RF coverage simulation and analyzing received signals in non-line-of-sight scenarios.



Figure 5.1 Visualize Buildings Data of Chicago downtown, IL, USA

For the RF coverage simulation, Chicago downtown, IL, USA is used as the deployment area. Figure 5.1 shows the deployment area map collected from the OpenStreetMap [83]. It has building information (e.g., building materials, glass, or concrete) needed for the multipath simulation. All the simulation parameters are listed in Table 5.1. The following two scenarios are considered for the simulation:

- a) User at non-line-of-sight with one reflected path (i.e. single ray analysis)
- b) User at non-line-of-sight with two reflected paths (i.e. two ray analysis)

Table. 5.1 The parameters for simulating a 5G cell for analyzing non-line-of-sight signals

Parameters	Values
Operating Frequency	70 GHz
Bandwidth	80 MHz
BS Antenna height	25 m
BS Transmit power	40 dBm
BS Antenna gain	10 dBi
BS Antenna noise figure	7 dB
Receiver height	1.5 m
Receiver noise figure	7 dB
Receiver gain	8 dBi
BS Antenna downtilt angles	15 <sup>0</sup>
Cell site radius	100 m
No. of cell sites	1
No. of sectors per cell	3
Cell sector angles	30 <sup>0</sup> , 150 <sup>0</sup> , and 270 <sup>0</sup>
Array size for each transmitter	256 elements

## 5.2 User at Non-Line-of-Sight with One Reflected Path

The simulation results shown in Figures 5.2 to 5.11 uses free space propagation modeling to estimate the received signal level and compare the results after including all the weather impairments (e.g., rain, fog) (discussed in chapter 3). Figure 5.2 shows the RF coverage simulation and receive signal strength for 70 GHz operating frequency. The user doesn't have a direct communication link with the cell site, but one reflected signal arrives at the receiver after reflecting from a building wall.

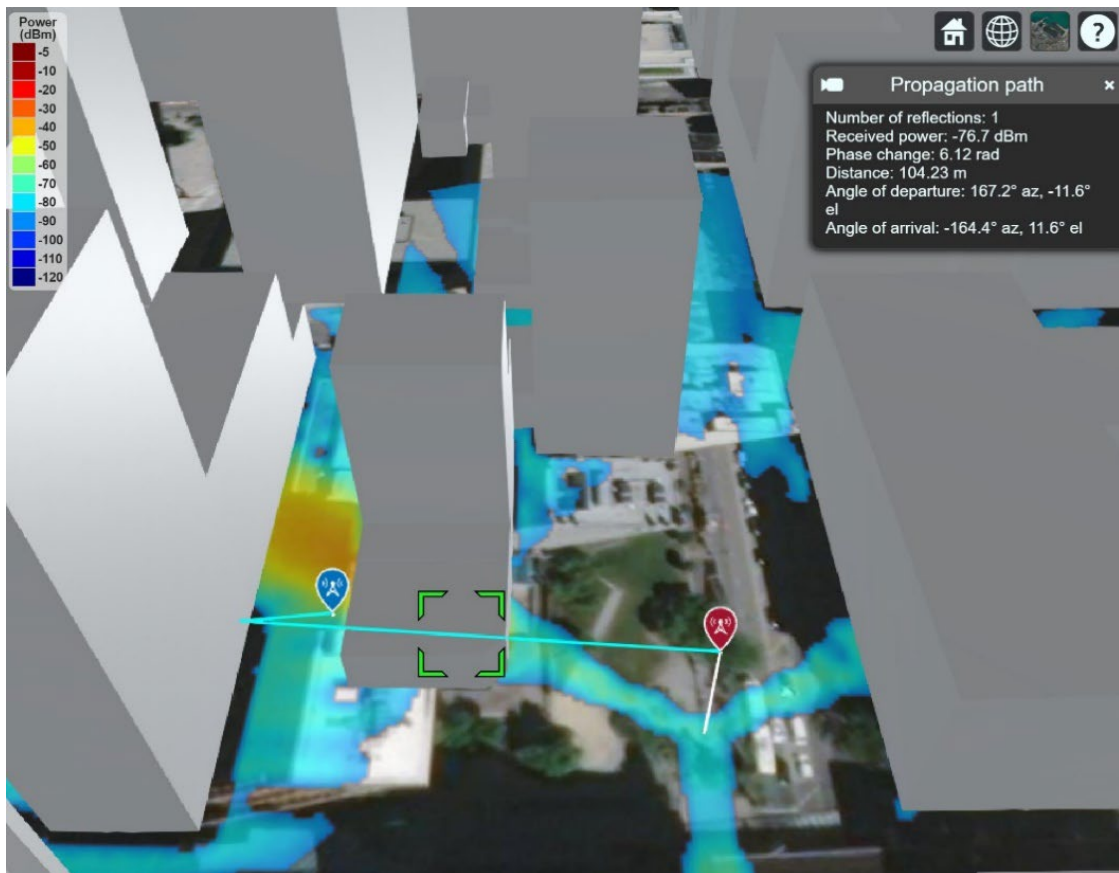


Figure 5.2 Radio frequency coverage of a 5G cell and ray tracing involving a single reflected path.

However, the reflected signal characteristic can significantly vary with the properties of the reflecting surface (e.g., perfect conductor, glass, concrete, and brick, etc.), which will change the received signal level at the receiver. Four simulation results are shown in Table 5.2 with different building materials type (i.e., perfect conductor, glass, concrete, and brick) to compare the effect of the received signal level. Results show that the received signal level varies significantly with the building materials type (e.g., perfect conductor, glass, concrete, brick, etc.). The maximum received signal obtained is - 76.7 dBm when the building material is an ideal conductor. But the received signal level drops to - 84.0 dBm for the glass type materials, - 84.8 dBm for the concretes, and -86.6 dBm for the brick. For the worst-case scenario (i.e., brick building materials), if we consider the weather loss (e.g., rain and fog), the received signal level drops further to -88.7 dBm, which is not a good signal for the 5G network.

Table. 5.2 Relationship between received signal power involving one reflected path and types of building materials

<b>Building Material Type</b>	<b>Receive Signal power</b>
<b>Perfect reflector</b>	- 76.7 dBm
<b>Glass</b>	- 84.0 dBm
<b>Concrete</b>	- 84.8 dBm
<b>Brick</b>	- 86.6 dBm

### 5.3 User at non-line-of-sight with two reflected paths

Figure 5.3 shows the RF coverage simulation and receive signal strength with two reflected paths. Three simulation results with different building materials are listed in Table 5.3. The findings show that the received signal power improved by 3.4 dB compared to

one reflected path when the building material is a perfect conductor. However, the received signal drops by 1.4 dB if the material is concrete, and 1.7 dB for brick, respectively. Since the multipath signal arrives at the receiver through a different path, they arrive with different amplitude, path delay, and phases. Therefore, the reflected path can interfere constructively or destructively. For the concrete and brick, the reflected path signal interferes destructively, and the received signal experiences signal attenuation. Even with the two reflected paths, the received signal power is not good enough for the 5G network. The next section describes how to improve the received signal level by adaptive beam steering.

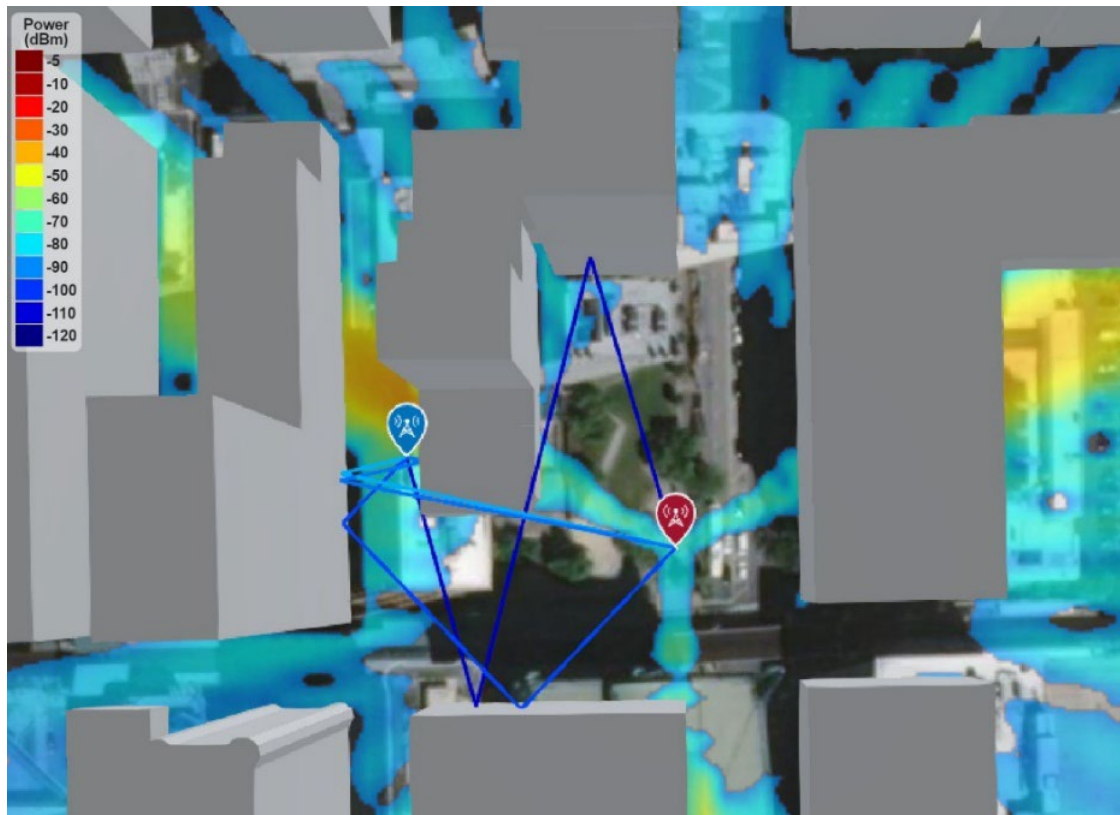


Figure 5.3 Radio frequency coverage of a 5G cell and ray tracing involving two reflected paths in contrast to Figure 5.2

Table. 5.3 Building Relationship between received signal power involving two reflected paths and types of building materials in contrast to Table 5.2

<b>Building Material Type</b>	<b>Receive Signal power with two reflected paths</b>	<b>Receive Signal power with one reflected path</b>
Perfect reflector	- 73.3 dBm	- 76.7 dBm
Concrete	- 86.2 dBm	- 84.8 dBm
Brick	- 88.3 dBm	- 86.6 dBm

#### 5.4 Adaptive Beam Steering to Enhance the Received signal Power

Phased array antenna provides adaptive beam steering, which can steer the radiated beam in any desired direction, described in Chapter 2. Figure 5.4 shows the updated RF coverage and receive signal strength simulation results after  $15^0$  beam steering of sector 1. All the simulation parameters remain the same as Table 5.1 except sector 1 steer to  $45^0$  instead of  $30^0$ .

Four simulation results are shown in Table 5.4 for different building materials to compare the received signal strength with and without beam steering. Results show that the received signal improves by more than 30 dB for all four building materials. The weather loss might drop the received signal level by a few dB but, the received signal is perfect for all four building materials types. For example, the receive signal power is -57 dBm for brick-type building materials after adding the weather loss (i.e., rain and fog), which is still an excellent signal for the 5G network.



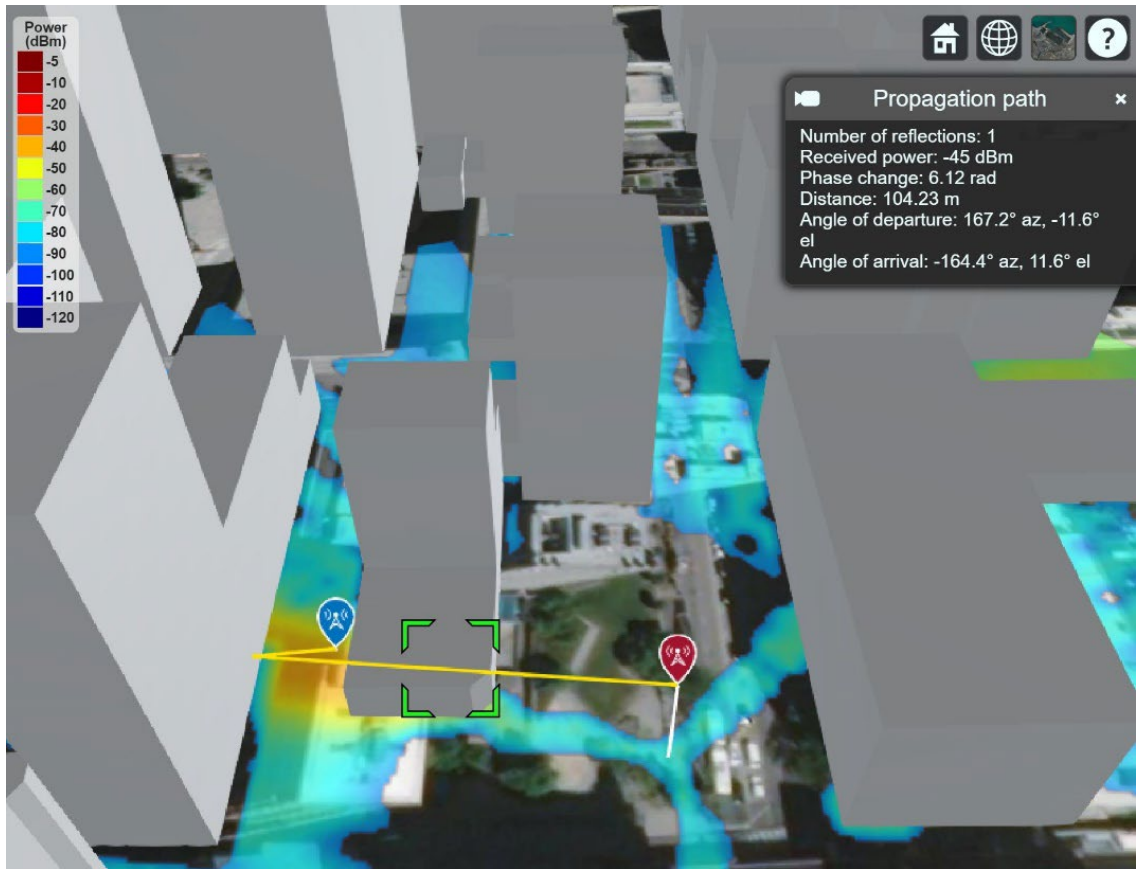


Figure 5.4 Radio frequency coverage of a 5G cell and ray tracing involving a single reflected path after beam steering in contrast to Figure 5.3

Table. 5.4 Relationship between received signal power involving one reflected path and types of building materials after beam steering in contrast to Table 5.2

<b>Building Material Types</b>	<b>Receive Signal power with beam steering</b>	<b>Receive Signal power without beam steering</b>
<b>Perfect reflector</b>	- 45 dBm	- 76.7 dBm
<b>Glass</b>	- 52.3 dBm	- 84.0 dBm
<b>Concrete</b>	- 53 dBm	- 84.8 dBm
<b>Brick</b>	- 55 dBm	- 86.6 dBm

Figure 5.5 shows the updated RF coverage and signal strength simulation results with two reflected paths after the 15 degree of beam steering at sector 1. Three simulation results with different building materials are listed in Table 5.5. Results show that the received signal power improved by 1.6 dB compared to one reflected path when the building material is a perfect conductor. However, the received signal drops by 1.88 dB if the material is concrete and 1.84 dB for brick. The receive signal power is still in the excellent range which is required for the 5G network.



Figure 5.5 Radio frequency coverage of a 5G cell and ray tracing involving two reflected paths after beam steering in contrast to Figure 5.3.

Table. 5.5 Relationship between received signal power involving two reflected path and types of building materials after beam steering in contrast to Table 5.3

<b>Building Material Types</b>	<b>Receive Signal power with two reflected paths</b>	<b>Receive Signal power with one reflected path</b>
<b>Perfect reflector</b>	- 43.364 dBm	- 45 dBm
<b>Concrete</b>	- 54.88 dBm	- 53 dBm
<b>Brick</b>	- 56.84 dBm	- 55 dBm

The millimeter-wave spectrum has a very short wavelength (i.e., 1mm-10mm). So, the 5G signal will be reflected from most objects (e.g., small wall, vehicles, buildings, trees, lamp post, signals, etc.) in the outdoor environment which will cause multipath signals. Based on the above simulation results (Figure 5.2 to 5.5), it is clear that the multipath signals greatly impact the millimeter-wave signal. It is also found that the received signal level significantly varies with different multipath signals when the transmitter transmits in one angle versus the other. Therefore, the received signal level will vary substantially with varying deployment areas and the cell site locations. The system designer must analyze the multipath signals throughout the deployment area. If there are significant signal drops in a particular area due to non-line-of-sight, the adaptive beam steering can be used to improve the received signal level.

## **CHAPTER 6**

### **5G NETWORK DEPLOYMENT CHALLENGES AND GUIDELINES**

#### **6.1 Introduction 5G Network Deployment Challenges**

Planning and deploying a new cell site involves several intricate steps, encompassing tasks such as surveys, planning, civil and electrical architecture, infrastructure development, signal testing, and more [94]. According to the CEO of Crown Castle, a prominent telecommunications infrastructure provider, the current timeframe for deploying 5G cells spans between 18 to 24 months [91]. Given the necessity for Mobile Network Operators (MNOs) to establish a substantial number of new cell sites to offer 5G services, adherence to conventional deployment procedures may impede the rapid rollout of the 5G network. This section outlines the potential challenges associated with 5G network deployment and presents guidelines for surmounting these challenges, thereby facilitating the accelerated deployment of the 5G network.

#### **6.2 Accurate Cell Site Planning**

During the initial phases of 5G network deployment, all existing cell sites, which were originally designated for 3G/4G networks, will serve as potential locations for 5G infrastructure [94]. However, it is important to note that the coverage provided by cell sites diminishes considerably in higher-frequency bands, reducing to a radius of just 200 meters compared to several kilometers in 4G networks. Consequently, the success of 5G networks hinges on cell densification, a crucial strategy to meet the stringent availability requirements, such as the need for 99.99% availability. In essence, network operators will need to deploy hundreds of new 5G cells in contrast to a single 4G cell site. However, the

availability of suitable locations and the need to supply power to those locations will limit options for viable new cell site placements. Hence, precise cell site planning emerges as a significant challenge, essential for minimizing redundant sites, mitigating out-of-cell interference, and curtailing deployment costs.

Furthermore, Mobile Network Operators (MNOs) will need to adopt diverse cell architectures, such as nine sectors and 12 sectors per cell, contingent upon the availability of neighboring cells and the characteristics of the deployment area (e.g., urban or densely urban). This dissertation underscores that advanced antenna designs, incorporating various antenna parameters like antenna height, transmit power, adaptive beamwidth, and adaptive beam steering, present a viable solution for achieving superior RF coverage and enhancing the requisite Signal-to-Interference-plus-Noise Ratio (SINR).

### **6.3 Acquiring Cell Site Location**

With the imperative need to deploy hundreds of new 5G cells, Mobile Network Operators (MNOs) face the considerable challenge of identifying suitable locations and securing these sites for deployment. The acquisition of these new 5G cell site locations will result in a significant escalation of both the initial deployment costs and ongoing operational expenses [95, 96].

In contrast to previous generations, 5G cells do not necessitate tall or robust structures; these cells can be deployed within existing structures, such as the perimeters of buildings or lampposts along roads, among other possibilities. However, each city has its own set of regulations pertaining to the construction of new structures in specific areas. Furthermore, various regions may have distinct local government ordinances that limit the utilization of existing infrastructure or the construction of new infrastructure within their

jurisdiction [97]. Consequently, identifying suitable locations for 5G cell sites is just one aspect of the challenge; the legal complexities associated with acquiring these sites, whether from private property owners or local governments, present a substantial hurdle.

Moreover, the proliferation of multiple mobile operators in countries worldwide aiming to develop their own 5G networks to cover the same deployment area raises the concern that 5G cell towers could saturate urban landscapes. This scenario poses a new dilemma for local governments and municipalities. Given the involvement of diverse stakeholders (MNOs, private property owners, local and national governments, etc.) throughout the deployment process, the establishment of appropriate regulations and frameworks becomes imperative. Some essential guidelines are outlined below:

1. Local and national governments must establish comprehensive guidelines that enable Mobile Network Operators (MNOs) to utilize and collaboratively share existing infrastructure for the deployment of new cell sites.
2. To expedite the process of approving new cell site locations, the government should implement streamlined rules and defined timelines that all involved parties must adhere to, thus mitigating unnecessary delays.
3. Government agencies should offer explicit clarity regarding the fees associated with the establishment of a new cell site or the renewal of an existing one.
4. Local government authorities should provide transparent guidelines to private property owners concerning rental valuations, thereby preventing the imposition of excessive rental costs.

5. Government to should enable multi-operator arrangements with shared resource utilizations to avert exorbitant expenses for operators and ensure efficient resource allocation.

#### **6.4 Propagation Modeling and Coverage Prediction**

Propagation modeling and coverage prediction are invaluable tools that permit the analysis of radio signals before the actual deployment and testing of cell sites. This approach not only translates into significant time and cost savings for Mobile Network Operators (MNOs) but also facilitates the identification of suitable locations for future cell sites without the need for physical deployments. However, traditional empirical propagation models like the Okumura-Hata model, which are effective for 4G networks, are not applicable to the millimeter-wave spectrum [11, 19].

While various research endeavors have addressed 5G propagation modeling [69, 98, 99], a standardized propagation model for 5G networks has yet to be established, preventing the comprehensive analysis of real radio signals before cell site deployment. Nonetheless, this dissertation overcomes this challenge by conducting real-world 5G network coverage analysis using MATLAB and Google Map tools in conjunction with free space propagation modeling. The results presented herein closely approximate real-world deployment conditions, provided an accurate and up-to-date Google Map dataset is utilized.

#### **6.5 Challenges Raised by Advanced Antenna System**

Conventional network planning, designed around multiple sectors per site employing transmitters with wide radiation beams, falls short in meeting the stringent demands of Massive MIMO in areas such as planning, coverage prediction, data rates, and

capacity [94]. To facilitate the implementation of Massive MIMO, the deployment of highly directional antennas with narrow beamwidth becomes imperative, driving the adoption of the Advanced Antenna System (AAS) within the 5G network framework.

The AAS amalgamates advanced array antennas with cutting-edge functionalities, including adaptive beamforming and steerability. Employing a large array of antenna elements (e.g., 16 by 16 array), the AAS delivers high gain and an exceptionally directional radiation pattern with adaptive beam steering. Consequently, it empowers the realization of Massive MIMO (Multiple-Input and Multiple-Output) through recent technological advancements, positioning itself as a pivotal enabling technology for the 5G network. This transformative system enhances network capacity, elevates data rates, bolsters network reliability, improves energy efficiency, and mitigates interferences [94, 100, 101]. While the higher frequency spectrum introduces challenges related to propagation loss, the advanced antenna system rises to meet the demanding RF coverage requirements. However, several key challenges necessitate attention and resolution as a prerequisite:

- The cost-effectiveness of first-generation Massive MIMO deployments will be pivotal, making the selection of an AAS configuration that optimizes network performance while remaining budget-friendly a significant challenge. Achieving this balance will necessitate a deeper understanding of multi-antenna systems and AAS characteristics.
- Given the physical constraints and load-bearing limits of each cell site, careful consideration must be given to the size and weight of the AAS when planning deployments.



- Future-proofing of all cell sites is essential, and MNOs must retain complete flexibility in transitioning to new AAS systems. Physical limitations, such as space availability and load-bearing capacity, can restrict the upgrading options available to MNOs, encompassing additions like increasing sectors, expanding transceiver units for Massive MIMO, or incorporating a multiband antenna system.
- The characteristics of AAS, including factors like beamwidth, gain, and directivity, exhibit substantial variability dependent on operating frequency and the number of elements in the array. For example, sub-6 GHz frequencies result in wider antenna beamwidth, while millimeter-wave spectrums offer highly directional capabilities. Transitioning an AAS from a three-sector cell operating in sub-6 GHz to one operating in the millimeter-wave spectrum can introduce coverage challenges, posing a significant hurdle for MNOs in determining the most suitable AAS and cell site architecture for various deployment scenarios.

However, addressing and surmounting the implementation challenges for efficient massive MIMO deployment will require further comprehensive investigation. Here are some guiding principles to consider:

- Mobile Network Operators (MNOs) must engage in extensive studies encompassing diverse deployment scenarios, featuring varying Advanced Antenna System (AAS) configurations and operating frequencies, to identify the most suitable AAS for each deployment area.
- The industry should actively innovate and adopt cutting-edge technologies aimed at managing AAS size, weight, and wind load characteristics, ensuring practical feasibility in diverse deployment environments.

- A mere transition of the antenna system for each transmitter to an AAS will be insufficient. MNOs should explore updated cell architectures, such as embracing higher-order cell-sectorization (e.g., transitioning from three-sector cells to 6, 9, or 12 sectors per cell), to mitigate coverage gaps, especially in higher-frequency spectrums.

## **6.6 Automatic cell planning**

Considering the necessity of deploying a substantial quantity of 5G cells in each city, the utilization of automatic cell planning tools emerges as a crucial element in expediting the rollout of 5G networks while conserving time and resources. The challenge lies in effectively amalgamating a multitude of cells and employing them uniformly for coverage and capacity analysis. A practical approach involves the creation of several cell groups, each comprising a distinct number of cells—such as seven cells or 19 cells per group, as exemplified in this dissertation. Furthermore, these cell groups can be finely tailored with varying cell site parameters, including antenna array dimensions, sector count, antenna height, azimuth, downtilt angle, and transmit power. This tailored approach allows for the precise analysis of network coverage or capacity planning, with the choice of specific groups contingent upon the characteristics and dimensions of the deployment area.

## **6.7 Energy Efficiency**

The proliferation of ultra-dense 5G cell deployments is poised to assume a pivotal role within 5G wireless networks, addressing the escalating mobile traffic demands and alleviating congested 4G macro-cell traffic to augment user experience quality. However, in the realm of 5G networks, power consumption can assume considerable proportions,

primarily due to the extensive deployment of 5G cells and the less-than-efficient millimeter-wave power amplifiers [102]. In fact, it's estimated that approximately 4.4 terawatt-hours (TWh) of power were consumed by around 100 million 5G cells in 2020, and projections suggest that the overall power consumption in the Information and Communication Technology (ICT) sector could soar to as much as 1700 TWh by 2030 [103, 104]. This compelling scenario underscores the research community's dedication to green communications, seeking energy-efficient solutions for 5G networks with a lofty aim of slashing energy consumption by up to 90% [105, 106].

The power consumption of a cell site manifests in varying traffic conditions, encompassing dynamic power consumption during active periods and static power consumption during idle intervals, as elucidated in Chapter 5. With the advent of advanced antenna systems and the transition to higher-order cell-sectorization from the conventional three-sector cell, the power demands per cell site are poised for a significant escalation. In light of these challenges, several guidelines merit attention:

1. A comprehensive optimization of energy efficiency should be undertaken for all network-related equipment.
2. The development of an advanced control unit is imperative to curtail static power consumption during traffic lulls.
3. Exploring alternative power sources, such as solar cells or batteries, is essential to meet augmented power requirements.

## **6.8 Backhaul Network**

The deployment of dense 5G cells is poised to usher in a remarkable surge in network capacity and data rates [107]. However, this proliferation mandates that each cell site

establishes a direct connection with the core network, often referred to as the backhaul network. The notion of creating a one-hop direct connection, be it wired or wireless, from the core network to every 5G cell site is logistically implausible. Consequently, the only viable approach to ensure a seamless backhaul connection between the core and 5G cells is via a multi-hop network. Yet, it's essential to acknowledge that as the number of hops between the core and 5G cells increases, network latency becomes a growing concern. Thus, crafting an ultra-reliable, ultra-low latency backhaul network emerges as a novel challenge [108, 109].

Addressing these challenges warrants the following guidelines:

1. Mobile Network Operators (MNOs) should explore alternative wireless backhaul solutions capable of supporting high capacity while maintaining cost-efficiency. Wireless backhaul technologies, including Millimeter-wave and laser backhaul [110-113], present viable options to expedite 5G network deployment.
2. MNOs must devise new backhaul architectures that facilitate multi-hop communication while ensuring a seamless backhaul connection that adheres to latency requirements.
3. It is imperative that all backhaul-related equipment exhibits a high degree of energy efficiency, as inefficient components can substantially elevate total energy consumption. Chapter 5 underscores that backhaul components constitute a significant contributor to cell site static power consumption. Therefore, MNOs should employ advanced control units to mitigate static power consumption during periods of zero traffic load.

## **6.9 Separate cell-site for indoor and outdoor coverage**

At higher frequencies, building penetration loss becomes a significant challenge, necessitating the deployment of distinct 5G cells for indoor and outdoor coverage by mobile network operators. Nonetheless, the extent of penetration loss is highly contingent upon the specific building materials and the surrounding environment [114, 115]. Consequently, it is imperative for mobile network operators to conduct comprehensive interference analyses, encompassing issues such as out-of-cell interference, to address potential challenges arising from interactions between outdoor and indoor cells.

## **6.10 Cell site monitoring and signal testing**

Given the sheer magnitude of 5G cell deployments, individually monitoring each cell site would entail substantial costs for mobile operators. Meeting the exacting demands of 5G networks, such as ultra-low latency and ultra-high reliability, necessitates more frequent signal testing compared to existing network protocols. The conventional signal testing method, which typically involves drive testing within the service area, would demand additional human resources and time, resulting in a considerable escalation of testing expenditures. Consequently, network operators must seek alternative solutions for efficient cell site testing and monitoring to optimize both time and costs.

## CHAPTER 7

### CONCLUSIONS AND FUTURE WORK

#### 7.1 Conclusions

The escalating demands for data traffic are compelling cellular networks to explore higher frequency spectrums like millimeter-wave and terahertz to access broader bandwidths. With the 5G network slated to utilize these elevated frequency spectrums, ranging from 24 GHz to 100 GHz, this dissertation initially delves into RF coverage planning at a 70 GHz operating frequency using a conventional three-sector cell architecture, closely examining RF signal characteristics. The findings underscore issues of subpar SNR and signal strength encountered by the traditional cell architecture when employing array antennas with a greater number of antenna elements.

To address these challenges, this dissertation adopts a strategic approach. Firstly, this dissertation first employs nine and twelve sector cell architectures, where each sector is equipped with an advanced antenna system designed with subarray architecture, thereby providing adaptive beamforming and beam steering capabilities. The simulation outcomes reveal impressive RF coverage for the nine-sectored cell architecture. In this configuration, each sector is equipped with an 8-by-8 uniform phased array antenna situated at a height of 25 meters above ground level and tilted at a 30-degree angle. Conversely, the twelve-sectored cell architecture exhibits exceptional RF coverage performance. In this scenario, each sector is furnished with a 16-by-16 uniform phased array antenna, maintaining the same elevation above ground level, and employing a downtilt angle of 20 degrees.

In addition to the higher sectorization techniques, this dissertation introduces an adaptive cell-sectorization method that engages twelve sectors during peak traffic hours to maximize capacity, while conserving energy during off-peak periods through the use of fewer sectors (e.g., nine sectors or six sectors per cell). Simulation results unequivocally demonstrate that the proposed adaptive cell-sectorization method significantly reduces energy consumption during off-peak hours.

Furthermore, this dissertation delves into the numerous challenges associated with deploying 5G networks, including precise cell site planning, location acquisition, propagation modeling, energy efficiency, backhaul considerations, among others, and outlines future research directions aimed at surmounting these challenges.

## **7.2 Directions for Future Research**

Future research endeavors will encompass efforts aimed at building upon the existing work to achieve enhanced performance outcomes.

### ***7.2.1 Accurate Terrain Profile to Analyze RF coverage***

In this dissertation, terrain profiles obtained from Google Maps are utilized to visualize RF coverage and signal propagation. Consequently, the precision of RF coverage simulations, including SINR and signal strength, is contingent upon the up-to-date terrain profile of the deployment area. Consequently, mobile network operators should ensure the use of current terrain profiles when assessing RF coverage for outdoor deployment scenarios. Reliable sources for obtaining updated terrain profiles may include local government agencies and telecommunication vendors such as GIS Lounge.

### *7.2.2 Appropriate Propagation Modeling*

The primary objective of RF coverage planning is to evaluate the characteristics of RF signals, encompassing factors like signal attenuation and received signal levels, across the entire deployment area. Simulation outcomes and signal tracing techniques are utilized to estimate the maximum signal attenuation between transmitters and receivers. However, the accuracy of these measurements largely depends on the utilization of the correct propagation model, which should be suitable for the specific deployment area, whether indoor or outdoor. In this dissertation, the analysis of RF coverage, with a focus on SINR and signal strength, involves the use of free space propagation modeling, along with accounting for atmospheric constituents such as rain, gas, and fog. It's important to emphasize that the accuracy of simulations may vary in real-world deployment scenarios. Currently, there isn't a standardized empirical propagation model for the 5G network, underscoring the need for mobile network operators (MNOs) to conduct comprehensive testing across diverse deployment areas to formulate a suitable propagation model tailored to 5G networks.

### *7.2.3 RF Coverage Planning and Analysis for Indoor*

The 5G network necessitates separate cell sites for indoor and outdoor coverage due to high building penetration loss, as discussed in Section 7.2.8. However, this dissertation primarily focuses on outdoor deployment scenarios for planning and analyzing RF coverage. Future research could encompass RF coverage planning and signal analysis for indoor environments.



It's worth noting that the main RF signal impairment indoors typically arises from multipath signals, without the influence of weather-related impairments such as fog or rain. This dissertation offers an extensive multipath signal analysis that can readily serve as a foundation for indoor RF coverage planning. Consequently, extending the scope of this dissertation to include indoor RF coverage planning would be a natural progression.

#### *7.2.4 More Studies on Adaptive Cell-Sectorization*

The proposed adaptive cell-sectorization method employs an advanced antenna system designed with subarrays. However, each subarray necessitates additional equipment, such as T/R switches and connecting cables, for controlling the number of radiating elements and beam steering. This augmentation will lead to increased costs and power requirements. Consequently, a trade-off emerges where mobile network operators (MNOs) must carefully assess deployment scenarios with consideration for varying traffic conditions.

If traffic conditions fluctuate significantly between peak and off-peak hours, the proposed method stands to be a cost-effective means of conserving cell site power consumption. On the other hand, if traffic remains relatively stable, the cost-effectiveness of this approach may be less evident. Future research can involve conducting more case studies, involving real-world deployment areas and actual traffic demands, to comprehensively analyze the performance and applicability of the proposed method.

#### *7.2.5 Extensive Studies on Advanced Antenna System*

This dissertation introduces an Advanced Antenna System (AAS) consisting of subarrays, with the overall antenna performance being contingent on the architecture of

individual subarrays. In Chapter 2, a design for a uniform linear phased array architecture is presented, incorporating various antenna element configurations such as 16-by-16 and 32-by-32 arrays. The chapter highlights potential challenges, such as sidelobes and sidelobe power levels, and demonstrates the effectiveness of the Dolph-Chebyshev amplitude tapering method in reducing sidelobe power. However, it is noted that this approach can reduce directivity and widen the beamwidth.

Future research endeavors could explore alternative amplitude tapering methods, such as Taylor and Binomial tapering, and conduct a comparative analysis against the Dolph-Chebyshev method to determine the optimal solution. Additionally, further investigations might focus on different types of phased array architectures, such as planar arrays and frequency scanning arrays, aiming to compare their performances with the current work to identify the most suitable antenna configuration.

## REFERENCES

- [1] "Ericsson White Paper: This is 5G," Ericsson 2021. [Online]. Available: <https://www.ericsson.com/49f1c9/assets/local/5g/documents/07052021-ericsson-this-is-5g.pdf>
- [2] "Cisco 5G Vision Series: Laying the Foundation for New Technologies, Use Cases, and Business Models," Cisco, 2016.
- [3] M. M. A. S. Faruque, "5G Backhaul: Requirements, Challenges, and Emerging Technologies," in *Broadband Communications Networks - Recent Advances and Lessons from Practice*, A. H. A. Aqqal Ed.: intechopen, ch. 4, pp. 43-58.
- [4] E. Dahlman, G. Mildh, S. Parkvall, J. Peisa, J. Sachs, and Y. Selén, "5G radio access," *Ericsson review*, vol. 91, no. 6, pp. 42-48, 2014.
- [5] T. K. Sawanobori, "The Next Generation of Wireless: 5G Leadership in the U.S.," CTIA, February 9, 2016.
- [6] "Understanding 5G: Perspectives on future technological advancements in mobile," GSMA intelligence, White paper, December 2014. [Online]. Available: <https://www.gsmainelligence.com/research/?file=141208-5g.pdf&download>
- [7] M. M. Ahamed and S. Faruque, "5G Network Coverage Planning and Analysis of the Deployment Challenges," *Sensors*, vol. 21, no. 19, p. 6608, 2021. [Online]. Available: <https://www.mdpi.com/1424-8220/21/19/6608>.
- [8] "Recommendation ITU-R M.2150-0 (02/2021): Detailed specifications of the terrestrial radio interfaces of International Mobile Telecommunications-2020 (IMT-2020)."
- [9] "5G wireless access: an overview," Ericsson, White Paper, April 2020. [Online]. Available: <https://www.ericsson.com/en/reports-and-papers/white-papers/5g-wireless-access-an-overview>
- [10] "NGMN 5G white paper." NGMN. [https://www.ngmn.org/uploads/media/NGMN\\_5G\\_White\\_Paper\\_V1\\_0.pdf](https://www.ngmn.org/uploads/media/NGMN_5G_White_Paper_V1_0.pdf) (accessed 20 October 2015).
- [11] M. M. Ahamed, "Energy efficient Small Cell planning for high capacity wireless networks," M.S., The University of North Dakota, Grand Forks, 1600237, 2015. [Online]. Available: <https://www.proquest.com/dissertations-theses/energy-efficient-small-cell-planning-high/docview/1731939573/se-2?accountid=10906>

- [https://iastate.alma.exlibrisgroup.com/view/uresolver/01IASU\\_INST/openurl?url\\_ver=Z39.88-2004&rft\\_val\\_fmt=info:ofi/fmt:kev:mtx:dissertation&genre=dissertations+%26+theses&sid=ProQ:ProQuest+Dissertations+%26+Theses+Global&atitle=&title=Energy+efficient+Small+Cell+planning+for+high+capacity+wireless+networks&issn=&date=2015-01-01&volume=&issue=&spage=&au=Ahamed%2C+Md.+Maruf&isbn=978-1-339-08502-9&jtitle=&bttitle=&rft\\_id=info:eric/&rft\\_id=info:doi/](https://iastate.alma.exlibrisgroup.com/view/uresolver/01IASU_INST/openurl?url_ver=Z39.88-2004&rft_val_fmt=info:ofi/fmt:kev:mtx:dissertation&genre=dissertations+%26+theses&sid=ProQ:ProQuest+Dissertations+%26+Theses+Global&atitle=&title=Energy+efficient+Small+Cell+planning+for+high+capacity+wireless+networks&issn=&date=2015-01-01&volume=&issue=&spage=&au=Ahamed%2C+Md.+Maruf&isbn=978-1-339-08502-9&jtitle=&bttitle=&rft_id=info:eric/&rft_id=info:doi/)
- [12] M. R. Palattella *et al.*, "Internet of Things in the 5G Era: Enablers, Architecture, and Business Models," *IEEE Journal on Selected Areas in Communications*, vol. 34, no. 3, pp. 510-527, 2016, doi: 10.1109/JSAC.2016.2525418.
  - [13] G. A. Akpakwu, B. J. Silva, G. P. Hancke, and A. M. Abu-Mahfouz, "A Survey on 5G Networks for the Internet of Things: Communication Technologies and Challenges," *IEEE Access*, vol. 6, pp. 3619-3647, 2018, doi: 10.1109/ACCESS.2017.2779844.
  - [14] Y. Mehmood, N. Haider, M. Imran, A. Timm-Giel, and M. Guizani, "M2M Communications in 5G: State-of-the-Art Architecture, Recent Advances, and Research Challenges," *IEEE Communications Magazine*, vol. 55, no. 9, pp. 194-201, 2017, doi: 10.1109/MCOM.2017.1600559.
  - [15] R. Ratasuk, A. Prasad, Z. Li, A. Ghosh, and M. A. Uusitalo, "Recent advancements in M2M communications in 4G networks and evolution towards 5G," in *2015 18th International Conference on Intelligence in Next Generation Networks*, 17-19 Feb. 2015 2015, pp. 52-57, doi: 10.1109/ICIN.2015.7073806.
  - [16] K. E. Skouby and P. Lynggaard, "Smart home and smart city solutions enabled by 5G, IoT, AAI and CoT services," in *2014 International Conference on Contemporary Computing and Informatics (IC3I)*, 27-29 Nov. 2014 2014, pp. 874-878, doi: 10.1109/IC3I.2014.7019822.
  - [17] C. R. Storck and F. Duarte-Figueiredo, "A Survey of 5G Technology Evolution, Standards, and Infrastructure Associated With Vehicle-to-Everything Communications by Internet of Vehicles," *IEEE Access*, vol. 8, pp. 117593-117614, 2020, doi: 10.1109/ACCESS.2020.3004779.
  - [18] "Ericsson, Ericsson Mobility Report," November 2019. [Online]. Available: <https://www.ericsson.com/en/mobility-report>
  - [19] T. L. Singal, *Wireless Communications*. McGraw-Hill Education (India) Pvt Limited, 2010.
  - [20] A. C. F. Eriksson, M; Ronkainen, H; Willars, P; Östberg, C, "5G New Radio RAN and transport choices that minimize TCO," Ericsson Technology Review,

- November 7, 2019. [Online]. Available: <https://www.ericsson.com/en/reports-and-papers/ericsson-technology-review/articles/5g-nr-ran-and-transport-choices-thatminimize-tco>
- [21] J. C. Whitaker, *The Electronics Handbook*. Taylor & Francis, 1996.
  - [22] S. K. Islam and M. R. Haider, *Sensors and Low Power Signal Processing*. Springer US, 2009.
  - [23] M. M. Ahamed and S. Faruque, "Propagation factors affecting the performance of 5G millimeter wave radio channel," in *2016 IEEE International Conference on Electro Information Technology (EIT)*, 19-21 May 2016 2016, pp. 0728-0733, doi: 10.1109/EIT.2016.7535329.
  - [24] Y. S. Meng and Y. Lee, "Investigations of foliage effect on modern wireless communication systems: A review," *Progress in Electromagnetics Research-pier*, vol. 105, pp. 313-332, 2010.
  - [25] "Recommendation ITU-R P.840-6: Attenuation due to clouds and fog," Radiocommunication Sector of International Telecommunication Union, 2013.
  - [26] "Understanding 5G: Perspectives on future technological advancements in mobile," GSMA Intelligence, December 2014. [Online]. Available: <https://www.gsmainelligence.com/research/?file=141208-5g.pdf&download>
  - [27] V. H. M. Donald, "Advanced mobile phone service: The cellular concept," *The Bell System Technical Journal*, vol. 58, no. 1, pp. 15-41, 1979, doi: 10.1002/j.1538-7305.1979.tb02209.x.
  - [28] S. Faruque, *Cellular Mobile Systems Engineering* Artech House Mobile Communications, 1997.
  - [29] S. Faruque, *Radio frequency cell site engineering made easy*. Springer, 2019.
  - [30] R. I.-R. M.[IMT-2020.EVAL], "Guidelines for evaluation of radio interface technologies for IMT-2020," 2017. [Online]. Available: <https://www.itu.int/md/R15-SG05-C-0057>
  - [31] C. A. Balanis, *Antenna Theory: Analysis and Design*, 4 ed. Wiley, 2016.
  - [32] S. J. Orfanidis, *Electromagnetic Waves and Antennas*. Rutgers University, 2016.
  - [33] S. A. Busari, K. M. S. Huq, S. Mumtaz, L. Dai, and J. Rodriguez, "Millimeter-Wave Massive MIMO Communication for Future Wireless Systems: A Survey,"

- IEEE Communications Surveys & Tutorials*, vol. 20, no. 2, pp. 836-869, 2018, doi: 10.1109/COMST.2017.2787460.
- [34] V. Jungnickel *et al.*, "The role of small cells, coordinated multipoint, and massive MIMO in 5G," *IEEE Communications Magazine*, vol. 52, no. 5, pp. 44-51, 2014, doi: 10.1109/MCOM.2014.6815892.
  - [35] G. A. T. Warren L. Stutzman, *Antenna Theory and Design*, 3 ed. Wiley.
  - [36] R. L. Haupt, *Antenna Arrays: A Computational Approach*. Wiley-IEEE Press, 2010.
  - [37] R. L. H. J. McCormack, "Low sidelobe array by amplitude edge tapering the edge elements," Patent 5017928, 1991.
  - [38] J. G. Proakis and M. Salehi, *Digital Communications*, 5th ed. McGraw-Hill Education, 2007.
  - [39] H. T. Friis, "A Note on a Simple Transmission Formula," *Proceedings of the IRE*, vol. 34, no. 5, pp. 254-256, 1946, doi: 10.1109/JRPROC.1946.234568.
  - [40] "Recommendation ITU-R P.838-3: Specific attenuation model for rain for use in prediction methods," Radiocommunication Sector of International Telecommunication Union, 2005.
  - [41] "Recommendation ITU-R P.530-17: Propagation data and prediction methods required for the design of terrestrial line-of-sight systems," Radiocommunication Sector of International Telecommunication Union, 2017.
  - [42] "Millimeter Wave Propagation: Spectrum Management Implications," Federal Communications Commission, Bulletin Number 70, July, 1997.
  - [43] "Radiocommunication Sector of International Telecommunication Union," Recommendation ITU-R P.676-10: Attenuation by atmospheric gases 2013.
  - [44] "Radiocommunication Sector of International Telecommunication Union," Recommendation ITU-R P.676-13: Attenuation by atmospheric gases and related effects, 2022.
  - [45] "Testing RF Cables in Cellular Networks Combining LTE and 5G Technologies," 2022. [Online]. Available: <https://dl.cdn-anritsu.com/en-us/test-measurement/files/Application-Notes/Application-Note/11410-02878A.pdf>
  - [46] 2022, "RF Cable Measurements Help Ensure 5G Networks Meet KPIs." [Online]. Available: <https://anritsu.typepad.com/basestationtransmits/2022/08/rf-cable-measurements-help-ensure-5g-networks-meet-kpis.html>

- [47] N. P. L. H. H. D. Abbott, "Tri-Orthogonal Polarization Diversity for 5G Networks," *Transactions on Emerging Telecommunications Technologies*, vol. 27, no. 7, 03 May 2016 2016, doi: 10.1002/ett.3042.
- [48] Z. H. Lin and H. T. Chou, "Polarization-Tunable Phased Antenna Array Module at 28 GHz Band for 5G Applications," in *2021 International Symposium on Antennas and Propagation (ISAP)*, 19-22 Oct. 2021 2021, pp. 1-2, doi: 10.23919/ISAP47258.2021.9614517.
- [49] Bevelacqua; and P. J. Antenna Efficiency [Online] Available: <https://www.antenna-theory.com/basics/efficiency.php>
- [50] D. Rube-Hundhammer. Efficiency: A Crucial Attribute for Modern Antenna Systems [Online] Available: <https://www.ericsson.com/en/antenna-system/efficiency>
- [51] "Understanding mmWave Spectrum for 5G Networks," 5G Americas, 2020. [Online]. Available: <https://www.5gamericas.org/understanding-millimeter-wave-spectrum-for-5g-networks/>
- [52] I. A. Hemadeh, K. Satyanarayana, M. El-Hajjar, and L. Hanzo, "Millimeter-Wave Communications: Physical Channel Models, Design Considerations, Antenna Constructions, and Link-Budget," *IEEE Communications Surveys & Tutorials*, vol. 20, no. 2, pp. 870-913, 2018, doi: 10.1109/COMST.2017.2783541.
- [53] T. Wu, T. S. Rappaport, and C. M. Collins, "The human body and millimeter-wave wireless communication systems: Interactions and implications," in *2015 IEEE International Conference on Communications (ICC)*, 8-12 June 2015 2015, pp. 2423-2429, doi: 10.1109/ICC.2015.7248688.
- [54] "4G/5G Network Experience Evaluation " GSMA Intelligence, 2020. [Online]. Available: <https://www.gsma.com/futurenetworks/resources/4g-5g-network-experience-evaluation-guideline/>
- [55] V. Raghavan *et al.*, "Spatio-Temporal Impact of Hand and Body Blockage for Millimeter-Wave User Equipment Design at 28 GHz," *IEEE Communications Magazine*, vol. 56, no. 12, pp. 46-52, 2018, doi: 10.1109/MCOM.2018.1800213.
- [56] Jonathan *et al.*, "Modeling Human Blockers in Millimeter Wave Radio Links," 2012.
- [57] "Atlanta RF white paper: Link Budget Analysis: Getting Started," Atlanta RF Services, Software & Designs, 2013. [Online]. Available: [https://atlantarf.com/uploads/1/4/3/4/143448818/link\\_budget\\_-\\_getting\\_started.pdf](https://atlantarf.com/uploads/1/4/3/4/143448818/link_budget_-_getting_started.pdf)

- [58] C. Cox, *An Introduction to LTE: LTE, LTE-Advanced, SAE and 4G Mobile Communications*. Wiley Publishing, 2012.
- [59] F. Khan, *LTE for 4G Mobile Broadband: Air Interface Technologies and Performance*. Cambridge University Press, 2009.
- [60] M. Ayad, R. Alkanhel, K. Saoudi, M. Benziane, S. Medjedoub, and S. S. M. Ghoneim, "Evaluation of Radio Communication Links of 4G Systems," (in eng), *Sensors (Basel)*, vol. 22, no. 10, May 22 2022, doi: 10.3390/s22103923.
- [61] P. Kyosti, "WINNER II channel models," *IST, Tech. Rep. IST-4-027756 WINNER II DI.1.2 V1.2*, 2007 2007. [Online]. Available: <https://cir.nii.ac.jp/crid/1571698600936523008>.
- [62] "3GPP TR 25.996 - Spatial Channel Model for Multiple Input Multiple Output (MIMO) Simulations," Sep. 2012 2012.
- [63] S. Sun, T. S. Rappaport, M. Shafi, P. Tang, J. Zhang, and P. J. Smith, "Propagation Models and Performance Evaluation for 5G Millimeter-Wave Bands," *IEEE Transactions on Vehicular Technology*, vol. 67, no. 9, pp. 8422-8439, 2018, doi: 10.1109/TVT.2018.2848208.
- [64] M. Cudak, T. Kovarik, T. A. Thomas, A. Ghosh, Y. Kishiyama, and T. Nakamura, "Experimental mm wave 5G cellular system," in *2014 IEEE Globecom Workshops (GC Wkshps)*, 8-12 Dec. 2014 2014, pp. 377-381, doi: 10.1109/GLOCOMW.2014.7063460.
- [65] S. Hur, Y. Cho, J. Lee, K. Noh-Gyoung, J. Park, and H. Benn, "Synchronous channel sounder using horn antenna and indoor measurements on 28 GHz," in *2014 IEEE International Black Sea Conference on Communications and Networking (BlackSeaCom)*, 27-30 May 2014 2014, pp. 83-87, doi: 10.1109/BlackSeaCom.2014.6849010.
- [66] W. Roh *et al.*, "Millimeter-wave beamforming as an enabling technology for 5G cellular communications: theoretical feasibility and prototype results," *IEEE Communications Magazine*, vol. 52, no. 2, pp. 106-113, 2014, doi: 10.1109/MCOM.2014.6736750.
- [67] M. Kyro, V. Kolmonen, and P. Vainikainen, "Experimental Propagation Channel Characterization of mm-Wave Radio Links in Urban Scenarios," *IEEE Antennas and Wireless Propagation Letters*, vol. 11, pp. 865-868, 2012, doi: 10.1109/LAWP.2012.2210532.
- [68] T. S. Rappaport, F. Gutierrez, E. Ben-Dor, J. N. Murdock, Y. Qiao, and J. I. Tamir, "Broadband Millimeter-Wave Propagation Measurements and Models Using Adaptive-Beam Antennas for Outdoor Urban Cellular Communications," *IEEE*



*Transactions on Antennas and Propagation*, vol. 61, no. 4, pp. 1850-1859, 2013, doi: 10.1109/TAP.2012.2235056.

- [69] T. S. Rappaport, G. R. MacCartney, M. K. Samimi, and S. Sun, "Wideband Millimeter-Wave Propagation Measurements and Channel Models for Future Wireless Communication System Design," *IEEE Transactions on Communications*, vol. 63, no. 9, pp. 3029-3056, 2015, doi: 10.1109/TCOMM.2015.2434384.
- [70] G. R. MacCartney and T. S. Rappaport, "73 GHz millimeter wave propagation measurements for outdoor urban mobile and backhaul communications in New York City," in *2014 IEEE International Conference on Communications (ICC)*, 10-14 June 2014 2014, pp. 4862-4867, doi: 10.1109/ICC.2014.6884090.
- [71] 3GPP, "Study on channel model for frequencies from 0.5 to 100 GHz," 3rd Generation Partnership Project (3GPP), TR38.901 V14.3.0," Dec. 2017 2017.
- [72] "Study on 3D Channel Model for LTE (Rel. 12), 3GPP TR 36.873, V12.1.0," Mar. 2015 2015.
- [73] S. Sun *et al.*, "Investigation of Prediction Accuracy, Sensitivity, and Parameter Stability of Large-Scale Propagation Path Loss Models for 5G Wireless Communications," *IEEE Transactions on Vehicular Technology*, vol. 65, no. 5, pp. 2843-2860, 2016, doi: 10.1109/TVT.2016.2543139.
- [74] T. S. Rappaport, *Wireless Communications: Principles and Practice*, 2nd ed. Prentice Hall PTR, 1996.
- [75] Z. Lazarevic, "Ericsson white paper: Benchmark measurements in 5G networks," Aug 21, 2020 [Online]. Available: <https://www.ericsson.com/en/blog/2020/8/benchmark-measurements-in-5g-networks>
- [76] M. Sauter, *From GSM to LTE-Advanced Pro and 5G: An Introduction to Mobile Networks and Mobile Broadband*. John Wiley & Sons, 2017.
- [77] J. Hoy, *Forensic Radio Survey Techniques for Cell Site Analysis*. John Wiley & Sons, 2015.
- [78] Y. Boyadzhieva, "Operators can save billions with better RAN planning – white paper," TelecomTV, Jul 7, 2022 2022. [Online]. Available: <https://www.telecomtv.com/content/access-evolution/operators-can-save-billions-with-better-ran-planning-white-paper-44902/>
- [79] "Accurate RAN planning saves billions," Infovista, Infovista.com, July 2022 2022. [Online]. Available: <https://www.infovista.com/resources/re/accurate-ran-planning-saves-billions>

- [80] "Planet (developed by Infovista)." <https://www.infovista.com/5g-network> (accessed Nov 12, 2023).
- [81] "Atoll (developed by Forsk)." <https://www.forsk.com/4g5g> (accessed Nov 12, 2023).
- [82] "ASSET Radio (developed by TEOCO) " <https://www.teoco.com/products-services/ran-solutions/planning/radio-planning/> (accessed Nov 12, 2023).
- [83] "OpenStreetMap." <https://www.openstreetmap.org/> (accessed).
- [84] S. Kumar, I. Z. Kovacs, G. Monghal, K. I. Pedersen, and P. E. Mogensen, "Performance Evaluation of 6-Sector-Site Deployment for Downlink UTRAN Long Term Evolution," in *2008 IEEE 68th Vehicular Technology Conference*, 21-24 Sept. 2008 2008, pp. 1-5, doi: 10.1109/VETECF.2008.384.
- [85] M. U. Sheikh and J. Lempiäinen, "A Flower Tessellation for Simulation Purpose of Cellular Network with 12-Sector Sites," *IEEE Wireless Communications Letters*, vol. 2, no. 3, pp. 279-282, 2013, doi: 10.1109/WCL.2013.022213.120861.
- [86] J. García-Morales, G. Femenias, and F. Riera-Palou, "Higher Order Sectorization in FFR-Aided OFDMA Cellular Networks: Spectral- and Energy-Efficiency," *IEEE Access*, vol. 7, pp. 11127-11139, 2019, doi: 10.1109/ACCESS.2019.2892187.
- [87] R. Joyce, D. Morris, S. Brown, D. Vyas, and L. Zhang, "Higher Order Horizontal Sectorization Gains for 6, 9, 12 and 15 Sectorized Cell Sites in a 3GPP/HSPA+ Network," *IEEE Trans. Veh. Technol.*, vol. 65, no. 5, pp. 3440-3449, / 2016, doi: 10.1109/TVT.2015.2446945.
- [88] H. Huang *et al.*, "Increasing throughput in cellular networks with higher-order sectorization," in *2010 Conference Record of the Forty Fourth Asilomar Conference on Signals, Systems and Computers*, 7-10 Nov. 2010 2010, pp. 630-635, doi: 10.1109/ACSSC.2010.5757638.
- [89] M. U. Sheikh and J. Lempiäinen, "Migration to 28 GHz frequency with higher order sectorization in urban macro cellular environment," in *2016 23rd International Conference on Telecommunications (ICT)*, 16-18 May 2016 2016, pp. 1-5, doi: 10.1109/ICT.2016.7500460.
- [90] N. Al-Falahy and O. Y. K. Alani, "The Impact of Higher Order Sectorisation on the Performance of Millimetre Wave 5G Network," in *2016 10th International Conference on Next Generation Mobile Applications, Security and Technologies (NGMAST)*, 24-26 Aug. 2016 2016, pp. 1-5, doi: 10.1109/NGMAST.2016.20.
- [91] A. Arbi and T. O. Farrell, "Energy efficiency in 5G access networks: Small cell densification and high order sectorisation," in *2015 IEEE International Conference*

- on Communication Workshop (ICCW), 8-12 June 2015 2015, pp. 2806-2811, doi: 10.1109/ICCW.2015.7247604.
- [92] G. Auer *et al.*, "How much energy is needed to run a wireless network?," *IEEE Wireless Communications*, vol. 18, no. 5, pp. 40-49, 2011, doi: 10.1109/MWC.2011.6056691.
  - [93] C. A. Balanis, *Antenna Theory: Analysis and Design*, 2 ed. Wiley, 1996.
  - [94] "Huawei 5G Wireless Network Planning Solution White Paper," 2018. [Online]. Available: [https://www-file.huawei.com/-/media/corporate/pdf/white%20paper/2018/5g\\_wireless\\_network\\_planning\\_solution\\_en\\_v2.pdf?la=en-us](https://www-file.huawei.com/-/media/corporate/pdf/white%20paper/2018/5g_wireless_network_planning_solution_en_v2.pdf?la=en-us)
  - [95] "Infrastructure Sharing." GSMA Intelligence. <https://www.gsma.com/futurenetworks/wiki/infrastructure-sharing-an-overview/> (accessed 12-29-20).
  - [96] S. Ondrusova and C. Hutchison, "5G Implementation Guidelines," July 2019. [Online]. Available: <https://www.gsma.com/futurenetworks/wp-content/uploads/2019/03/5G-Implementation-Guideline-v2.0-July-2019.pdf>
  - [97] "Tower and Antenna Siting." Federal Communications Commission. <https://www.fcc.gov/wireless/bureau-divisions/competition-infrastructure-policy-division/tower-and-antenna-siting> (accessed 12-30-20).
  - [98] A. I. Sulyman, A. T. Nassar, M. K. Samimi, G. R. Maccartney, T. S. Rappaport, and A. Alsanie, "Radio propagation path loss models for 5G cellular networks in the 28 GHZ and 38 GHZ millimeter-wave bands," *IEEE Communications Magazine*, vol. 52, no. 9, pp. 78-86, 2014, doi: 10.1109/MCOM.2014.6894456.
  - [99] M. K. Samimi and T. S. Rappaport, "3-D Millimeter-Wave Statistical Channel Model for 5G Wireless System Design," *IEEE Transactions on Microwave Theory and Techniques*, vol. 64, no. 7, pp. 2207-2225, 2016, doi: 10.1109/TMTT.2016.2574851.
  - [100] E. G. Larsson, O. Edfors, F. Tufvesson, and T. L. Marzetta, "Massive MIMO for next generation wireless systems," *IEEE Communications Magazine*, vol. 52, no. 2, pp. 186-195, 2014, doi: 10.1109/MCOM.2014.6736761.
  - [101] A. L. Swindlehurst, E. Ayanoglu, P. Heydari, and F. Capolino, "Millimeter-wave massive MIMO: the next wireless revolution?," *IEEE Communications Magazine*, vol. 52, no. 9, pp. 56-62, 2014, doi: 10.1109/MCOM.2014.6894453.
  - [102] E. Zola, A. J. Kassler, and W. Kim, "Joint User Association and Energy Aware Routing for Green Small Cell mmWave Backhaul Networks," in *2017 IEEE*

*Wireless Communications and Networking Conference (WCNC)*, 19-22 March 2017 2017, pp. 1-6, doi: 10.1109/WCNC.2017.7925706.

- [103] A. R. Ekti, M. Z. Shakir, E. Serpedin, and K. A. Qaraqe, "End-to-end downlink power consumption of heterogeneous small-cell networks based on the probabilistic traffic model," in *2014 IEEE Wireless Communications and Networking Conference (WCNC)*, 6-9 April 2014 2014, pp. 1138-1142, doi: 10.1109/WCNC.2014.6952289.
- [104] I. Humar, X. Ge, L. Xiang, M. Jo, M. Chen, and J. Zhang, "Rethinking energy efficiency models of cellular networks with embodied energy," *IEEE Network*, vol. 25, no. 2, pp. 40-49, 2011, doi: 10.1109/MNET.2011.5730527.
- [105] E. Oh, B. Krishnamachari, X. Liu, and Z. Niu, "Toward dynamic energy-efficient operation of cellular network infrastructure," *IEEE Communications Magazine*, vol. 49, no. 6, pp. 56-61, 2011, doi: 10.1109/MCOM.2011.5783985.
- [106] K. Wang, X. Hu, H. Li, P. Li, D. Zeng, and S. Guo, "A Survey on Energy Internet Communications for Sustainability," *IEEE Transactions on Sustainable Computing*, vol. 2, no. 3, pp. 231-254, 2017, doi: 10.1109/TSUSC.2017.2707122.
- [107] N. Bhushan *et al.*, "Network densification: the dominant theme for wireless evolution into 5G," *IEEE Communications Magazine*, vol. 52, no. 2, pp. 82-89, 2014, doi: 10.1109/MCOM.2014.6736747.
- [108] U. Siddique, H. Tabassum, E. Hossain, and D. I. Kim, "Wireless backhauling of 5G small cells: challenges and solution approaches," *IEEE Wireless Communications*, vol. 22, no. 5, pp. 22-31, 2015, doi: 10.1109/MWC.2015.7306534.
- [109] M. Jaber, M. A. Imran, R. Tafazolli, and A. Tukmanov, "5G Backhaul Challenges and Emerging Research Directions: A Survey," *IEEE Access*, vol. 4, pp. 1743-1766, 2016, doi: 10.1109/ACCESS.2016.2556011.
- [110] M. M. Ahamed and S. Faruque, "Design a 5G Backhaul Network Based on Free Space Optics and Analyze the Link Performances," presented at the 2017 IEEE 36th International Performance Computing and Communications Conference (IPCCC), December 10-12, 2017.
- [111] M. M. Ahamed, S. Faruque, and S. K. Gaire, "Laser radio: backhaul solution for 5G networks," 2016, vol. 9979, pp. 99790C-99790C-10. [Online]. Available: <http://dx.doi.org/10.1117/12.2237952>. [Online]. Available: <http://dx.doi.org/10.1117/12.2237952>
- [112] C. Dehos, J. L. González, A. D. Domenico, D. Kténas, and L. Dussot, "Millimeter-wave access and backhauling: the solution to the exponential data traffic increase

- in 5G mobile communications systems?," *IEEE Communications Magazine*, vol. 52, no. 9, pp. 88-95, 2014, doi: 10.1109/MCOM.2014.6894457.
- [113] Z. Gao, L. Dai, D. Mi, Z. Wang, M. A. Imran, and M. Z. Shakir, "MmWave massive-MIMO-based wireless backhaul for the 5G ultra-dense network," *IEEE Wireless Communications*, vol. 22, no. 5, pp. 13-21, 2015, doi: 10.1109/MWC.2015.7306533.
- [114] H. Zhao *et al.*, "28 GHz millimeter wave cellular communication measurements for reflection and penetration loss in and around buildings in New York city," in *2013 IEEE International Conference on Communications (ICC)*, 9-13 June 2013 2013, pp. 5163-5167, doi: 10.1109/ICC.2013.6655403.
- [115] C. A. L. Diakhate, J. Conrat, J. Cousin, and A. Sibille, "Millimeter-wave outdoor-to-indoor channel measurements at 3, 10, 17 and 60 GHz," in *2017 11th European Conference on Antennas and Propagation (EUCAP)*, 19-24 March 2017 2017, pp. 1798-1802, doi: 10.23919/EuCAP.2017.7928696.